Molecular Dynamics Simulations of Cluster-assembled Metallic Glasses

TECHNISCHE
UNIVERSITÄT
DARMSTADT

Materials and Earth
Sciences Department

Joint Laboratory
Nanomaterials
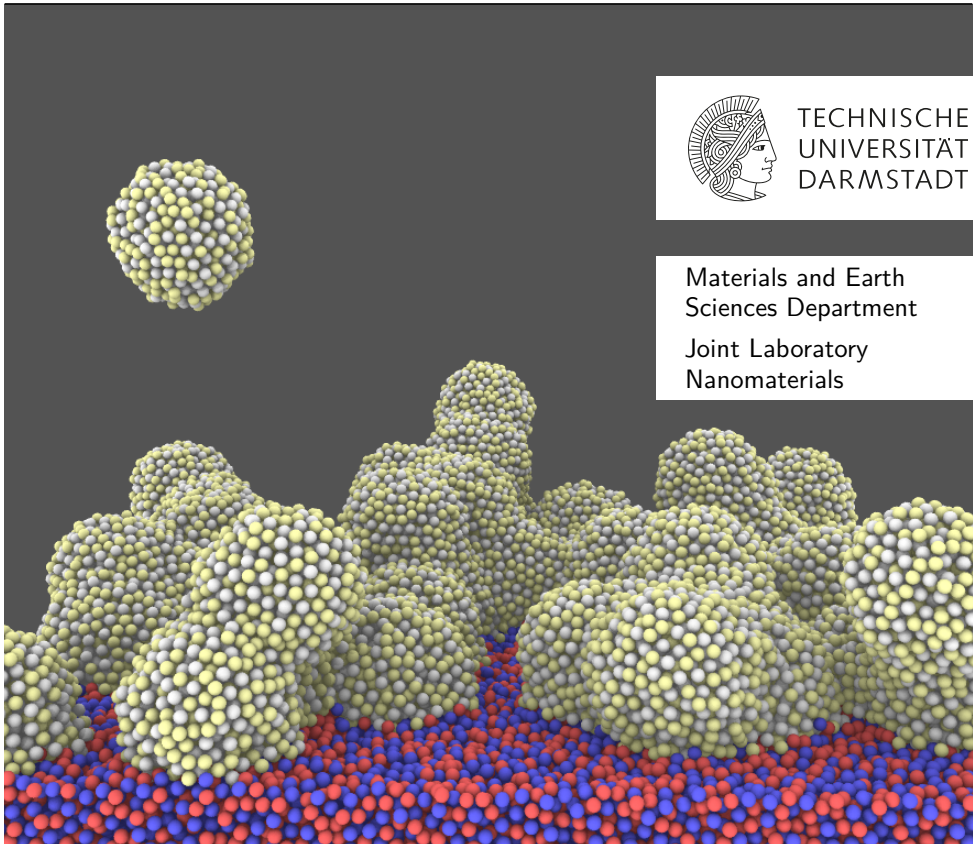
Molecular Dynamics Simulations of Cluster-assembled Metallic Glasses
Molekulardynamik-Simulationen von Cluster-assemblierten Metallischen Gläsern

Accepted doctoral thesis by MSc. Syamal Praneeth Chilakalapudi

1. Review: Prof. Dr.-Ing. Horst Hahn
2. Review: Prof. Dr. rer. nat. Karsten Albe
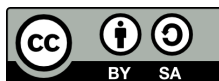
Date of submission: 30 Nov. 2022
Date of thesis defense: 17 Apr. 2023

Darmstadt, Technical University of Darmstadt

నా తల్లిదండ్రులకు మరియు శ్రేయోభిలాషులకు అంకితం
Dedicated to my parents and well-wishers—my pillars of strength

Abstract/Zusammenfassung

Abstract

Metallic glasses are an exciting class of amorphous materials, primarily known for their interesting properties such as high resilience and superior strength. Tailoring the local structure of these glasses is a step towards an increased control of their properties in a manner similar to how microstructures of crystalline materials are already being altered to suit various applications today. Recently, films prepared via an intricate assembly of amorphous clusters by energetic deposition were reported to demonstrate a remarkable change in properties depending on the deposition energy. The properties of the so-prepared cluster-assembled metallic glasses are currently believed to arise from the deposition process, and the formation of cluster-cluster interfaces—creating novel microstructures otherwise absent in traditionally prepared glasses. Being in the nascent stages of conception, the nature of the cluster-assembled glasses remains largely unexplored.

In the present thesis, molecular dynamics simulations of the cluster-assembled metallic glasses are studied in a model CuZr system. The development and implementation of new simulation protocols uncover the mechanisms of the formation routes to these novel cluster-assembled glassy films, the morphologies adopted by the clusters, and the local topological order in the materials. Two amorphous phases are identified in these glasses: one in the cores of the clusters, and the other in the continuous network of interfaces formed amongst the clusters. The amorphous short- and medium-range orders of cluster-assembled glasses are demonstrated to not only differ considerably from the traditional metallic glasses prepared by rapid quenching, but also to vary with cluster-impact energies in both the core and interface regions. In cluster-assembled glasses the interface regions are more densely packed than the cores, while the core atoms occupy lower energy states—a surprising outcome when contrasted with the traditional glasses where denser packing and lower energetic states occur together. Such an interesting occurrence is found to be a consequence of the core and interface regions having distinct chemical compositions. The inherent chemical heterogeneity of the precursor clusters also plays a role in the variation of local order and energetic states of cluster-assembled

glasses made from varying cluster sizes. However, the local short-range order and the thermal evolution of the enthalpy is found to be invariant with cluster size in these materials. These investigations provide a computer-aided understanding of amorphous cluster assembly and the synthesis of tailorable non-crystalline architectures in the quest to harness the properties of amorphous materials in the future.

Zusammenfassung

Metallische Gläser sind eine spannende Klasse amorpher Materialien, die vor allem für ihre interessanten Eigenschaften wie hohe Widerstandsfähigkeit und überlegene Festigkeit bekannt sind. Die maßgeschneiderte lokale Struktur dieser Gläser ist ein Schritt hin zu einer besseren Kontrolle ihrer Eigenschaften, ähnlich wie Mikrostrukturen kristalliner Materialien bereits geändert werden, um sie an verschiedene Anwendungen anzupassen. Kürzlich wurde berichtet, dass Filme, die durch eine komplizierte Anordnung von amorphen Clustern durch deren energetische Abscheidung hergestellt wurden, eine bemerkenswerte Veränderung der Eigenschaften allein durch die Abscheidungsenergie aufweisen. Es wird derzeit angenommen, dass die Eigenschaften der so hergestellten cluster-assemblierten metallischen Gläser aus den Besonderheiten der Abscheidetechnik und durch die Bildung von Cluster-Cluster-Grenzflächen, die neuartige Mikrostrukturen erzeugen, die es in herkömmlich hergestellten Gläsern nicht existieren. Da das Konzept noch in den Kinderschuhen steckt, ist die Natur der cluster-assemblierten Gläser noch weitgehend unerforscht.

In der vorliegenden Arbeit werden Molekulardynamiksimulationen der cluster-assemblierten metallischen Gläser im CuZr-Modellsystem untersucht. Die Entwicklung und Implementierung neuer Simulationsprotokolle umfasst die Mechanismen der Bildungswege dieser neuartigen cluster-assemblierten amorphen Filme, die Morphologien, der Cluster, und die lokale topologische Ordnung in den Materialien. In diesen Gläsern werden zwei amorphe Phasen identifiziert: eine in den Kernen der Cluster und die andere in dem kontinuierlichen Netzwerk von Grenzflächen, das sich zwischen den Clustern bildet. Die kurz- und mittelreichweitige Ordnung der cluster-assemblierten Gläser unterscheiden sich nicht nur erheblich von den traditionellen metallischen Gläsern, die durch schnelles Abschrecken hergestellt werden, sondern variieren auch mit den Abscheideenergien der Cluster sowohl im Kern als auch in den Grenzflächenbereichen. In cluster-assemblierten Gläsern sind die Grenzflächenregionen dichter gepackt als die Kerne, während die Kernatome niedrigere Energiezustände einnehmen - ein überraschendes Ergebnis, wenn man es mit den traditionellen Gläsern vergleicht, bei denen dichtere Packung und niedrigere Energiezustände zusammen auftreten. Dieses interessante Phänomen ist darauf zurückzuführen, dass die Kern- und Grenzflächenregionen unterschiedliche chemische

Zusammensetzungen aufweisen. Die inhärente chemische Heterogenität der Cluster im Ursprungszustand spielt ebenfalls eine Rolle bei der Variation der lokalen Ordnung und den energetischen Zuständen von cluster-assemblierten Gläsern, die aus unterschiedlich großen Clustern bestehen. Die lokale Nahbereichsordnung und die thermische Entwicklung der Enthalpie sind in diesen Materialien jedoch nicht von der Clustergröße abhängig. Diese Untersuchungen ermöglichen ein computergestütztes Verständnis von amorphen Cluster und die Synthese maßgeschneiderter nichtkristalliner Architekturen, um die Eigenschaften amorpher Materialien in Zukunft nutzbar zu machen.

Table of Contents

Contents

List of Figures

List of Tables

Glossary

E_{coh} cohesive energy.

G Gibbs free energy.

R_C^{max} radius of curvature.

T_C Curie temperature.

T_k Kauzmann temperature.

T_x crystallisation temperature.

Z coordination number.

η von-Mises strain.

fs femtosecond.

μm micrometres (10^{-6} metres).

$ar.u.$ area units.

2D two-dimensional.

3D three-dimensional.

ABC autonomous basin climbing.

APT atom-probe tomography.

BM ball-milling.

BMG bulk metallic glasses.

CAMG cluster-assembled metallic glass.

CAMs cluster-assembled materials.

CIBD cluster-ion beam deposition.

DFT density functional theory.

EAM embedded atom model.

ECP efficient cluster packing.

EDX energy-dispersive x-ray spectroscopy.

EXAFS extended x-ray absorption fine structure.

FCC face-centered cubic.

FI full-icosahedral.

ForHLR II forschungshochleistungsrechner.

GFA glass-forming ability.

GUM geometrically-unfavoured motifs.

HCP hexagonal close-packed.

HoreKa hochleistungsrechner Karlsruhe.

HPC high-performance computing.

ICO-like icosahedral-like.

IGC inert-gas condensation.

IHP inverse Hall-Petch.

ILO icosahedral-like order.

INT Institute of Nanotechnology.

KIT Karlsruhe Institute of Technology.

LAMMPS large-scale atomic/molecular massively parallel simulator.

LJ Lennard-Jones.

LRO long-range order.

MC Monte Carlo.

MD molecular dynamics.

MG metallic glass.

MG_ht heat-treated Metallic Glass.

MPI message passing interface.

MRO medium-range order.

MS Mössbauer spectroscopy.

NCM nanocrystalline materials.

NG nanoglass.

ns nanosecond.

OVITO open visualisation tool.

PAS positron annihilation spectroscopy.

PBC periodic boundary conditions.

PE potential energy.

PEL potential-energy landscape.

PRDF partial radial distribution function.

PVD physical-vapour deposition.

QNA quasi-nearest atom.

QS quadrupole splitting.

RDF radial distribution function.

RMC reverse Monte Carlo.

RMSD$_{shell}$ root mean square deviation of the shell atoms.

RQ rapidly-quenched.

SC simple cubic.

SRO short-range order.

STZ shear transformation zones.

T$_g$ glass-transition temperature.

T$_m$ melting temperature.

TEM transmission electron microscopy.

UHV ultra-high vacuum.

VP Voronoi polyhedra.

XANES x-ray absorption near edge structure.

XRD x-ray diffraction.

1. Introduction

1.1. Motivation

Metallic glasses (MGs), which are a class of amorphous metal-metal or metal-metalloid alloys, have been well studied for decades. Initially synthesized in the group of Pol Duwez [1], MGs of various compositions and systems have since been investigated, revealing many structural and functional properties [2–5]. These bulk-processed MGs, have a homogeneous distribution of the constituent elements (depicted in Figure 1.1a), and are possess many interesting characteristics such as low density, high stiffness, high wear and corrosion resistance, better thermoplasticity, and biocompatibility in comparison to crystalline materials—finding various applications in aerospace materials, machine components, casting and thermoplastic forming, wear-resistant surgical tools, and medical implants [6, 7].

Conventionally, MGs are prepared from a melt as rapidly-quenched (RQ) solids, or by ball-milling (BM) mixtures of elements [1, 2, 8, 9]. In the late 1980s, a new class of MGs came to prominence. The advent of nanocrystalline materials (NCM) production via compaction of nanopowders, motivated the synthesis of a novel kind of metallic glass called nanoglass (NG)—by the mechanical compaction of amorphous nanoparticles [10, 11]. This bottom-up approach to amorphisation, shown in Figure 1.1b, and successive research on NGs [11–17] indicated that NGs are present with additional structural features—deduced to arise from nanoparticle interface formation—that are not achievable in MGs prepared by RQ and BM. The NG structural model is reminiscent of that of NCMs i.e., cores embedded in an interfacial network; however, both the cores and interfaces in the NGs are fully amorphous [12, 18–21].

While the tailoring of structural and functional properties (by varying composition and quenching rate) of conventional metallic glasses is quite challenging, the new processing route of making NGs offers many advantages. The current research indicates that the interface formation and the surface segregation in nanoparticles lead to interesting features and properties of NGs such as reduced density and enhanced plasticity [18, 20, 22–27].
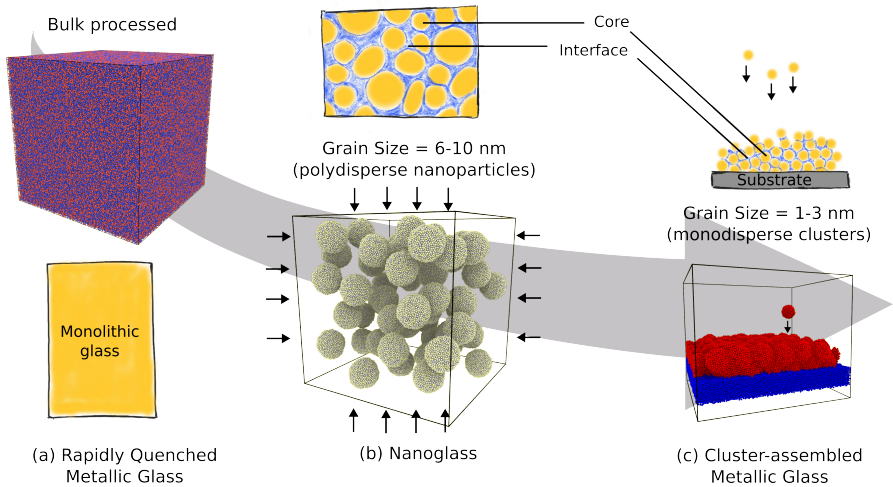
Figure 1.1.: Building metallic glasses from bottom-up: (a) Traditional metallic glasses have a homogenous amorphous structure. Glasses built from amorphous nanoclusters by (b) compaction form nanoglasses, and by (c) energetic deposition create cluster-assembled glasses. The hand-drawn illustrations indicate the broad microstructural differences expected between the bulk processed glasses and those prepared from bottom-up approaches.

More recently, it has been discovered that MGs can also be produced from atomic clusters which are substantially smaller than the building blocks of NGs. Cluster-assembled amorphous films were demonstrated to be synthesised by the energetic deposition of small clusters (Illustrated in Figure 1.1) in the size range of 10-2000 atoms per cluster, onto a substrate under ultra-high vacuum (UHV) [28–30]. Such materials have been referred to as cluster-assembled metallic glasses (CAMGs).

A first report on CAMGs detailed their preparation from 10-16 atoms-sized Cu-Zr clusters of varying compositions, characterising the resulting films as amorphous by synchrotron-based diffraction [28, 29]. However, a detailed account of the structure was not given. In another study, $Fe_{80}Sc_{20}$ CAMGs were prepared from 800 atom-sized clusters [30, 31]. By changing only the deposition energy of the cluster assembly, the average local structure—characterised by synchrotron extended x-ray absorption fine structure (EXAFS)—and the ferromagnetic transition temperatures (T_C) were found to change significantly in

the CAMG of constant macroscopic composition of $Fe_{80}Sc_{20}$. This possibility to modify the amorphous structure by the novel CAMG preparation methods presents a novel opportunity to control properties of amorphous solids.

Due to the difference in the preparation methods, and the intriguing observations mentioned above, the structural features of CAMGs are expected to be different from those of NGs and CAMGs, which are in turn known to differ from each other [18, 20, 23, 24]. The structural characterisation of CAMGs is currently limited to the EXAFS study of the $Fe_{80}Sc_{20}$ CAMGs [30], further exploration of CAMGs with advanced transmission electron microscopy (TEM) and atom-probe tomography (APT) methods is pending. At this juncture, complementary computational studies can prove to be a powerful tool to improve existing knowledge on CAMGs. Virtual insights from computer simulations can not only describe the dynamics and the structure at the atomic level, but also perform parametric studies with ease—thereby guiding future experiments on CAMGs.

1.2. Objective, Scope and Outline of this thesis

1.2.1. Objective

The objective of the present work is to describe the mechanisms of formation routes and the structures attained by the CAMGs, by developing specific molecular dynamics (MD) simulations for the same system. A special emphasis is given to how cluster deposition as a processing method affects both the structure and packing of the CAMGs in comparison to rapid quenching in MGs and mechanical compaction in NGs. With the intention to connect to various previous studies on MGs and NGs, and also due to availability of a well-known molecular dynamics potential, Cu-Zr has been chosen as a model system to investigate CAMGs.

1.2.2. Scope

$Cu_{50}Zr_{50}$ clusters were simulated using MD techniques to replicate a cluster-structure as obtained by inert-gas condensation (IGC) in the experiments. A distinction is made between clusters—which are in the size scales of 1-3 nm—and nanoparticles, which have a diameter greater than 4 nm.

The deposition of single $Cu_{50}Zr_{50}$ clusters (the protocol for which was developed within the framework of the thesis) was studied with varying impact energies to gain a semi-quantitative understanding on morphologies and distortion of the deposited clusters.

Two efficient simulation algorithms of deposition of a monodisperse clusters were developed to virtually synthesise CAMG films at various deposition energies. The latter of the two algorithms was designed to deposit clusters in a densely packed manner to reduce porosity and maximise cluster-cluster interactions for optimal interface creation. A monodisperse model of NGs is designed to compare the effects of cluster-processing routes of deposition (in CAMGs) with that of compaction (in the NGs). Although the cluster/nanoparticle size-distribution in the NG-experiments is polydisperse, the NGs in this are limited to mono-disperse cluster distributions. Simulations of Cu-Zr RQ MGs were developed and studied to serve as a reference standard to compare CAMGs and NGs with. In this thesis, the terms glass and MG shall be used interchangeably unless mentioned otherwise.

The CAMGs of 3 nm sized $Cu_{50}Zr_{50}$ clusters were made at varying impact energies. The surface atoms of the yet-to-be deposited clusters were found to form a network of cluster-cluster interfaces. The simulated 3 nm cluster CAMGs were evaluated and compared with NGs and RQ MGs by means of short-range order (SRO), medium-range order (MRO), and atomic packing and energetic characteristics. Furthermore, the influence of the cluster size on the cluster-cluster interfaces in CAMGs and NGs was investigated.

1.2.3. Outline

Chapter 2 introduces the theoretical background required for the thesis, providing a historical narrative of the research on metallic glasses and nanoglasses, which had motivated the study of cluster-assembled glasses. The definitions pertinent to glassy systems, and the concepts relevant to the computational study of Cu-Zr binary metallic glasses, as well as a review of the relevant literature is included.

Chapter 3 elaborates the molecular dynamics technique used to perform the necessary simulations, and presents information about the various characterisation methods used to evaluate the simulated data sets.

Chapter 4 presents the development of two efficient protocols to simulate the CAMGs. Simulations of RQ MGs are discussed to establish a standard of reference. The model chosen to simulate NGs is also mentioned.

In Chapter 5 the structure of CAMGs is investigated in depth as a function of deposition energy, and compared with RQ MGs and NGs. The formation of interfaces, and their evolution with impact energies in CAMGs is noted. The structural characterisation and atomic-property inspection of CAMGs unravel the relationships of their SRO and MRO with the impact energy.

The scaling of interface formation with the cluster size in CAMGs and NGs is explored in Chapter 6. The rise of cluster-size effects, and its influence on their structure and characteristics in the CAMGs are presented.

The results and findings of the presented research are concluded in Chapter 7 and promising directions for future research are proposed.

2. Scientific Background

This chapter discusses the relevant historical overview and scientific knowledge that forms the basis of this thesis. First and foremost, the traditional metallic glass (MG), which is made by rapid quenching is discussed. The fundamentals of MGs synthesis, their properties and the computation-aided structural models are provided. Next, the nanoglass (NG)—which is a recent class of MGs–is introduced. The details on how to prepare the NGs, and their relevant structural models are elaborated. Equipped with the fundamentals of MGs and NGs, the reader is then acquainted with the concept of the novel cluster-assembled metallic glass (CAMG). The details of the initial CAMG experiments, and the current advances and limits of the understanding of CAMG is covered.

2.1. Metallic Glasses

In their natural state, metallic solids exhibit crystalline order. However, when an alloy is cooled from a liquid to solid state fast enough i.e., supercooled, typically at high cooling rates of $10^5 - 10^6$ K/s, it gives rise to a metallic solid with an amorphous structure [32]. This is because the atomic mobility of the liquid decreases drastically before any crystallisation nucleation events can occur during the cooling, and the so-obtained solid is trapped in a state with no long-range order (LRO). These materials, exhibiting a lack of LRO, are broadly termed as glasses. They are already known to occur in nature (as obsidian and amber), and have also been artificially produced from silicates, polymers and even dextrose [5, 33]. Primarily, MGs are supercooled metallic materials exhibiting amorphous atomic arrangement. In 1960, Duwez et al. [1, 9] devised an apparatus to rapidly quench molten materials. Their successful synthesis of an entirely amorphous $Au_{75}Si_{25}$ flake led the foray into MG research [1]. The interesting physics in the MGs will be discussed in the following sections.

2.1.1. Glass Transition and Free Volume

The liquid to solid transition of glasses, known as glass transition, is very different from that exhibited in crystalline materials—as shown in Figure 2.1a. For the crystalline material, the liquid upon solidification undergoes a sharp phase transition in the specific volume or enthalpy at the melting temperature (T_m). The glass transition is much more gradual, occurring at the glass-transition temperature (T_g). A slower cooled glass (glass 2 in Figure 2.1a) demonstrates a lower glass transition temperature ($T_{g2} < T_{g1}$).

In general, physical changes in materials can be classified based on the change in the phases, typically described by an order parameter. By the Ehrenfest classification, the order of the lowest derivative of the Gibbs free energy (defined as G = H - TS, where H, T, and S are enthalpy, temperature, and entropy respectively) exhibiting a discontinuity upon crossing the phase boundary is the order of a phase transition [34]. By this definition, $G(T,p)$ is continuous in a first order phase transition but its first derivatives are discontinuous:

$$-\left(\frac{\partial G}{\partial T}\right)_p = S, \text{ and } \left(\frac{\partial G}{\partial p}\right)_T = V \tag{2.1}$$

where S, p, V and H are the entropy, pressure, volume, and enthalpy of the system, respectively. In the second order phase transition, the first derivatives are continuous but the second-order derivatives of $G(T,p)$, and also the following response functions are discontinuous:

$$C_p = T\left(\frac{\partial S}{\partial T}\right)_p = -T\left(\frac{\partial^2 G}{\partial T^2}\right)_p, \ \alpha = \frac{1}{V}\left(\frac{\partial V}{\partial T}\right)_p = \frac{1}{V}\left(\frac{\partial^2 G}{\partial T \partial p}\right),$$
$$\text{and } \kappa_T = -\frac{1}{V}\left(\frac{\partial V}{\partial p}\right)_T = -\frac{1}{V}\left(\frac{\partial^2 G}{\partial p^2}\right)_T, \tag{2.2}$$

where C_p, α, and κ_T are the isobaric heat capacity, coefficient of thermal expansion, and isothermal compressibility, respectively. The first- and second-order phase transitions are illustrated in Figure 2.1b. The first order transition is discontinuous in entropy (S) and volume (V) (See Figure 2.1bi-bii). The second order transition, while continuous in S, is discontinuous in heat capacity (C_p) (See Figure 2.1biii-biv). It can now be clearly noticed that the transition from the liquid to the crystalline material depicted in Figure 2.1a is a first-order phase transition. The glasses, on the other hand, exhibit the glass transition, which is continuous in the volume or enthalpy order parameters, but discontinuous in viscosity and specific heat. The glass transition is a second order phase-transition [5, 35] and has been experimentally demonstrated in many materials [36].

Contrary to the liquid-to-crystalline solid transition, the glass transition is not an
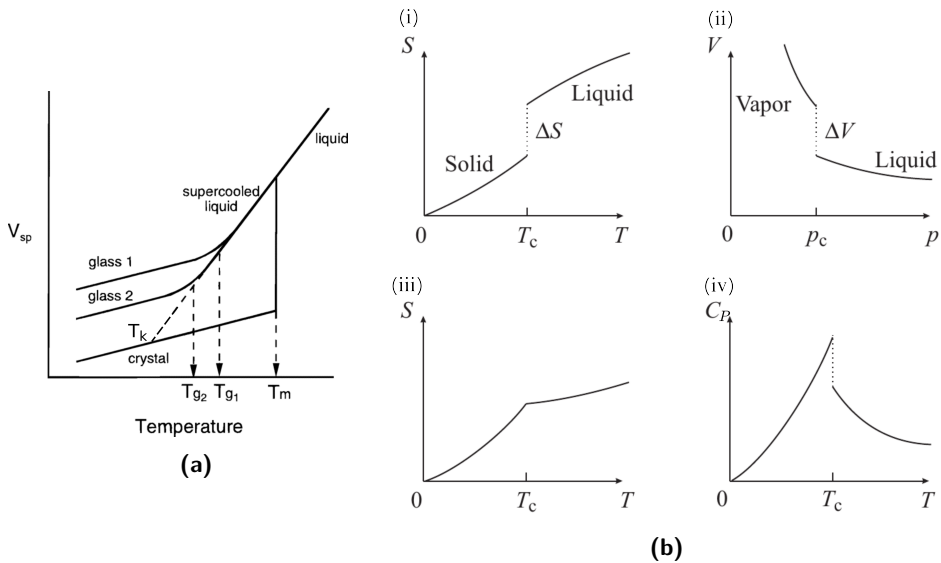
Figure 2.1.: Glass transition and phase transitions: (a) Specific volume of a glass upon cooling demonstrates a glass transition at T_g, different from the liquid-to-solid transition in its crystalline counterpart (*Adapted with permission from* [37]. ©1996, American Chemical Society). (b) First-order (i-ii) and second-order (iii-iv) phase transitions. (*Adapted with permission from* [38]. ©2010, Oxford University Press).

equilibrium transition, rather is an effect of failure of kinetic readjustments due to change in temperatures [37, 39, 40]. The observation that the product of viscosity and total volume is constant with temperature [41] leads to the concept of free volume. One of the popular definitions of free volume of a solid system at a given temperature is the excess measured specific volume compared to its specific volume at 0 K temperature [40]. The glass transition in supercooled liquids is said to originate from the reduction of relative free volume in the bulk [42]. Cohen and Turnbull [35] proposed a model of free volume: the atoms were assumed to be transported into the voids that appeared, when the void volume was greater than a critical volume, and no energy is required to free volume redistribution. The free volume would be negligible in low temperature regimes, but with increasing temperature, the volume gained upon expansion is "free" to be redistributed into the entire bulk of the solid. After the volume is distributed, the

system would attain a minimum free energy configuration [43]. The glass transition is a change in the viscosity, it is not really a physical change. It is for this reason that a glass transition is not considered to be a thermodynamic phase change like melting.

2.1.2. Glass Forming Ability and Energy Landscape

Some popular routes today to synthesise MGs are rapidly-quenched (RQ) by melt-spinning [2], ball-milling [3, 8] and solid-state reactions [44]. The MG synthesis involves accessing a metastable amorphous state, and avoiding nucleation of crystals is not without difficulties. There is hence a need to search for good glass formers, and enhancing the glass-forming ability (GFA). Turnbull [45] proposed criteria to bypass crystallisation when supercooling, one of the most important being the reduced glass transition temperature $T_r = T_g/T_m$, where T_g and T_m are the glass-transition temperature and melting temperature at the composition respectively [45, 46]. It was predicted that glasses around the deep eutectic compositions would have good GFA. For $T_r = 0.5 - 0.67$, the system becomes sluggish in crystallisation at experimental timescales [45].

While Turnbull's criterion is a good rule of thumb for GFA, the experimentally realisable size of metallic glass samples is another challenge. The larger the dimensions of the glass sample, the greater the chance of non-uniform cooling rates, promoting crystallisation within the bulk of the undercooled sample. This greatly limits the size of the MGs. For instance, the first AuSi glass could be made in very small dimensions in the order of 0.1 mm^2 area and 10 μm thickness[1]. The interest to produce glasses of larger critical sizes in the 1990s led to research on bulk metallic glasses (BMG), which are up to several millimetres in thickness [48–50]. In 1999, Johnson [48] developed the first BMGs. Shortly after, it was empirically determined in 2000 by Inoue [50] that the crystallisation in larger glasses could be avoided using the following criteria:

1. *Confusion principle*: Choosing multi-component alloys (≥ 3 components) can cause frustration in the undercooled liquid, delaying crystallisation
2. The difference in radii of atoms should be more than 12-15%
3. Negative heat of mixing amongst the main constituent elements,

These conditions increasing solid/liquid interfacial energy, and make it difficult for atomic rearrangement on a long-range scale. Thereby, the visosity and the T_g increase, and the driving force for crystallisation is reduced. By choosing multi-component systems and along with these empirical rules, Inoue [50] successfully prepared BMG of 72 mm in size. The good GFA of BMGs is attributed to their Arrhenius-like behaviour, demonstrating strong-liquid-like viscosities as classified by the empirical Vogel–Fulcher–Tammann (VFT)

---

[1]Today, industrial production of melt-spun amorphous ribbons of even 150 mm in width is possible [47].

relation [32, 46]. In the quest to produce better glasses, which are also thermally stable, a better understanding of the underlying thermodynamic mechanisms is warranted.

One of the first observations about glass stability was its dependence on the quench rate [51, 52]. Figure 2.1b shows the specific volume behaviour with temperature for a liquid forming a glass. At lower quench rates, glasses can reach a state with lower specific volume, which translates to lower enthalpy and entropy. Furthermore, the glass-transition temperature (T_g) of the glasses reduces when lowering the cooling rates. However, there is a limit on the slowest cooling rate possible in the glasses. Theoretically, at an infinitely slow quench rate, the entropy of the system can be lowered below the entropy of the solid, forming an *ideal glass* [36]. Visually, this can be understood from Figure 2.1a, where the liquid transition is extrapolated to low temperatures, and where the extended (dotted) line meets the crystal entropy is the Kauzmann temperature (T_k). However, this renders the entropy of the liquid to attain a value below that of the crystalline solid at absolute zero temperature. This is called the Kauzmann paradox [5, 32, 36]. A resolution to this entropy paradox was postulated by Kauzmann himself, suggesting that all supercooled liquids must crystallise before the T_k is reached. In actual experiments there is a limit to quench rates possible [36], and at very slow quench rates, the system will crystallise.
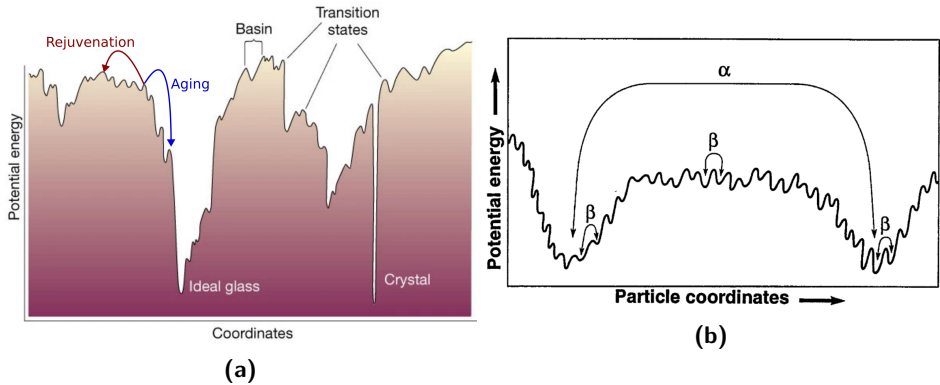
Figure 2.2.: Energy landscape of metallic glasses: (a) The potential-energy landscape of MGs in configurational space, depicted with basins and sub-basins (*Adapted with permission from* [32]. ©2001, SPRINGER NATURE) (b) α and β transitions in configurational space, α relaxations constitute a change of the all the particle coordinates. (*Reprinted with permission from* [53]. ©1995, AAAS).

The synthesis of MGs is evidently complicated because of their inherent metastability, as the preferred states of the systems are either crystalline (at low temperatures) or liquid (at high temperatures). To better understand the process, the system of atoms that constitute the glass can be imagined to have many accessible states, which are potential wells (also called basins) in configurational space—often referred to as a potential-energy landscape (PEL). In Figure 2.2a, an illustration of a PEL is depicted. The various amorphous states are local minima in the PEL, with the crystalline structure at the global minimum of the configurational coordinates. While various processing treatments bring the system to a certain state, it is possible for the system to hop from one state to another by transitions or relaxation processes. This is visualised in Figure 2.2b. β-relaxations are the hopping of a system amongst subbasins, and involves a local rearrangement of atoms. The larger and relatively slower hopping events, which constitute a rearrangement of the entire system, are referred to as α-relaxations, transporting a system to an entirely different basin in the PEL.

In order to stabilise the glasses at the nearest local minimum, sometimes heat-treatment processes are implemented. A low temperature thermal cycling such as annealing below T_g for instance, lowers the enthalpy and potential energy of the glassy system. This is referred to as aging. In contrast, when a treatment of the system increases the total energy of the system, the process is called rejuvenation [54, 55]. The rejuvenation and aging processes are depicted in Figure 2.2a.

2.1.3. Structural Models for Amorphous Metals

As mentioned in the previous section, a system can attain multiple glassy configurations (see Figure 2.2); the thermodynamic state of a glass depends upon the formation routes—and hence affects its properties. This leads to the age-old problem of understanding the structure of MGs, to explore structure-property relationships. At a first glance, glasses appear to have no particular structural order, only to be characterised by their general lack of LRO. A unifying structural definition of the amorphous structures, requires understanding them beyond simply defining the lack of LRO. Recent studies discuss models in which metallic glasses possess ordered substructures [49, 56, 57]. The first kind, termed as short-range order (SRO) is defined over the length scales of ≤ 0.5 nm. SRO is the structure at the level of an atom and its first and second nearest neighbours. Beyond the SRO, the medium-range order (MRO) is defined at length scales of ~ 1 nm, and describe how the SRO-motifs pack together. An experimentalist may already be familiar with these terms upon calculating radial distribution function (RDF) (described in Chapter 3) from electron diffraction, x-ray diffraction (XRD) or extended x-ray absorption fine structure (EXAFS), however the RDF provides only an average picture of the atomic structure. A description of the local structure of atoms

provides essential clues to understand the amorphous MGs, and finds value particularly in Chapters 5 and 6 of this thesis.

The local atomic arrangements and their contribution to the packing and, eventually, to the stability of glassy structures have been discussed in previous studies. A first theory of SRO in random packing in solids was from empirical evidence of compressing densely packed plasticine (modelling clay) balls by Bernal [58], in connection with an investigation of the structure of liquids. It was noticed that the hard spheres upon compression deformed into a wide variety of polyhedra, which were mostly made up of pentagonal faces. The convex polyhedra so formed in the plasticine models could also be constructed in atomic structures, as shapes enclosed by planes are drawn to bisect distances between every geometrical neighbour of all the atoms [58, 59]. Such a construction has been known in the mathematics and physics communities by various names, such as the Voronoi tessellation [60, 61], Dirichlet region [62], Delaunay triangulation [63] or as a Wigner-Seitz cell [64]. The Bernal plasticine model for irregular packing in liquids, fails to describe multicomponent glasses with large size differences between the atoms, and also the realistic atomic systems, which interact differently than hard spheres. Another model was proposed by Gaskell [65] for metal-metalloid systems, arguing that the nearest neighbour units resemble the structure of the crystalline phases at the same compositions. The structure factors of the glasses obtained from this model were in agreement with those obtained from neutron diffraction experiments. However, this model did not support metal-metal glass systems, and failed to explain the stability of BMGs in their supercooled states [66].

In recent times, Miracle [67] proposed an alternative theory for metallic glasses. He supposed that the structure of glasses could be constructed by efficient packing of solute-centered clusters (or solute clusters) in face-centered cubic (FCC) or hexagonal close-packed (HCP) layouts, giving rise to the efficient cluster packing (ECP) model. By this model, the solute atoms (α type) exist inside the solvent atom clusters (Ω type), and also in the cluster-octahedral interstices (β type) and cluster-tetrahedral interstices (γ type) depending upon the ratio of atomic radii of the solute and solvent atoms. This makes up four topologically distinct classes of atoms in the glass. The solute clusters were deemed to be predominantly face-sharing, but also exhibit edge- and vertex-sharing to accommodate for internal strains. The model theorised that the solute clusters in turn were packed in FCC and HCP configurations, giving rise to the MRO. This ECP model was successful in predicting the compositions and also MRO up to 1 nm length scale. However, this model has some major deficiencies. The model fails to explain the evolution of the local structure of MGs, which are known to vary with the quench rate. Furthermore, the ECP is a static model, so it also can not explain the dynamical behaviour of glasses.

A more recent method to describe simulated local amorphous structure and SRO is

the evaluation of the local topological order of the atoms. Unlike the Miracle [67, 68] approach, first an amorphous structure is prepared either by molecular dynamics (MD) or reverse Monte Carlo (RMC) simulations. Then, a Voronoi tessellation is performed to study the topology [56, 57]. This results in a broad distribution of polyhedra of various shapes and sizes, reminiscent of the polyhedra obtained by Bernal [58]. Such a method has various advantages over the Miracle model, i.e., the dynamic evolution of SRO can be studied.

Initially, Honeycutt and Andersen [69] calculated the stability of free-standing agglomerations of 13 atoms in size—arranged in an icosahedral packing with five-fold symmetry. The stability in supercooled liquids was suggested to be a result of icosahedral clusters by Frank [70]. It was later reported that the occurrence of icosahedral packing–or, full-icosahedral (FI) order—can be correlated with increased packing fraction in model metallic glasses [71]. Recently, performing Voronoi tessellation on simulated glasses [56, 57] showed that the partitioned three-dimensional (3D) space assigned to atoms were equivalent to Kasper polyhedra [72, 73], which constitute the local SRO in MGs. Sheng et al. [56] showed that the glass structure need not be made from a single FI motif, but that every alloy system has distribution of coordinations, dominated by a certain coordination polyhedra. For the case of $Cu_{64}Zr_{36}$ MGs, icosahedral atomic packing was observed to be the highest occurring structural motif [74, 75]. Furthermore, for $Cu_{50}Zr_{50}$ MGs, it was observed that these FI environments were strongly spatially correlated to each other [76, 77]. For $Cu_{50}Zr_{50}$ MGs quenched at a faster rate, less FI and icosahedral-like (ICO-like) packing or icosahedral-like order (ILO) has been found [78].

Icosahedral order dominates local order and influences packing. The link between stability (structural and thermodynamic) and SRO in MGs is a very well-studied topic in literature. The work by Cheng et al. [79] unequivocally clarifies the relationship between increased FI SRO and increased thermodynamic stability in Cu-Zr MGs. Additionally, there is also work on geometrically-unfavoured motifs (GUM), which are SRO structures that are known to be the most likely participators in shear transformations, contributing to structural instability of MGs [74]. Icosahedral SRO units are known to be least likely to be GUMs.

In addition to giving a description of the topological SRO, Sheng et al. [56] proposed a model for MRO. They suggested that in dilute solutions, unlike the proposed SRO-units by Miracle [67], it would be the solute clusters as derived from the Voronoi that would pack in FCC/HCP/icosahedral-stacking to form a MRO. When the solute concentration increases above ~20%, they observed that all of the solute atoms can no longer be placed at the centre of a solute-cluster being completely surrounded only by solvent atoms. In this case, some solute atoms are expected to be first nearest neighbours. Consequently, a different kind of MRO forms in solute-rich compositions, comprising of strings of solute atoms. Another recent work discusses the aggregation of FI-clusters to form chains
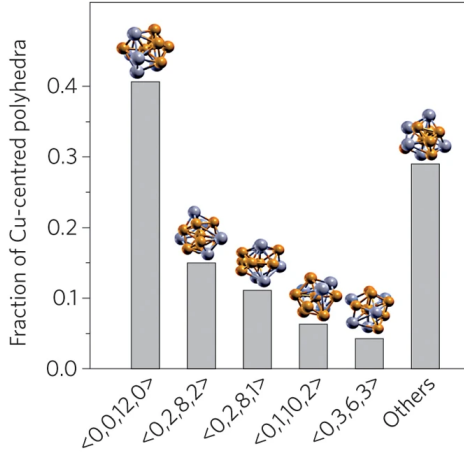
Figure 2.3.: Short-range order in metallic glasses: The Voronoi tessellation method [56, 57] helps identify the distribution of SRO polyhedra indexed using Schläfli notation (discussed in further detail later in Section 3.2.2). In $Cu_{64}Zr_{36}$ glasses, FI-polyhedra ($<0\ 0\ 12\ 0>$) are the prominently occurring SRO motifs.   (*Reprinted with permission from* [54]. ©2015, NATURE PUBLISHING GROUP).

present also with interpenetrating icosahedra to exhibit a cross-linked MRO network [80–82].

2.2. Nanoglasses

The previous section elaborates on the various aspects of the conventionally prepared MGs. Alternative routes to preparing glasses have been explored to find new ways to control properties of amorphous materials. As early as 1977, it was expected by the glass community that vapour-deposited materials should have different structures than their monolithic counterparts, due to the effects of boundary conditions on the nanoparticles or atoms being deposited during synthesis [83]. The discovery of nanocrystalline materials (NCM) [84]—made from compaction of nanometre-sized grains—catalyzed similar advances in noncrystalline solids. Analogous approaches to the NCM powder processing, could then be used to generate glasses with tailorable defect microstructures.
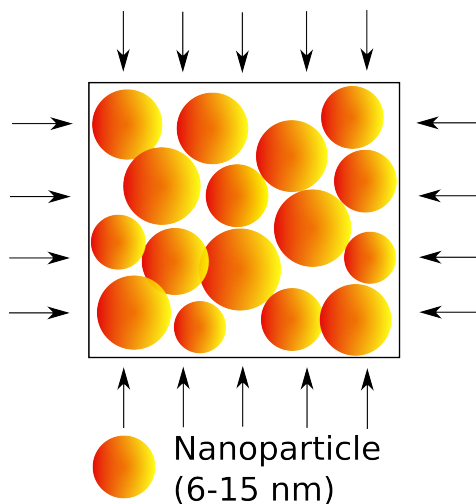
Figure 2.4.: Schematic of nanoglass formation by compaction: Illustrated here is the hydro-static compaction of particles produced via IGC, which leads to the synthesis of nanostructured NGs.

Gleiter [84] envisioned a new type of non-crystalline solid made from the consolidation nanometre-sized amorphous nanoparticles, and termed it as nanoglass (NG). He hypothesized that in compacting a multitude of glassy nanoparticles, it would be possible to create a glass with enhanced free volume, which exist amongst in the regions of contact (or interfaces) of adjacent nanoparticles. Expecting defective coordinations at the interfaces, Gleiter propounded that the interfacial regions should be structurally and/or chemically distinct from the cores [84, 85]. The SRO and properties of the NGs, he said, must then deviate from a RQ MG of a similar chemical composition.

2.2.1. Experimental Studies

The group of Gleiter successfully synthesised a PdFeSi NG [10] in 1989. The nanoparticles were prepared by thermal evaporation and inert-gas condensation (IGC) under ultra-high vacuum (UHV), and later consolidated at gigapascal orders of pressure. The structure of the PdFeSi NG was evaluated using the Fe-Mössbauer spectroscopy (MS) technique. In contrast to the RQ MG, which shows a single broad peak in the quadrupole splitting (QS) distribution, it was observed that the NG shows two peaks [10]: One peak was

similar to that of the RQ MG, and hence was interpreted to be originating from the core regions of the glassy nanoparticles, as the NG core was expected to have similar structure to the RQ MG. The second peak of the QS distribution was unique to the NG. This additional component was attributed to the interfaces formed amongst the consolidated nanoparticles [10]. In addition, the MS indicated the interfacial region to possess a reduced electron density. NGs of various chemical compositions, such as Au–Si, Au–La, Fe–Si, La–Si, Pd–Si, Ni–Ti, Ni–Zr and Ti–P, were also synthesised [15].

$Sc_{75}Fe_{25}$ NGs were also investigated using positron annihilation spectroscopy (PAS) [13], as depicted in Figure 2.5a. The Fe-Sc NGs indicated two distinct positron lifetimes, one of which was the same as of the RQ MG, and the second lifetime was present only in the NGs and interpreted as originating from the interface regions. The intensities of the two lifetimes were used to indicate that the as-prepared NG consisted of 65 vol% glassy cores and 35 vol% interfacial regions. Moreover, this $Sc_{75}Fe_{25}$ NG demonstrated enhanced plasticity in comparison to RQ MGs, this was also attributed to the presence of glass-glass interfaces.

The Fe environments in Fe-Sc NGs were studied extensively to identify core and interfaces. The $Fe_{90}Sc_{10}$ NG in particular was the subject of many reports indicating the presence and peculiar properties of interfaces [14, 17, 24, 86, 87]. Using high energy XRD, it was found that the number of Fe nearest neighbour atoms in the interfacial regions of the $Fe_{90}Sc_{10}$ NGs is lower than in the corresponding RQ MGs [86].

It was also demonstrated that the magnetisation curves of the NGs vastly differed from RQ MGs. While the $Fe_{90}Sc_{10}$ MG was paramagnetic at 300 K, the corresponding NG was ferromagnetic with a paramagnetic component (See Figure 2.5b), indicated by its magnetisation not fully saturating even at 4 T [17]. Like in reference [10], once again the MS experiment, shown in Figure 2.5c, indicated a heterogeneous magnetic structure in the $Fe_{90}Sc_{10}$ NG (there was an occurrence of two sub-spectra: a paramagnetic component and a ferromagnetic sextet). It was also proven that these fascinating properties of the NG were observed only after the nanoparticles were compacted, and not as a loose powder, strengthening the idea that the formation of interfaces resulted in the special properties. The concept of interfaces is illustrated in Figure 2.6, highlighting the idea that the cores and interfaces, while both amorphous, are structurally distinct from one another.

The $Fe_{90}Sc_{10}$ NG was further investigated with electron energy loss spectroscopy, which indicated a surface segregation of Fe in the glassy nanoparticles. The surface segregation leads to a chemical heterogeneity in the structure of $Fe_{90}Sc_{10}$ NG [87]. Such a surface segregation was explained to arise from both the difference in surface energies of Fe and Sc, and the enthalpy of mixing. A segregation model in the Fe-Sc NGs was proposed based on experimental results of small- and wide-angle X-ray scattering [24].
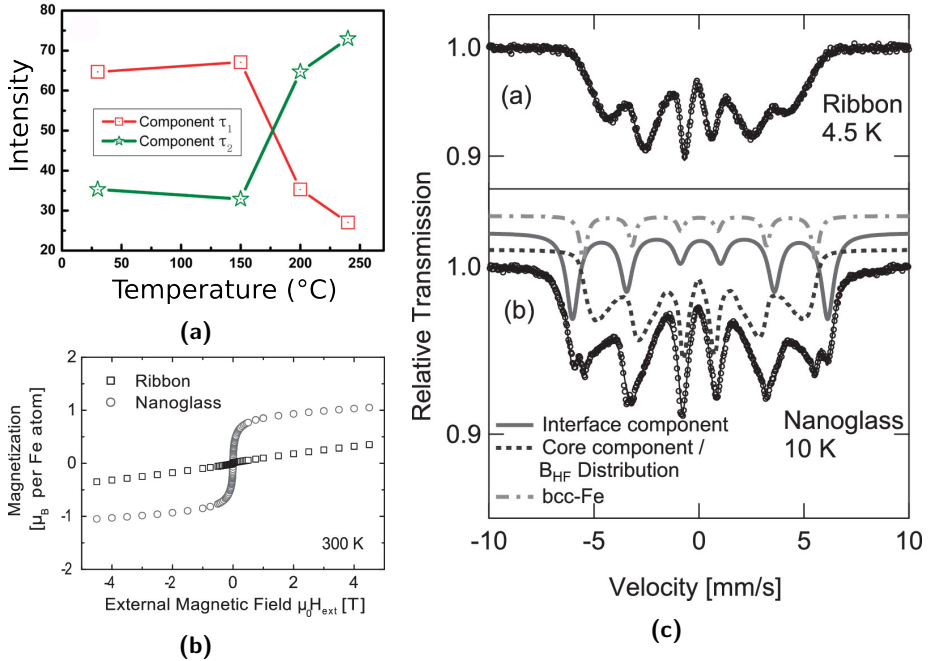
Figure 2.5.: Indirect evidence for interfaces in FeSc NGs: (a) Relative intensities of two positron lifetimes from PAS of $Sc_{75}Fe_{25}$ NG; τ_2 was interpreted to arise from interfaces and increases in intensity with annealing (*Adapted with permission from* [13]. ©2012, AMERICAN CHEMICAL SOCIETY). (b) Magnetisation and (c) MS spectra of $Fe_{90}Sc_{10}$ NG indicate a new distinct Fe-environment in NGs (*Reprinted with permission from* [17]. ©2013, AIP PUBLISHING LLC).

Recently, $Cu_{50}Zr_{50}$ NGs were also prepared using magnetron sputtering as opposed to thermal evaporation [18, 88]. These NGs were characterised to exhibit higher T_g, and consequently, higher thermal stability as compared to the RQ MGs. Furthermore, a chemical segregation present in the interfaces facilitated better stability against crystallisation (i.e., higher crystallisation temperature T_x) as well. Nanoindentation studies also revealed that the NGs demonstrated better plastic behaviour (homogenous deformation as opposed to formation of shear bands), and also a higher hardness (Young's
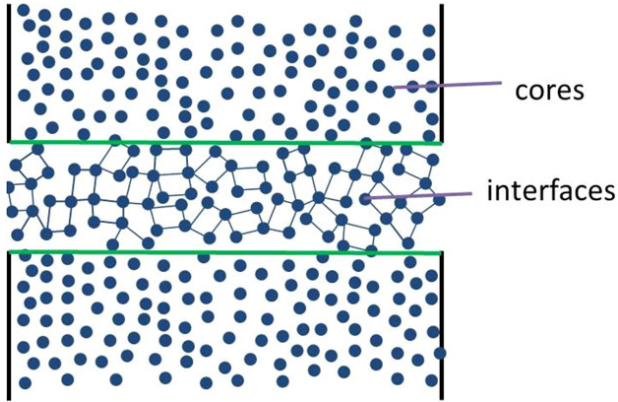
Figure 2.6.: Proposed core-interface structure of nanoglasses: The processing of a NG is hypothesised to form the two core and interface glassy phases—both of which resemble the amorphous structure of RQ MGs in terms of exhibiting no LRO. However, the SRO and MRO of core and interface differ from one another. (*Reprinted with permission from* [12]. ©2018, WILEY).

modulus) than MGs. The shear transformation zones (STZ) of NGs were also measured to be ∼3.8 times larger in volume as compared to melt-spun MGs. The segregation of Cu to the interfaces in the NG, as evidenced by atom-probe tomography (APT), was used to explain the enhancement of T_x and T_g in the NGs.

2.2.2. Simulation Models

In the previous subsection, the progress made in the NG experimental investigations was discussed. To aid these reports, several independent MD simulation models of NG have been made, predominantly by the groups of Karsten Albe [19, 20, 22, 23, 89–92], Jason Trelewicz [21, 93] and Paulo S Branicio [94–97]. A first report of NG simulations was made by Şopu et al. [19], which demonstrated a compaction protocol for glassy Ge nano-sized spheres at 300 K temperature. The investigators observed that the interfaces formed with lesser densities than the cores. However, their attempts at simulating a $Cu_{50}Zr_{50}$ NG at 300 K failed as the interfaces completely vanished after compaction, indicating that the mechanical and diffusional properties of the materials influenced the stability of interfaces.

Later, in 2011, Ritter et al. [23] were successful in simulating a planar glass-glass interface in $Cu_{64}Zr_{36}$ MGs, which were also stable in MD timescales. The interfaces were characterised with defective local FI SRO, and present with a 1-2% excess free-volume. The interfaces were also found to promote shear band formation during tensile deformation, indicating a mechanism to explain enhanced plastic deformation in NGs. Such planar glass-glass interfaces were further studied in $Cu_{64}Zr_{36}$ and $Pd_{80}Si_{20}$ systems, also with an elemental surface segregation model [22]. It was found that segregated interfaces were found to be better packed as compared to ordinary interfaces, with higher topological SRO, number and electron densities. The interfaces in NGs can hence be considered as a structurally stable interphase between the core regions. In the same work, a model was proposed to simulate nanoparticles (precursors to NGs) with chemical segregation. The nanoparticles, derived from cutting a sphere out of a glassy bulk and subsequent heat treatment, were found to have similar energetic states as a cluster derived from an IGC simulation [22]. The cohesive energies of the Zr in $Cu_{50}Zr_{50}$, and Si in $Pd_{80}Si_{20}$ were found to drive their segregation to the core regions, while the complementary elements segregated to the surface. This method of deriving a glassy cluster from the bulk of an RQ also offers the advantage of controlling the nanoparticle size, as compared to other successful IGC-based models reported for generating Ge clusters [89] and $Cu_{64}Zr_{36}$ clusters [96].

A contemporaneous work to the nanoparticle segregation model discussed above [22] was an investigation by Danilov et al. [98], that reported a model for IGC of nanoparticles of an amorphous Kob-Anderson system [99]. This model, which described atomic forces in a Lennard-Jones (LJ)-like manner substantiated the presence of a distinct chemical segregation in the cores and shells of the IGC-nanoparticles. Furthermore, a compaction model was also proposed to create NGs from the amorphous IGC-nanoparticles. The Kob-Anderson model of IGC-nanoparticles, and the NGs made from them were found to demonstrate an enhanced thermal stability in comparison with the RQ MGs [98].

Adjaoud and Albe [20] further improved the realistic simulation of the NG-compaction model in $Cu_{64}Zr_{36}$ and $Pd_{80}Si_{20}$ systems by consolidating a polydisperse distribution of nanoparticles, with an empirically derived embedded atom model (EAM) interatomic potential. Further details of EAM are given in Section 3.1.2. The consolidation pressure was shown to have significant influence on the porosity and microstructure of the NGs. At ~5 GPa of pressure, the porosity was seen to considerably disappear. Unlike in the work of Şopu et al. [19], the temperature of the system was chosen to be 50 K. The closing up of pores was accompanied by the formation of interfaces, indicated by the local shearing of surface atoms of the nanoparticles. The interfaces constituted of surface atoms of the nanoparticles, and possessed defective SRO compared to the cores (for the $Cu_{64}Zr_{36}$ and $Pd_{80}Si_{20}$ systems). In $Cu_{64}Zr_{36}$ NGs, the presence of chemical segregation in the nanoparticles led to the formation of interfaces which were chemically heterogeneous

from the core regions. This heterogeneity from the segregation was found to be more energetically favourable in the $Cu_{64}Zr_{36}$ nanoparticles, than in the interfaces.

Similar NG models were made by Cheng and Trelewicz [21, 93] in which a compaction model for a monodisperse distribution of nanoparticles in a patterned arrangement was described, much like the work of Şopu et al. [19]. In $Cu_{64}Zr_{36}$ glasses, the interface SRO and width in NGs was shown to increase with the temperature at which the nanoparticles were consolidated, and even annealing temperatures after consolidation [21, 93]. In these works, the interfaces remained stable even up to 800 K temperature[2], hinting that the attempts of $Cu_{50}Zr_{50}$ NGs by Şopu et al. [19] could have failed due to lack of availability of a good interatomic potential. Reduced average flow stress and shear localisation factor [102] were observed in the 2.5-nm and 5-nm grain size NGs, hinting at a stable plastic flow and scaling of elastic properties with nanoparticle size.

Another alternative means to simulating NGs that exists in literature is the tessellation-based approach. The previously discussed works fill a box with nanoparticles and compact them [19–21, 90, 93]. In the tessellation approach, first a Poisson-Voronoi tessellation is applied to segment the simulation box, and then segmented partitions are filled with amorphous glassy "grains" [94, 95, 97, 103]. An external hydrostatic pressure is applied on this configuration. The resulting grain microstructure tends to resemble that of nanocrystalline materials albeit with amorphous grains. While this interesting approach was used to explain some mechanical behaviour of the NGs, it is quite different from the compaction model and also from the experiments. Next, the "amorphous grains" are chunks of 3 nm particles on average, which are aspherical and fill the space efficiently, rendering the grains to not deform realistically as would the spherical clusters. These tessellation-based NG simulations are not discussed in the thesis beyond this section.

2.3. Cluster-assembled Metallic Glasses (CAMGs)

2.3.1. Cluster-ion Beam Deposition and Cluster-assembled Materials (CAMs)

Advances in research on nanocomposites such as NCMs and NGs inspired the exploration of cluster-assembled materials (CAMs). This new class of materials are built from clusters of atoms, in UHV, and have been realised in experiments [104–106]. One of the initial works from 1991 reported the development of a cluster-ion beam deposition (CIBD) apparatus. This apparatus epitaxially deposited a beam of cluster ions with a large size range (25-1600 atoms) onto Si substrates. The ion guided deposition process was

---

[2]This temperature is close to $Cu_{64}Zr_{36}$ T_g, although it is not clear if this temperature is above or below the simulated glass-transition temperature, which is shown to vary with the choice of the EAM potential [100, 101].

successful in preparing films mostly from the smaller clusters in the distribution [107], as only a few of the larger clusters were ionised.

CAMs were also prepared (and simulated) by low energy deposition of atomic clusters [108], resulting in highly porous films which grow in fractal-like patterns due to random stacking. Another extensive review of CAMs discusses the cluster-assembly method for tailorability of superconductivity or charge transport in fullerene-based materials, for the tunability of bandgaps in cluster-based semiconductors, and for the devising of superlattices of size-selected inorganic nanocrystals to enhance conductivity and charge mobilities [109]. Although CAMs have been studied by various research groups, the detailed mechanisms that affect films deposited from CIBD sources are still unclear from the experiments.

Computer simulations of ion-beam depositions provide preliminary insights into mechanisms of cluster deposition. The first theoretical studies on CIBD linked cluster deposition energy to the epitaxy of the films, and suggested that the density of the films increases with impact energy [110, 111]. Succeeding atomistic deposition simulations of covalent systems correlated change in bonding and lattice distortions with deposition energy [112]. Simulations of molybdenum-cluster depositions provided insights into the morphologies adopted by the CAMs [113, 114]. More recent deposition simulations of Cu clusters onto a Si substrate also exist [115, 116]: describing the variation of film epitaxy, stress, and surface roughness with the deposition energy of cluster-assembly. However, a deeper understanding of the local atomic structures adopted in metallic CAMs is still lacking.

2.3.2. State of Art: Size-selected CAMs and CAMGs

As seen in the previous section, a control over the local chemistry, morphology, and even microstructure in nanocomposites can be envisioned with precise cluster-assembly. Kartouzian et al. [28, 29] synchronised the idea of CAMs with metallic glasses, and conceptualised the idea of cluster-assembled metallic glass (CAMG). By designing MGs meticulously with size-selected clusters as building blocks, Kartouzian expounded the possibility to better understand the structure of MGs. His proposed method was successful in creating an amorphous CAMG, but it was presented with no discernible features and no concrete method of investigating them. The quest of preparing CAMGs as a means to fabricate fully tailorable amorphous nanocomposites remained unexplored. Aided by experience from NG experiments, the synthesis of size-selected CAMs and CAMGs for the first time was achieved by the group of Hahn with the development of a unique UHV apparatus to perform CIBD [31, 117, 118].

Figure 2.7 depicts a variety of cluster-based nanocomposites that can be synthesised in the UHV machine. The CAMs are made by depositing crystalline or amorphous nanoparticles
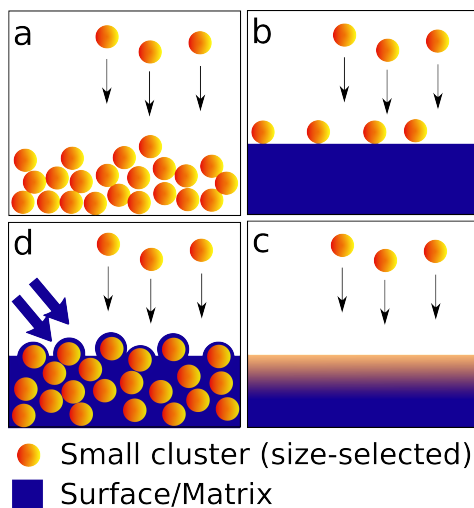
Figure 2.7.: Various CAMs made possible by UHV CIBD: Illustrations of the types of nanocomposites. The cluster-assembly can be used to create (a) purely cluster-composed films, or (b) cluster decorated surfaces. (c) With high impact energies, surface alloys can be created. (d) By co-deposition, clusters can be embedded in a matrix material.

onto a substrate placed within the UHV CIBD apparatus[3]. A purely cluster-composed CAMs (Figure 2.7a) can be made with both monodisperse and polydisperse clusters. The clusters may be deposited with a low deposition energy, to create cluster decorated surfaces (Figure 2.7b), or directed with high energies onto a substrate to make surface alloys (Figure 2.7c). Furthermore, in the UHV CIBD apparatus, clusters can be co-deposited along with physical-vapour deposition (PVD) of a matrix material from a thermal evaporation source. In doing so, clusters deposited at low energies can be embedded in matrices (Figure 2.7d). The co-deposition serves an additional function i.e., to deposit a capping layer on any kind of the CAMs as protection against oxidation. Cluster-composed matrices [31, 118, 119] have been shown to demonstrate tailorable magnetic properties by varying cluster-size and cluster-concentration in the matrices. The embedding of clusters in a matrix at low deposition energies also promises the potential to engineer multiphase nanocomposites with elements that are known to be miscible

---

[3]Further details regarding the UHV apparatus are discussed in detail in the works of Fischer [117, 118]

in thermodynamic equilibrium. Conversely, at high deposition energies, an immiscible system can be made miscible.

2.3.3. Initial Studies on CAMGs

As mentioned before, CAMGs are a special class of the CAMs. Initial attempts to synthesise CAMGs were by the deposition of 10-16 atom sized clusters of varying composition, to create a locally heterogeneous chemical structure. Although the films made were characterised to be amorphous, a more detailed study of structure–property relationships was not reported [28, 29].

Previous experiments on Fe-Sc NGs made in the Hahn group [14, 17], however, confirmed that the magnetism studies can shed light on the structural information. Hence, the study of size-selected $Fe_{80}Sc_{20}$ CAMGs was a necessary step in understanding the nature of amorphous structures made from cluster assembly [30]. $Fe_{80}Sc_{20}$ CAMGs of ∼800 atom sized $Fe_{80}Sc_{20}$ clusters were prepared at three different deposition energies (50, 100, 500 eV per cluster), and coated with a Mg layer to prevent oxidation. The samples were studied by energy-dispersive x-ray spectroscopy (EDX) to confirm chemical compositions. Although the Mg capping layer posed a challenge to characterise the CAMG films with transmission electron microscopy (TEM), the samples were found to be amorphous with synchrotron XRD [30]. X-ray absorption spectroscopic studies were conducted to ascertain the average local atomic structure of the constituent atoms.

The structural and magnetic characteristics of $Fe_{80}Sc_{20}$ CAMGs are described in Figure 2.8. X-ray absorption studies were performed at a synchrotron facility to study the fine structure in the extended (EXAFS) or the near-edge region (x-ray absorption near edge structure (XANES)). The normalised Sc K-edge XANES spectra of the three CAMGs, an RQ MG ribbon of the same composition, pure metallic Sc, and Sc_2O_3 are all depicted in Figure 2.8a. The K-edge, i.e, the first inflection point in the energy absorption spectra of the CAMGs and the MG were found to be lower than the Sc_2O_3 K-edge, indicating that the CAMG samples were not oxidised[4]. Furthermore, the spectra in the CAMGs and the MG ribbon were observed to be dissimilar, hinting at differences in local structures.

In Figure 2.8b, the Sc K EXAFS spectra of the three CAMGs and the RQ MG ribbon are compared with pure metallic scandium. The fading of EXAFS oscillations in k-space was identified as an indicator of amorphous structure. The oscillations in the EXAFS spectra of the three CAMGs differ from that of the MG ribbon, indicating once again that the local structures in the cluster-assembled samples are different from RQ MGs.

---

[4]The X-ray absorption energy increases with increase in oxidation state.
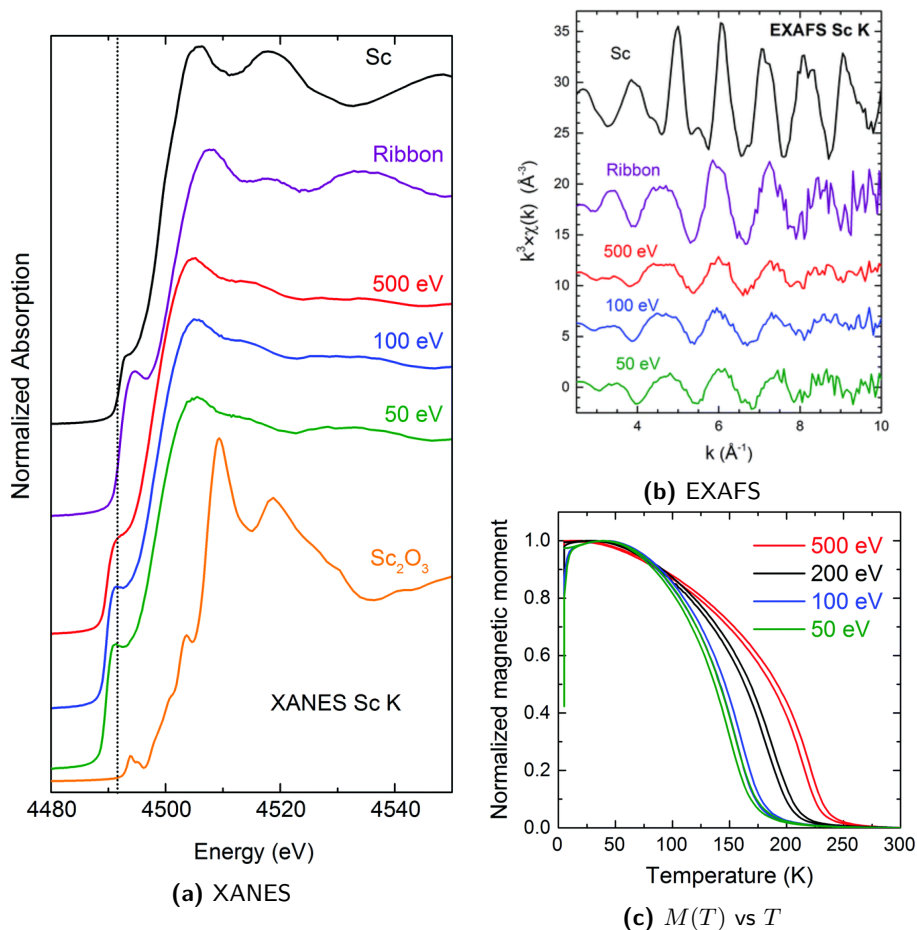
Figure 2.8.: Experimental characterisation of Fe$_{80}$Sc$_{20}$ CAMGs: (a) The XANES spectra show evidence of no oxidation. (b) The EXAFS spectra of CAMGs are distinct from that of the amorphous Fe$_{80}$Sc$_{20}$ RQ MG ribbon. (c) Curie temperature (T_C) varies with deposition energy in CAMGs. (*Reprinted with permission from* [30]. ©2019, ROYAL SOCIETY OF CHEMISTRY).

The magnetic behaviour of four $Fe_{80}Sc_{20}$ CAMGs of impact energies 50, 100, 200, and 500 eV per cluster are described in Figure 2.8c. Firstly, a paramagnetic to ferromagnetic transition was observed in all samples. When the impact energy is reduced from 500 eV per cluster to 50 eV per cluster, the magnetic transition temperature or the Curie temperature (T_C) shifts by 60 K. This result was surprising, as only a change in the impact energy for the CAMGs can result in significantly different T_C. Based on the increase in nearest neighbour distances from the EXAFS data, Benel et al. [30] speculated that the increase of T_C, which is known to correspond to an increased strength of the magnetic exchange interactions, was a result of an increase in the number of the Fe nearest neighbours. The study of $Fe_{80}Sc_{20}$ CAMGs prepared via CIBD has demonstrated the opportunity to tailor the local atomic structure and the T_C by varying the deposition energy. The astounding promise of the CAMGs is the variation of properties in a glass while keeping the macroscopic composition constant.

3. Methods

As discussed in Chapter 2, simulating a metallic glass (MG) is an effective route to understanding its structure-property relationships. Atomistic simulations complement experiments by providing insights into functional and mechanical behaviour. Traditionally, MGs have been simulated using atomistic classical molecular dynamics to understand their structure-property relationships and time-evolution of local atomic processes [79, 120], and local atomic short-range order (SRO) and medium-range order (MRO) [56]. In the current chapter, the fundamentals of the classical molecular dynamics method, as well as techniques used to characterise the simulated samples are discussed.

3.1. Molecular Dynamics Simulations

3.1.1. Overview

The many-body approach is adopted to describe the mechanisms of a system of atoms or molecules. The most accurate solution would be achieved with a quantum mechanical treatment. However, beyond a two-body problem, an analytic quantum mechanics solution is not possible. While the local density approximation class of density functional theory (DFT) methods can help predict structure and thermodynamics, they are highly computationally intensive; one is limited to systems of not more than hundreds of atoms for the simulations to complete in a reasonable time with the computing resources available today [121]. A reasonable compromise is to perform molecular dynamics (MD) simulations by treating atoms as the lowest level of discretisation to study the properties of materials. Today, MD simulations of metallic glasses are performed using readily available codes such as large-scale atomic/molecular massively parallel simulator (LAMMPS) [122, 123]. The basics of the techniques implemented in the MD solvers are addressed.

The Born–Oppenheimer approximation [124] allows one to treat the dynamics of the nuclei and electrons of atoms separately due to their large mass differences. Consequently, in the many-body problem, the heavier and slowly moving nuclei are described as point masses using Newton's equations of motion. The electrons are assumed to adapt instantaneously

to change in the nuclei. For studies in which one is interested in atomic arrangements and interactions, the atomistic molecular dynamics methods allows discretisation of simulation to atomic scales [1]. Being able to calculate both the particle velocities and trajectories, MD emerges as a powerful tool to not only observe microscopic processes, but also compute macroscopic experimental observables of a given system.

For a system of N-particles of masses $\{m_i\}$ with a set of initial positions $\{\vec{r_i}\}$ and momenta $\{\vec{p_i}\}$, the time evolution of the system can be obtained by solving for the Newton's equation of motion:

$$\vec{F_i} = m_i \frac{\partial^2 \vec{r_i}}{\partial t^2}, \ \text{i=1...N} \tag{3.1}$$

The forces $\vec{F_i}$ on the particles are obtained from the gradient of a potential $V(\{\vec{r_j}\})$

$$\vec{F_i} = -\vec{\nabla} V_i(\{\vec{r_j}\}), \ \text{i,j=1...N.} \tag{3.2}$$

The mathematical function for $V(\{\vec{r_j}\})$ is decided based on the type of interatomic interactions being modelled. The equations of motions are then time-integrated over short time steps δt. The aspects of the interatomic potentials and the technique of performing the time-integration are discussed in the following sections.

3.1.2. Interatomic Potentials

As seen from Equations 3.1 and 3.2, the time-evolution of the system in MD are crucially dependant on the interatomic potentials (also called force-fields). Different mathematical functions have been prescribed to describe the various physical interactions. The simplest kind of interatomic potential is the Lennard-Jones (LJ) potential and it is a pair potential taking the following form:

$$U_{ij}(r_{ij}) = 4\epsilon \left[\left(\frac{\sigma}{r_{ij}} \right)^{12} - \left(\frac{\sigma}{r_{ij}} \right)^6 \right], \tag{3.3}$$

where U_{ij} is the interatomic potential between the ith and jth atoms, r_{ij} is the distance between the particles, ϵ is the strength of the potential, and σ is the distance between the two particles at which the potential energy between them is zero [125]. The LJ potentials

---

[1] Further approximations, such as coarse-graining: where certain molecules or functional groups are treated as one unit, or implicit solvent models: where the solvent interactions in a solute-solvent system are implicit in the equations of motion, are also employed to further reduce simulation costs.

models the interatomic forces in a simple fashion: The first term, contributing energy to the system replicated the close-range repulsions. The second term contributes to the attractive forces. The balance between the two terms results in the binding of atoms. This definition of an interatomic potential was adopted for supercooled liquids [99], and it still used as a model system for glass simulations [98].

However, such a pair potential does not include the many-body effects that occur in metallic systems. Daw et al. [126], in 1993, elaborate on the limitations of the pair potential and a solution for it. In metals, bonds between atoms are not independent of each other. Consequently, the pair potentials do not replicate metallic bonding because the cohesive energy $E_{coh}()$ does not scale with negative of coordination number (Z), which is the expected result from pair potential. Rather, E_{coh} scales more weakly as $E_{coh} \propto Z^{1/2}$ [126].

To overcome the limitations discussed above, and to capture many-body interactions in metallic solids, the embedded atom model (EAM) model was proposed by Daw and Baskes [127]. This model takes into consideration the realistic forces on a central atom resulting from the sea of electrons from the atoms that the central atom is embedded in. Each atom is considered as an impurity in the host of the other atoms. Now, the EAM potential U_{EAM} takes the following form:

$$U_{EAM} = \sum_i \mathcal{F}_i(\rho_i) + \sum_{i \neq j} \phi_{ij}(r_{ij}) \tag{3.4}$$

where $\mathcal{F}_i$ is the embedding energy functional, ρ_i is the average electron density of the ith atom, ϕ_{ij} is the pair-wise interaction, and r_{ij} is the scalar distance between the i and j atoms. The general form of the functional $\mathcal{F}$ and ϕ are not known, but are fitted to replicate elastic properties known from experiments.

The EAM interatomic potential used in this thesis was developed by Mendelev et al. [100, 101]. The potential form used was of a Finnis–Sinclair-type: which differs only slightly from the original Daw and Baskes [126, 127] formalism in that the electron density ρ_i is element dependant. These interatomic potentials are semi-empirically derived; the Cu-Zr potential utilised in this thesis [101] was developed from pure Cu and Zr potentials, modifying the ρ_i to fit to the experimental liquid density, mixing enthalpy, and radial distribution function (RDF) [100] (Information on RDF is given in Section 3.2.1).

Later, the CuZr EAM potential was improved to predict the Laves phases better by fitting the EAM partial radial distribution function (PRDF) to those from experiments and *ab-initio* MD simulations. Only the terms associated with Cu-Zr interactions were

modified; the Cu-Cu and Zr-Zr interactions remained unchanged [101]. Such semi-empirical potentials are system specific and provide reasonably accurate results for large system sizes.

Although the EAM interatomic potential has a complicated form, at the time of calculating the forces, one only needs the tabulated values of $\mathcal{F}$, ρ and ϕ to calculate U_{EAM} and $\vec{F_i}$ from Equations 3.4 and 3.2 respectively. The final expression for U_{EAM} bears resemblance to a pair-wise calculation, leading to the EAM potentials being often mistaken to be similar to classical potentials like the LJ model. Owing to the additional calculation of the embedding forces, the EAM potentials are not only more accurate, but are also computationally expensive than the LJ potentials.

3.1.3. Periodic Boundary Conditions and Pair Cutoffs

Simulations are usually carried out in a cubic or cuboid simulation box, which is a virtual space in which the particles exist. A two-dimensional (2D) simulation box is depicted in Figure 3.1. While MD techniques can simulate millions of atoms in today's supercomputers, the number is still quite small in comparison to realistic systems where the particle numbers are in the orders of the Avogadro's number (6.022×10^{23}). For this reason, any edge effects or surface effects observed in simulations will be significantly larger than observed in the experiments.

In order to circumvent this problem, periodic boundary conditions (PBC) are used, instead of closed boundaries. The periodic boundaries are visualised in Figure 3.1.: the simulation box is connected across boundaries such that any atom that exits the simulation box on one side, enters from the opposite side while maintaining the same trajectory[2]. Additionally, by the minimum-image convection [125, 128], for each atom that crosses the boundary in either of the $\hat{i}$, $\hat{j}$ and $\hat{k}$ directions, an "image" flag is assigned to each atom. Forces on a particle are calculated with the nearest images of the other particles. Even with periodic boundary conditions, the number of atoms in the system should be large enough, to avoid any finite-size effects.

In MD simulations, forces acting on every atom need to be calculated, and subsequently the computation times scale as $\mathcal{O}(N^2)$ with the number of particles N in the N-body system. To improve simulation efficiency, short-range interactions between particles are truncated within cut-off distances (See Figure 3.1b). For long-range interactions such as Coloumbic forces, a technique called Ewald summation is used to approximate the long-range forces (forces which decay slower than r^{-3}) as well allowing the simulations to scale as $\mathcal{O}(N^{3/2})$ or $\mathcal{O}(Nlog(N))$ [125, 128].

---

[2]An unacquainted reader can draw parallels from the Pac-Man arcade game, in the way that Pac-Man and the ghosts traverse across the edge of the maze, only to appear on the other side.
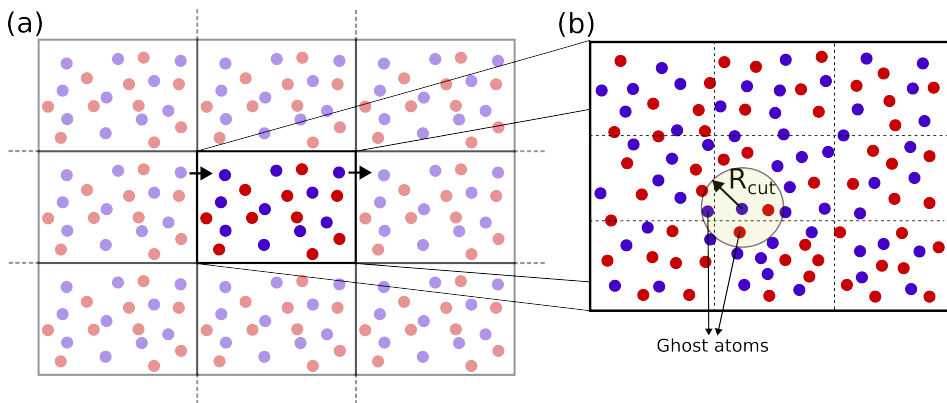
Figure 3.1.: Simulation box and periodic boundary conditions: (a) A simulation box and eight of its infinite images are depicted, atoms moving across the boundary can be mapped back within the original box as well. (b) The atoms in the simulation box are partitioned into grids, which can be assigned to independent processors for parallel computing. Ghost atoms of the central grid, associated with the highlighted central atom are also depicted.

Furthermore, defining a cut-off radius also allows one to divide a simulation box into multiple grids (See Figure 3.1b), which allows for the MD solvers to be run in parallel on multiple processors [123]. Each grid of the simulation box is assigned to a single processor. The atoms within a grid, and associated "ghost" atoms—which are atoms outside the given grid but within the cut-off distances of the atoms inside—exist within the memory of the processor. In this way, the interactions of an N-body simulations can be computed independently within each processor grid.

3.1.4. Time Integrators

In an MD simulations box that was discussed in the previous section, the initial coordinates and even velocities of the particles can be defined. However, to get information on the time evolution of the system, the equations of motion—typically described by the Newtonian formalism—still need to be numerically time-integrated. Based on an algorithm first proposed by Verlet [129], the modified Velocity-Verlet algorithm [130] is the standard

technique to perform time integration in MD [3]. At a given time t, the position of an ith particle $\vec{r}_i$ in the time intervals $t \pm \delta t$ can be expressed as a Taylor expansion:

$$\vec{r}_i(t + \delta t) = \vec{r}_i(t) + \vec{v}_i(t)\delta t + \frac{\vec{F}_i(t)}{2m_i}\delta t^2 + \dddot{\vec{r}}_i(t)\frac{\delta t^3}{3!} + \mathcal{O}(\delta t^4)$$
$$\vec{r}_i(t - \delta t) = \vec{r}_i(t) - \vec{v}_i(t)\delta t + \frac{\vec{F}_i(t)}{2m_i}\delta t^2 - \dddot{\vec{r}}_i(t)\frac{\delta t^3}{3!} + \mathcal{O}(\delta t^4)$$

(3.5)

Where $\vec{F}_i$, $\vec{v}_i$ and m_i are the force, velocity, and mass of the ith particle, respectively. Adding and subtracting the two Equations 3.5, one gets:

$$\vec{r}_i(t + \delta t) + \vec{r}_i(t - \delta t) = 2\left(\vec{r}_i(t) + \frac{\vec{F}_i(t)}{2m_i}\delta t^2 + \mathcal{O}(\delta t^4)\right)$$

(3.6)

$$\vec{r}_i(t + \delta t) - \vec{r}_i(t - \delta t) = 2\left(\vec{v}_i(t)\delta t + \dddot{\vec{r}}_i(t)\frac{\delta t^3}{3!}\right)$$

(3.7)

These two equations, have been approximated to give the following relation:

$$\vec{r}_i(t + \delta t) \approx \vec{r}_i(t) + \vec{v}_i(t)\delta t + \frac{\vec{F}_i(t)}{2m}\delta t^2 + \mathcal{O}(\delta t^3)$$

(3.8)

For a more detailed treatment, the reader is referred to References [125, 128].

Similarly, an expression for velocities is obtained:

$$\vec{v}_i(t + \delta t) = \vec{v}_i(t) + \frac{\vec{a}_i(t) + \vec{a}_i(t + \delta t)}{2}\delta t$$

(3.9)

where $\vec{a}_i$ denotes the acceleration. With the Equations 3.8 and 3.9, the Velocity-Verlet algorithm can finally be described:

- Get initial coordinates
- Calculate new position $\vec{r}_i(t + \delta t)$ using Equation 3.8, and compute forces, or $\vec{a}(t)$
- At t=$\delta t/2$, calculate intermediate velocity

$$\vec{v}_i(t + \delta t/2) = \vec{v}_i(t) + \frac{1}{2}\vec{a}_i\delta t$$

(3.10)

- Using $\vec{r}_i(t + \delta t)$, compute acceleration $\vec{a}_i(t + \delta t)$

---

[3]Some alternatives like r-RESPA, Runge-Kutta methods also exist but are out of the scope of this thesis.

- Calculate new velocity $\vec{v}_i(t + \delta t)$

$$\vec{v}_i(t + \delta) = \vec{v}_i(t + \delta t/2) + \frac{1}{2}\vec{a}_i(t + \delta t)\delta t \tag{3.11}$$

As seen above, the time integration can be started with just the initial coordinates and velocities. Furthermore, the Velocity-Verlet algorithm allows for calculation of forces just once per time step. The error in estimating $\vec{r}_i(t + \delta t)$ is of order $\mathcal{O}(t^3)$. The error dies down exponentially with the time of the simulation, this effect is termed as Lyapunov instability [128]. This error loses significance at long simulation time scales.

The shorter the length of the timestep, the higher the accuracy. However, a longer timestep results in lesser calculations and consequently is less computationally expensive. For this reason, the choice of the timestep is quite important. For MG simulations with the EAM potential, usually a timestep of 1 *fs* is chosen. A good timestep should be at least less than half the timescale of the fastest vibration in the system, by the Nyquist theorem [131].

3.1.5. Thermostats and Barostats

Once a system has been assigned initial coordinates, and velocities, the MD simulation can be run as an isolated system or a microcanonical ensemble. To simulate the system at a specific temperature, or to avoid accumulation of numerical errors over time, temperature control is required, and it is done by implementing thermostat algorithms.

The simplest form of temperature control in MD can be done by harnessing the equipartition theorem. The average kinetic energy ($\langle E_{kin}\rangle$) and temperature (T) are associated by the following relation, for a system with 3 degrees of freedom:

$$\langle E_{kin}\rangle = \frac{1}{2}\langle \sum_i m_i \vec{v}_i^{\,2}\rangle = \frac{3}{2}k_B T \tag{3.12}$$

where m_i and $\vec{v}_i^{\,2}$ are the mass and velocity of the ith particle respectively. Knowing this, temperature control can be achieved by simple scaling of velocities. Multiplying velocities by a certain factor can change the temperature of the system. This, however, only sets the temperature but does not replicate behaviour of a closed system, or a canonical ensemble. In this thesis, a Nosé-Hoover thermostat [132] is implemented to create an isothermal ensemble. The Nosé-Hoover thermostat couples the system with an infinite heat bath, and a fictitious mass (or coupling strength) that indicates how quickly the system's temperature can be set to the target temperature.

Similarly, the pressure of a MD system can also be controlled to then simulate constant or varying pressures. Such an algorithm is referred to as a barostat. The chosen barostat in this thesis is the Parrinello and Rahman [133] implementation, which introduces a time-dependent metric tensor, in addition to introducing volume as a thermodynamic variable. In the LAMMPS code, the barostat can be coupled with the Nosé–Hoover thermostat to approximately simulate an isoenthalpic-isobaric ensemble.

3.2. Characterisation

The previous section describes the fundamentals of the MD techniques. The implementation of MD to simulate the rapidly-quenched (RQ) MGs, nanoglass (NG), and cluster-assembled metallic glass (CAMG), will be discussed in Chapter 4. The novel properties of NGs and CAMGs are then evaluated in Chapters 5 and 6.

In order to aid the development of CAMG simulation protocols, and to unravel the exciting properties of CAMGs, all glasses simulated in this dissertation are characterised based on their structural and energetic features.

3.2.1. Radial Distribution Function

In amorphous materials, which do not possess long-range order (LRO), the radial distribution function (RDF)—or the pair correlation function—is to describe atomic structures. The RDF usually is denoted as g(r), and is defined as the average probablility of finding a neighbouring atom within a spherical shell dr at distance r of a given atom. Mathematically, the number of particles in the shell around an atom can be expressed as:

$$dn(r) = \frac{N}{V}g(r)4\pi r^2 dr \tag{3.13}$$

where, N is the total number of particles, and V is the volume occupied by the system. From the above equation, the expression of g(r) around a central atom is derived:

$$g(r) = \frac{V}{N}\frac{dn(r)}{4\pi r^2 dr} \tag{3.14}$$

In the case of a two-component system where α and β are the two species, the partial radial distribution function (PRDF) of the α species with neighbouring atoms of β species is written as:

$$g_{\alpha\beta}(r) = \frac{V}{N_\alpha}\frac{dn_{\alpha\beta}(r)}{4\pi r^2 dr} \tag{3.15}$$

Integrating the RDF $g(r)$ function within a shell of r_0 gives the coordination number in the shell—which is the number of neighbours inside a coordination sphere. In LAMMPS, the g(r) is calculated as a histogram: by binning pairwise distances of all atoms within an MD pair cutoff value.
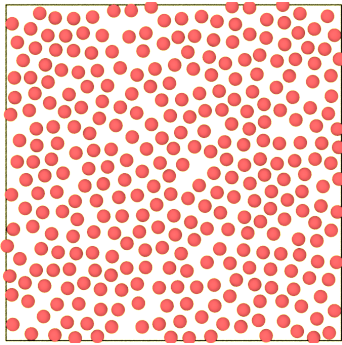
(a)
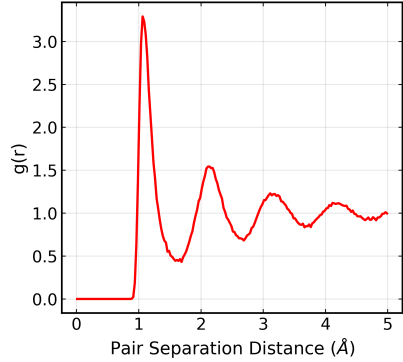
(b)

Figure 3.2.: RDF of a two-dimensional Lennard-Jones melt: (a) A simulation snapshot of a 2D LJ melt using open visualisation tool (OVITO) (b) The RDF of the liquid.

Figure 3.2a visualises a simulated two-dimensional LJ melt with PBC. In Figure 3.2b, the corresponding RDF is displayed. One way to interpret the $g(r)$ is as an indication of the local density. At the length scale of the order of atomic radii, the local density ($\rho(r)$) is a modulated function of average density (ρ_{bulk}).

$$\rho(r) = \rho_{bulk} \cdot g(r) \tag{3.16}$$

Supposing the system simulated in Figure 3.2 was a crystalline material, then RDF would have looked a series of peaks, each nth peak corresponding to the position of the nth nearest neighbour. However, since the structure in Figure 3.2 represents a liquid, and lacking long-range order, the peaks broaden and show the average SRO and MRO. The first peak of g(r) (1.2 LJ distance units in Figure 3.2) is the first nearest-neighbour distance. At large values of r, the probability of finding a nearest neighbor within the shell of radius r is a sure event. Hence, $g(r) \rightarrow 1$ for such large r values, and $\rho(r) \rightarrow \rho_{bulk}$, as seen in Figure 3.2b.

Since the RDF is a projection of the positions of nearest neighbours onto a radius space, it gives the radially averaged information of the bonding. However, it can not provide a full description of the local atomic order.

3.2.2. Voronoi Analysis

The Voronoi tessellation method is used to partition space into mutually exclusive volumes around a finite set of points in space. When applied to metallic glasses, it can assign a finite volume—a polyhedron—to each atom in a simulation. In doing so, one can describe the local order and topology of the simulated amorphous structures. The three dimensional Voronoi polyhedra in the present thesis were determined using the methods described by Brostow et al. [134, 135] and Borodin [136] and implemented on OVITO [137].
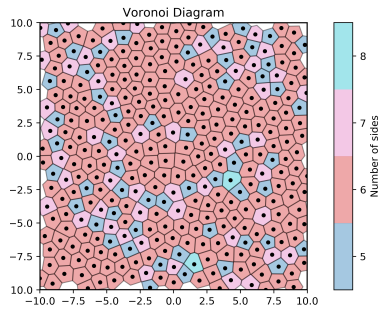
Figure 3.3.: Voronoi tessellation of a two-dimensional Lennard-Jones melt: 2D Voronoi polygons constructed for the 2D LJ melt shown in Figure 3.2a using Python and the *freud* Python library.

The Voronoi polyhedra (VP) are constructed as the shapes that are bound by intersecting planes perpendicular to lines connecting every atom pair. This method is reminiscent of the Wigner-Seitz construction of primitive cells in solid-state physics [64]. The representation of Voronoi tessellation in 2D is shown in Figure 3.3. For 3 dimensional systems, the polyhedra are described by the Schäfli notation [61]: $<n_3\ n_4\ n_5\ n_6>$, where n_i are the number of i-edged faces of the polyhedra [61, 135]. The choices of the polyhedra is not arbitrary, rather they are restricted by two constraints: 1. total number of edges is equal to Z of the central atom. 2. the VP satisfy the relation $\sum_i (6-i)n_i = 0$, known as the Euler relation [138]. The $<n_3\ n_4\ n_5\ n_6>$ Schäfli index is restricted to n_i where $3 \leq i \leq 6$. This restriction originates from the understanding that: 1. the polyhedra cannot have

(a) Nearest neighbours

(b) Coordination polyhedron

(c) Voronoi polyheron
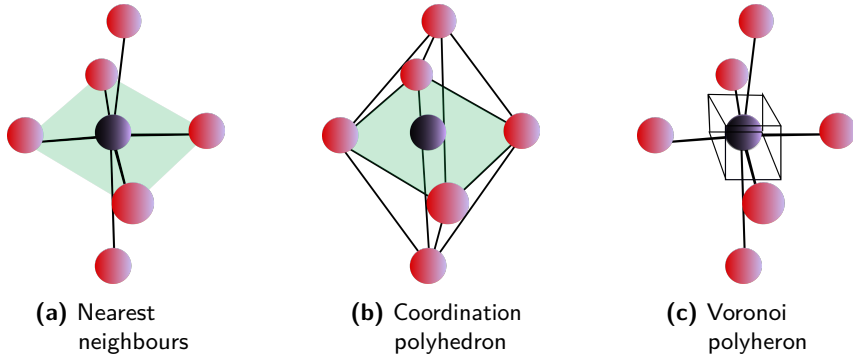
Figure 3.4.: Voronoi polyhedra for a simple cubic coordination: For a (a) simple cubic (SC), the corresponding (b) coordination polyhedra and (c) Voronoi polyhedra are shown. The volumes of the polyhedra and the bonds are not drawn to scale.

faces with less than three edges, and 2. the coordinates with edges of sizes four to six dominate dense packed structures, and faces with larger edges are generally not found [136].

In Figure 3.4a, a simple cubic (SC) coordination is depicted as an example. The central atom is surrounded by six nearest neighbours. Figure 3.4b depicts the corresponding coordination polyhedron. The corresponding VP (Figure 3.4a) is equivalent to the coordination polyhedron, with the total number of faces in a VP being the same as the number of vertices in the coordination polyhedron. The VP has six sides with four faces each, and hence it's Schäfli index would be <0 6 0 0>. The indices add up to six, viz. the coordination number of the central atom.

For metallic glasses in general, the Voronoi polyhedra are known to be classified into four main categories as reported by Yue et al. [78]: 1. icosahedral-like: <0 0 12 0>, <0 0 10 x>, and <0 2 8 x>; 2. crystal-like: <0 4 4 x> and <0 5 2 x>; 3. mixed coordinations: <0 3 6 x>, where $0 \leq x \leq 4$; and 4. other remaining indices.

3.2.3. Surface Mesh

The open surfaces of the simulated samples need to be identified in order to evaluate porosity in NGs and CAMGs, and to compute the volumes enclosed by the CAMGs. In the current dissertation, this is done by means of constructing a surface mesh, by the

alpha-shape algorithm [139] implemented in OVITO. The algorithm utilizes a method similar to Voronoi tessellation called the Delaunay triangulation, that connects every three nearest neighbouring atoms as vertices of a triangle. Then, a "probe sphere" is determined, which defines the smoothness of the surface mesh. The circumcirles of the constructed triangles are compared with the probe sphere. If the radius is smaller than that of the circumcircle, the surface is determined to be closed. If larger, then the surface is considered to be open. The alpha-shape method takes care of the PBC.

3.2.4. Local Atomic Strain

The local shear strain or the von Mises shear strain, has been traditionally used as a model to explain failure theories in metallic materials, and for the visualisation of shear transformations in metallic glasses. One of the aims of this dissertation is to identify the interfaces formed amongst clusters, in which atoms are sheared due to either compaction in NGs, or deposition in CAMGs.

To calculate the local deformations, two system configurations are required: one being the sample to be characterised, and the second being an initial undeformed reference configuration. Using these, the von Mises shear strain is calculated by an algorithm proposed by Shimizu et al. [102]: from the two configurations, a local atomic deformation gradient tensor (or a transformation tensor) is determined, from with the strain tensor is calculated. The invariant of the strain tensor is the von Mises local shear strain, and is given by the following expression:

$$\eta_i^{Mises} = \sqrt{\eta_{yz}^2 + \eta_{xz}^2 + \eta_{xy}^2 + \frac{1}{6}\left[(\eta_{yy} - \eta_{zz})^2 + (\eta_{xx} - \eta_{zz})^2 + (\eta_{xx} - \eta_{yy})^2\right]} \quad (3.17)$$

where, η_i is the strain tensor for each ith atom. The von Mises strain was calculated and visualised using the OVITO software.

3.3. Synopsis

This chapter primarily discusses the fundamental ideas of the MD technique, which were used to simulate the glassy systems in this dissertation. The simulations were run using the LAMMPS code on the Forschungshochleistungsrechner (ForHLR II) and Hochleistungsrechner Karlsruhe (HoreKa) high-performance computing (HPC) clusters available through the Karlsruhe Institute of Technology (KIT). The message passing interface (MPI) protocol using MPICH2 was implemented to perform parallel programming. Furthermore, some characterisation techniques such as RDF, Voronoi tessellation and the von Mises local shear strain—used to evaluate the simulated data sets—were elucidated. The characterisation was done predominantly using Python scripts, and the OVITO Python library.

The iterative workflow for the development of the simulations and the software involved, are described in the Supplementary Material Section, Figure A.1. The simulation codes developed in the framework of this thesis, and the necessary post-processing scripts can be accessed in Section A.2, also in the Supplementary Material chapter. The concepts addressed in this chapter will be implemented in Chapters 5 and 6 to simulate and characterise CAMGs and NGs.

4. Development of Simulations of Cluster-based Metallic Glasses

> *Selected sections of this chapter were communicated in [140]. The respective paragraphs—along with further additions and modifications—are indicated by a vertical gray bar in the inner page margin[1].*

It has been discussed in Chapter 1 that a simulation study of the cluster-assembled metallic glass (CAMG) is critical in understanding their local structure and related properties. The present chapter elucidates the molecular dynamics (MD) models developed within the framework of this thesis to produce simulated data sets of CAMGs.

First, the Rapidly-quenched (RQ) metallic glass (MG) is simulated and characterized, to test the embedded atom model (EAM) potential, and to serve as a reference. The protocols are then extended to study the CAMG and nanoglass (NG).

Next, the simulation of amorphous clusters—the building blocks of the CAMGs—is discussed. The reader will then be introduced to novel simulation protocols, developed to investigate the CAMGs. Further, a simulation protocol for NGs is also discussed. The challenges encountered in modelling the non-trivial deposition process of the CAMG, and solutions on how to overcome these hurdles are presented; thereby allowing one to simulate CAMGs in a computationally efficient manner.

4.1. Simulating Metallic Glasses

The simulated behaviour of Cu-Zr RQ MGs are compared with results from previously known works. The variation of the local packing, final energy states, and volume occupancy in the Cu-Zr glasses are studied as a function of quench rates (10^{10} K/s, 10^{12} K/s, 10^{13} K/s, 10^{14} K/s) and composition ($Cu_{50}Zr_{50}$, $Cu_{64}Zr_{36}$, $Cu_{60}Zr_{40}$).

---

[1] *Reprinted with permission from [140]. ©2022, ELSEVIER LTD.*
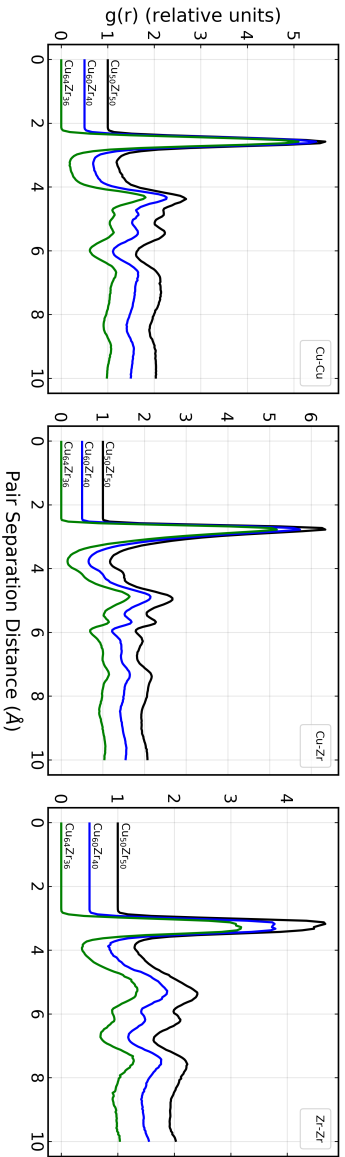
(a) partial radial distribution functions (PRDFs) vs compositions: $Cu_{50}Zr_{50}$, $Cu_{60}Zr_{40}$, and $Cu_{64}Zr_{36}$.
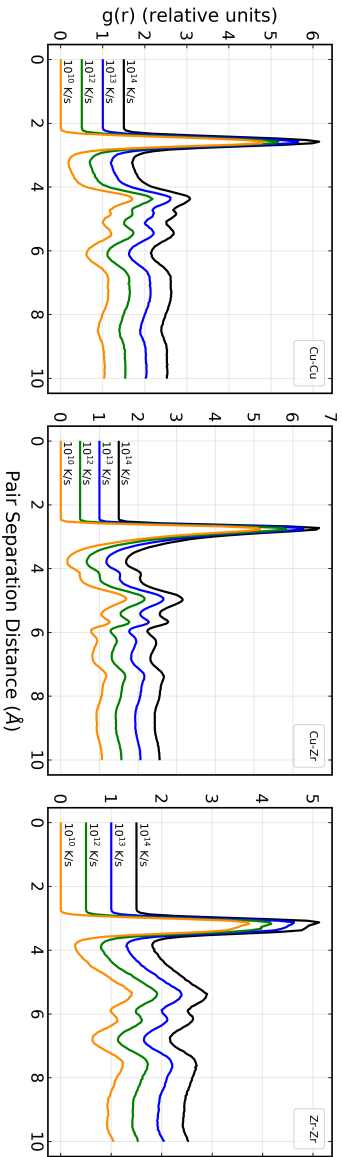
(b) PRDFs vs quench rates: 10^{10} K/s, 10^{12} K/s, 10^{13} K/s and 10^{14} K/s

Figure 4.1.: Partial pair correlations in RQ MGs: Cu-Cu, Cu-Zr, and Zr-Zr pair correlations in the RQ MGs for varying MG-synthesis compositions and quenching rates.

Atomistic MD simulations of binary Cu-Zr glasses have been performed using the large-scale atomic/molecular massively parallel simulator (LAMMPS) code [122, 123]. A semi-empirical potential developed with data from $Cu_{46}Zr_{54}$ alloys [101], based on the EAM model proposed by Daw et al. [126], was used to model the Cu-Zr interactions. The $Cu_{50}Zr_{50}$ MGs were simulated by quenching from the 2000 K (liquid state) to 50 K temperature. The liquid state was simulated by equilibrating an equimolar mixture of Cu and Zr atoms placed at random coordinates at 2000 K for 2 ns. The quenching to the glassy state was performed at zero pressure at four cooling rates of 10^{10} K/s, 10^{12} K/s, 10^{13} K/s and 10^{14} K/s. The system temperature and pressure were controlled by using a Nosé-Hoover thermostat (NPT in LAMMPS). The MGs will be referred to by the quench rate: for instance, an MG quenched at 10^{10} K/s will be referred to as a 10^{10} K/s MG, and so on. For the case of the 10^{10} K/s MG, which requires a much longer and computationally expensive simulation, a sample of ~16,000 atoms was chosen, and replicated in all three dimensions, resulting in a larger sample of ~150,000 atoms in total. For the 10^{12} K/s and 10^{14} K/s MGs, in which the simulation costs are less, the larger samples of ~150,000 atoms were prepared directly. Periodic boundary conditions were used in all three directions, and a time step of 1 *fs* was chosen for all simulations. After quenching, the metallic glasses were equilibrated for 2 ns at 50 K.

4.1.1. Pair-correlations in RQ MGs

The PRDFs were computed from the snapshots of the RQ MGs, with a cutoff radius of 10 Å. The lack of any sharp peaks indicates lack of crystalline order. The first peak positions of Cu-Cu (2.45 Å), Cu-Zr (2.8 Å), and Zr-Zr (3.25 Å) in the MGs match well with those previously reported values [141, 142]. Beyond this information, the PRDFs fail to capture the change in the structure of RQ MGs with cooling rate or with composition.

4.1.2. Local Atomic Short-range Order

The local amorphous short-range order (SRO) of MGs, i.e., the description of the local coordinations exhibited by the atoms were studied via Voronoi tessellation, a process that has been described in Chapter 3, Section 3.2.2. The volumes occupied by atoms upon Voronoi tessellation were shown by Sheng et al. [56] to be analogues of the Frank-Casper polyhedra [72]. These shapes were used to define the local SRO. Moreover, it was observed that certain polyhedra were more prominently occurring. In CuZr glasses, icosahedral atomic coordinations and icosahedral-like (ICO-like) coordinations were found to be the dominating polyhedra, and the most relevant motifs that correlate to glass stability [74, 78]. Other kinds of polyhedra could also possibly exist in the glasses, describing other motifs, such as crystalline packing (should crystalline coordinations be present in the

solids), or the liquid-like packing (which constitute sites for shearing under stresses) [74, 78, 143]. However, these polyhedra are not discussed in detail in this thesis.

Ding et al. [74] mention how the distinction between full-icosahedral (FI) and ICO-like lies in the distortion tolerance set in the polyhedron designation algorithm during the tessellation. For this reason, the quantified FI is quite sensitive for differences in the simulation protocols and potentials used.[77, 94, 144, 145]. This variability also prompts the inclusion of the icosahedral-like order (ILO) in the study of the local amorphous SRO. To standardise the simulation protocols presented in this thesis, Voronoi analysis was performed on these already well studied RQ MGs.

(a)

(b)
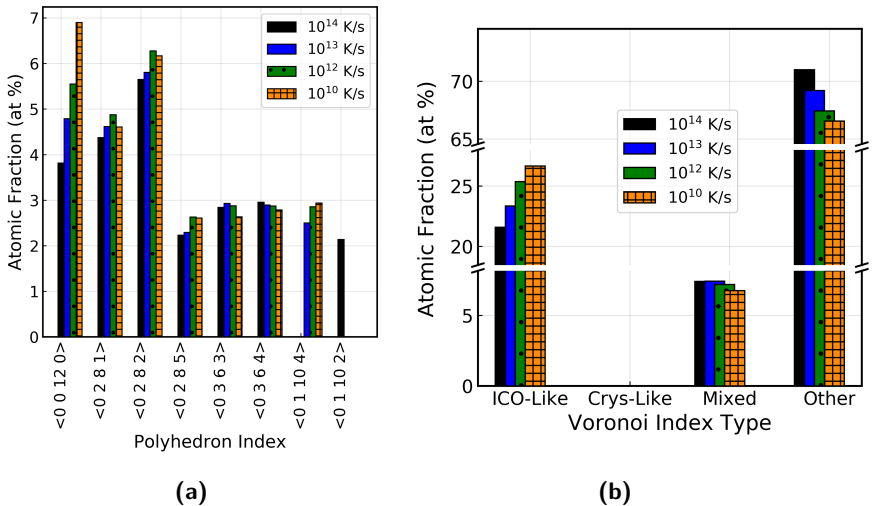
Figure 4.2.: Local short-range order vs. quench rate in RQ MGs: (a) and (b) Show systematic increase in full-icosahedra and icosahedral-like fractions of $Cu_{50}Zr_{50}$ RQ glasses with decrease in cooling rate, from 10^{14} K/s to 10^{10} K/s.

First, the behaviour of the simulated RQ MGs with varying quench rate, but at a fixed composition ($Cu_{50}Zr_{50}$), is verified. Figure 4.2a shows the top seven highest occurring Voronoi indices in $Cu_{50}Zr_{50}$ RQ glasses quenched with cooling rates 10^{10} K/s, 10^{12} K/s, 10^{13} K/s, and 10^{14} K/s. The percentage of atoms exhibiting the <0 0 12 0> index, representing the FI coordinations, is seen to increase with lowering quench rates. In Figure 4.2b, the sorted categories (as described in Section 3.2.2) of Voronoi polyhedra

(VP) are described. Firstly, the lack of any crystalline coordinations indicates that all these RQ MGs have amorphous SRO. While it can be seen that the ICO-like coordinations also increase with decreasing quench rate, concurrently one can also notice the decrease in the "other"-or-miscellaneous coordinations, which are known to be indicators of glass instability (for more details on the four prominent classes of VP, see Section 3.2.2). Decreasing the quenching rate improves the FI and ICO-like fractions. These results are in agreement with previous knowledge [5, 78], that lowering the glass quench rate correlates with increased ICO-like packing and stability.

**(a)**   **(b)**
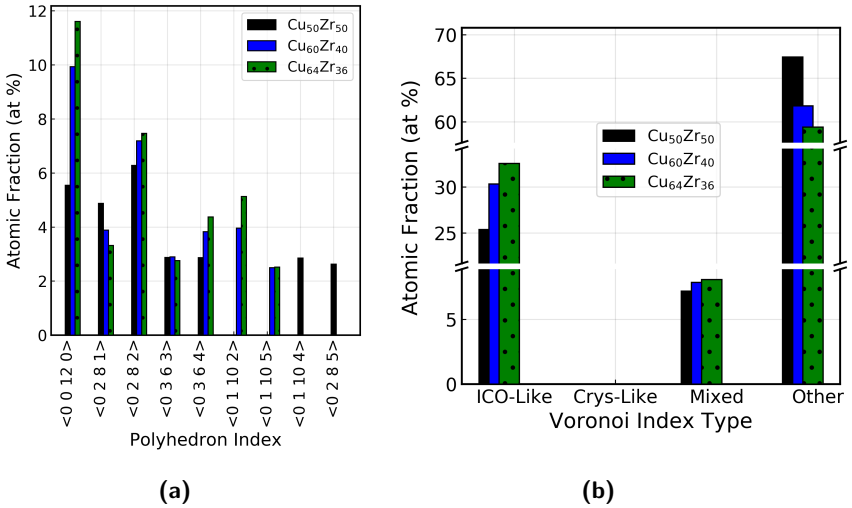
Figure 4.3.: Local short-range order vs. composition in RQ MGs: (a) and (b) show the increase of full-icosahedral ($<0\ 0\ 12\ 0>$) and icosahedral-like fractions with increase in composition from $Cu_{50}Zr_{50}$, to $Cu_{60}Zr_{40}$ to $Cu_{64}Zr_{36}$ for 10^{12} K/s MGs.

Next, the FI and ICO-like fractions in RQ MGs was studied with respect to composition at a fixed quench rate. $Cu_{50}Zr_{50}$, $Cu_{60}Zr_{40}$, and $Cu_{64}Zr_{36}$ glasses made at a quench rate of 10^{12} K/s were studied. From Figure 4.3a-b, two observations can be made. Firstly, with increasing Cu composition in CuZr metallic glasses while keeping the quench rate fixed, the FI and the ILO increase. This observation is consistent with results from previous works [76, 77, 82]. Secondly, a concurrently decrease in the defective coordinations marked as "other" is observed. In CuZr glasses, increase in Cu seems to improve glass-forming ability (GFA).

4.1.3. Potential Energy of MGs

The potential energy (PE) of the simulated RQ MGs were analysed with respect to both the cooling rate and the compositional changes in CuZr RQ MGs. Figure 4.4 shows the normalized PE distributions of the MGs. Two distinct distributions are observed; one for the Cu atoms, and one for the Zr atoms. The Zr atoms are found to occupy lower energies on average compared to the Cu atoms. For the $Cu_{50}Zr_{50}$ 10^{10} K/s MGs, the Cu peak occurs at ∼-3.52 eV/atom and the Zr peak at ∼-6.45 eV/atom. In the inset of the figures, the average PE of each atom; i.e, the area under the graph is represented. In Figure 4.4a, it is noticed that the average PE of the RQ MGs reduces with quench rate, this in alignment with the expected physical behaviour of glasses [5, 78]. The relative peak shifts are not noticeably different from one another. However, no further analysis has been attempted to characterize the nature of these distributions. Yet another trend is observed, in Figure 4.4b, where Cu-Zr RQ MGs of 10^{12} K/s are contrasted with one another: with increasing Cu concentration, the average PE notably increases. This change is correspondingly noticed in the PE/atom distributions: the peak height of Zr drops with composition (and that of Cu increases), owing to the decrease in stoichiometric population of Zr atoms. Furthermore, with the peak centres also being shifted to the right, it is confirmed that both the Cu and Zr atoms, on an average, occupy high energy states in glasses with higher Cu concentration. The relative increase in Cu concentration has a stronger influence in the change of energy states of metallic glasses, than the quench rate.

4.1.4. Atomic Volume Distributions of MGs

Similar to the Sections 4.1.2 and 4.1.3, the RQ MGs are also contrasted with each other in terms of atomic volume, while varying both composition and quench rates. In Figure 4.5, the normalized distributions of atomic volume occupancy are shown; in the inset, the average volume per atom (area under the curve) is described. Like in Figure 4.4, two separate distributions are once again observed for the Cu and Zr atoms. The Cu atoms are seen to occupy a lower volume on average in comparison to Zr atoms, influenced by their respective atomic radii (Cu: 1.35 Å, Zr: 1.55 Å). With increasing Cu composition, the Cu peak height increases, yet it shifts to the left on the x-axis. The opposite trend is observed for Zr atoms. The resulting effect is seen on the average atomic volume which reduces with increase in Cu composition (see Figure 4.5 inset). In the CuZr glasses explored in this section, the glasses have better packing with increasing Cu concentration. This observation is in agreement with a previous study by Peng et al. [76].

Next, the relationship between volume distributions of $Cu_{50}Zr_{50}$ glasses and the quenching rates was investigated. Figure 4.6a shows the volume distributions of the Cu and Zr
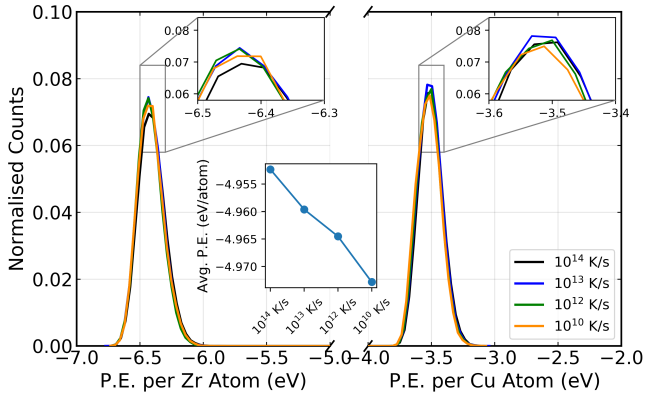
(a) PE vs Quench Rate
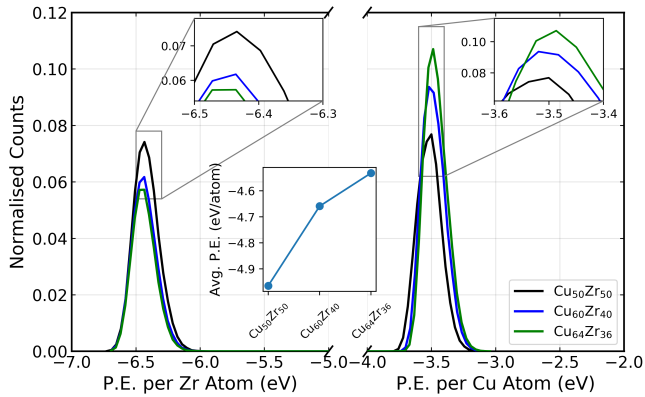
(b) PE vs Composition

Figure 4.4.: Potential energy vs composition and quench rate in RQ MGs: PE per atom distribution for (a) $Cu_{50}Zr_{50}$ MGs with changing quench rates 10^{10} K/s, 10^{12} K/s, and 10^{14} K/s; and (b) 10^{12} K/s RQ metallic glasses of varying composition: $Cu_{50}Zr_{50}$, $Cu_{60}Zr_{40}$ and $Cu_{64}Zr_{36}$. The insets describes the average potential energies of the glasses.
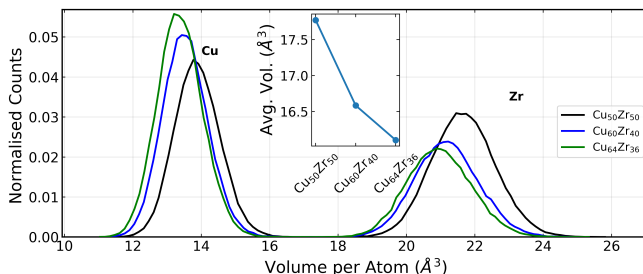
Figure 4.5.: Volume occupancy vs composition in RQ 10^{12} K/s MGs: Volume distribution for 10^{12} K/s metallic glasses of varying composition: $Cu_{50}Zr_{50}$, $Cu_{60}Zr_{40}$ and $Cu_{64}Zr_{36}$. The inset describes the average volume (or volume per atom) for the three glasses.

atoms. The occurrence of the peaks is similar to that in Figure 4.5. In the inset of Figure 4.6a are the calculated values of the average atomic volumes per atom in the RQ MGs. Here, no clear trend is observed. Furthermore, it is noticed that the 10^{10} K/s glass has the highest volume, i.e, the lowest density. These findings are in disagreement with previous knowledge [5, 78].

For this reason, it was important to verify the simulation technique chosen to prepare RQ MGs in Section 4.1. Firstly, in the method used, the total number of atoms in the simulation were not equal for the MGs of varying quench rates. Next, the melt of the binary alloy was obtained by directly setting the temperature of the atoms to 2000 K for 2 ns. It could be suspected that the melting of the metallic glass before the quenching was not simulated well enough. To reveal the influences of these two processing steps, some additional simulations sets were performed for each of the 10^{10} K/s, 10^{12} K/s and 10^{14} K/s MGs: 1. The MGs were simulated with equal number of atoms, 2. an additional melting step was performed before quenching.

In Figure 4.6b1-b3, the volumes were recorded with respect to the temperature, as the quenching process occurred. In the inset, the temperature (T) is also plotted as a function of the simulation timesteps. Figure 4.6b1 depicts MGs that were treated by the same process as in Section 4.1. In Figure 4.6b2, all RQ MGs had the 8192 atoms in the box. Next, in Figure 4.6b3, all RQ MGs had the same number of atoms and additionally a 2 ns melting step was performed. The initial random mixture of atoms were first
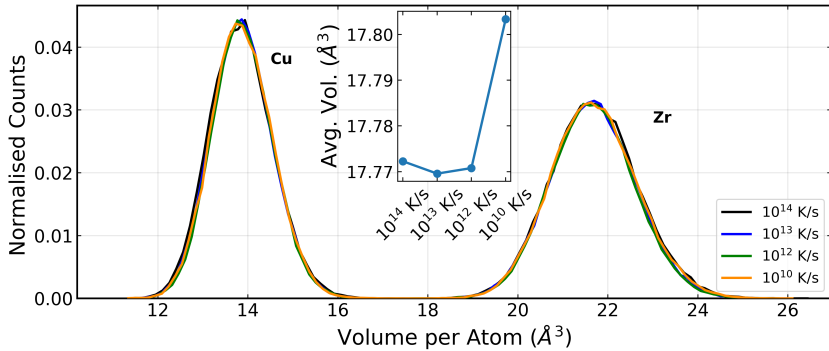
(a) Volume vs Quench Rate
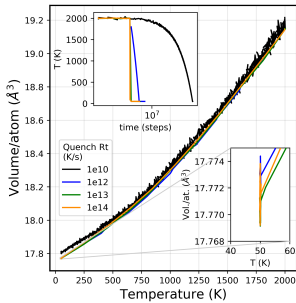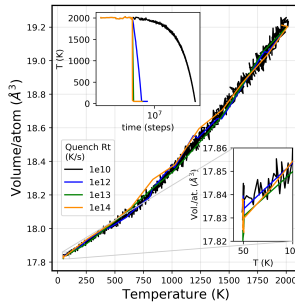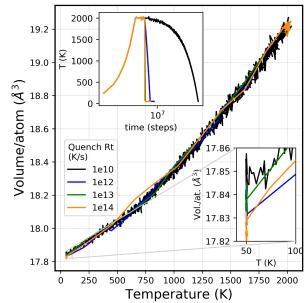
(b1) **(b2)** **(b3)**

(b) Volume vs Temperature: Varying RQ MG Preparation

Figure 4.6.: Volume occupancy vs quench rate in $Cu_{50}Zr_{50}$ RQ MGs:
(a) Volume occupancy in RQ MGs quenched at rates between 10^{10} K/s-10^{14} K/s (b) Volume evolution during quenching (b1) as in Section 4.1 (b2) starting with 8192 atoms at 2000 K (b3) 8192 atoms melted from 50 K before quenching.
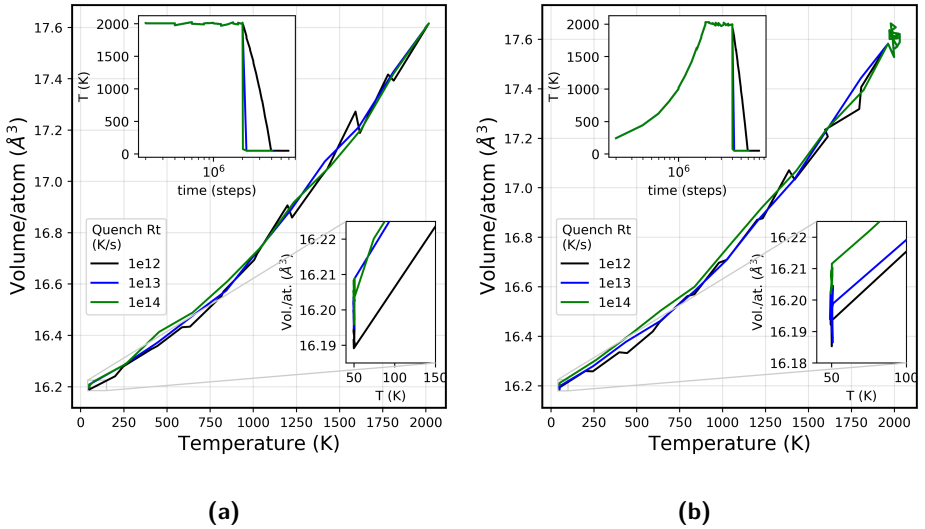
Figure 4.7.: Volume evolution vs quench rate in Cu$_{64}$Zr$_{36}$ RQ MGs:
Volume evolution during cooling of RQ MGs quenched at rates between 10^{12} K/s-10^{14} K/s with (a) 8192 atoms melted directly at 2000 K, and (b) 8192 atoms melted with a temperature ramping from 50 K to 2000 K before quenching.

equilibrated at 50 K, melted at 2000 K, equilibrated for 2 ns, and then quenched. In the three processes, however, the volume behaviour during cooling is not reproduced correctly for the glasses. Moreover, at 50 K, volume fluctuations—significantly higher than a volume change occuring by a temperature increase of 50 K–are seen as indicated in the insets of Figures 4.6b1-b3. Visually, the glass transition is estimated to be around 600 K, however, a more rigorous estimate has not been attempted for these RQ MGs in this section. However, the enthalpy evolution with temperature during cooling for the RQ MGs prepared at varying quench rates, described in Figure A.3 in the Supplementary Material, and also briefly in Chapter 6 follows the expected trends [5, 37].

To cross-verify the observations made from Figure 4.6b, the volume vs temperature behaviour was also studied as a function of quench rates in Cu$_{64}$Zr$_{36}$ RQ MGs, which is close to the Cu$_{64.5}$Zr$_{35.5}$ composition validated by the developers of the Cu-Zr glass potential [101]. Starting with a box of 8192 atoms in the box, the glass quenching was

performed with the atoms equilibrated at an inital temperature of 2000 K (Figure 4.7a), and also in a second case where the atoms were first set to 50 K temperature, melted at 2000 K, and then quenched to 50 K (Figure 4.7b). For both treatments, the volume of the RQ MGs presented lots of fluctuations during cooling. For the case of direct quenching from 2000 K, the expected trend of enhanced packing with lower quench rates is not seen below 75 K. The desired effects were only observed in the $Cu_{64}Zr_{36}$ RQ MGs, which were first melted from 50 K to 2000 K before quenching. In both the cases, however, the final average volumes of the glasses fluctuate significantly at 50 K, in comparison to thermal effects as seen in Figures 4.6b1-b3.

Based on the above simulations, it was inferred that while the influence of compositional changes in the RQ MG volume behaviour is easily observable, the effects of quenching rate on the glass volumes are not well reproduced by the EAM potential used. The effects of alternative but older EAM potentials [79, 100] has not been attempted in this thesis.

4.2. Cluster Synthesis

In the present work, the structure of CAMGs with a specific size of the clusters as a function of impact energy is studied using MD simulations, with the intention of comparing the local atomic structure of CAMGs with that of the MGs prepared by RQ. The atomic structure of the CAMGs will also be compared to an equivalent NG prepared by mechanical compaction of clusters as opposed to cluster deposition.

The clusters in the CIBD experiments [30, 31] were generated via inert-gas condensation (IGC) (see Chapter 2 for more details). In previous works to simulate NGs using a Kob-Anderson model [98], the nanoparticles were prepared using a physical-vapour deposition (PVD) growth process. The first route chosen in this work to synthesize clusters was an algorithm to periodically condense gaseous Cu and Zr atoms in a simulation box. To simulate Cu-Zr PVD cluster-growth with the computationally expensive EAM potentials, the procedure had to be optimized for computational time. Typically, inert gas atoms are included in previous IGC simulations [89, 146], to cool the metallic atoms. The present model did not take this into consideration. Instead, the temperature of the Cu and Zr atoms in both the gaseous phase and in the cluster were controlled using a thermostat (NPT in LAMMPS). To reduce computational time further, regular checks were made during the condensation process to delete atoms straying away from the cluster. The growth rate of the cluster was chosen arbitrarily, and the chemical potential effects were not accounted for. Upon testing, the simulation protocol was found to not be stable. As a workaround to additional modelling and testing of the IGC simulation, an alternative method of deriving clusters from the bulk of a simulated RQ MG was chosen.
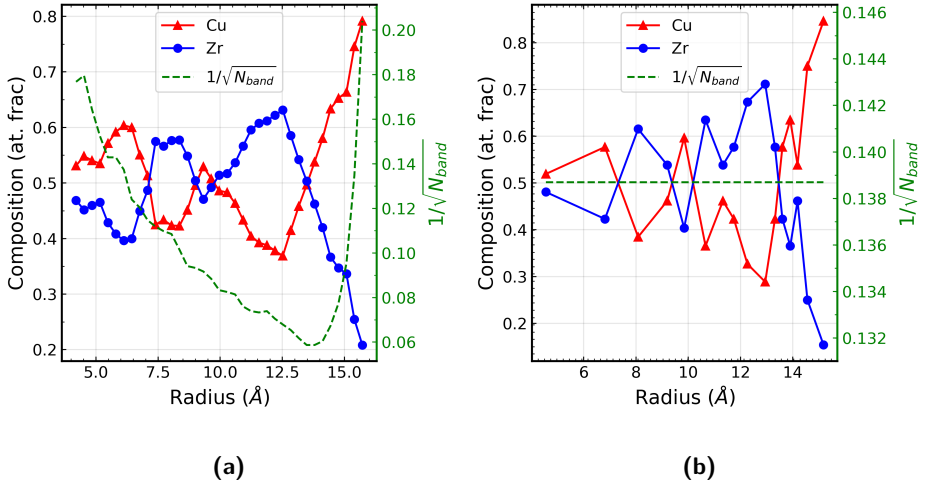
Figure 4.8.: 3 nm $Cu_{50}Zr_{50}$ cluster chemical substructure: A radial compositional analysis with concentric bands chosen with (a) 0.2 nm thickness and (b) fixed population of $\sim$50 atoms, reveals Cu segregation to the surface, which form the basis to define a core-shell structure.

Consequently, in a first step, a free-standing cluster was prepared by cutting a sphere of 3 nm diameter (with 800 atoms) from a 10^{10} K/s $Cu_{50}Zr_{50}$-MG[2] held at 50 K temperature. The resulting cluster was found to be approximately at a $Cu_{50}Zr_{50}$ composition (with a 1% deviation). This compositional deviation is not significant to the following studies on glass SRO, as evident from previous MD studies [76]. As reported earlier by Adjaoud and Albe [22], any cluster develops surface stresses immediately after cutting. It is known that the kinetics of atoms at temperatures above the glass-transition temperature T_g can equilibrate the cluster[22]. Therefore, a short-time increase of the temperature of the cluster, which increases the mobility of the atoms, allows to obtain a configuration similar to a cluster synthesised in a real experiment by IGC. Thus, the protocol developed in reference [22], viz., heating the cluster shortly to 1000 K, i.e., beyond T_g, followed by cooling it back to 50 K, was employed. Both the heating and cooling were performed

---

[2]The 10^{10} K/s quench rate is the conventional value used in literature [20, 22, 23]. Apart from Sections 4.1, 5.7, and A.3, the all the simulated glassy systems in this dissertation are made from 10^{10} K/s RQ MGs.
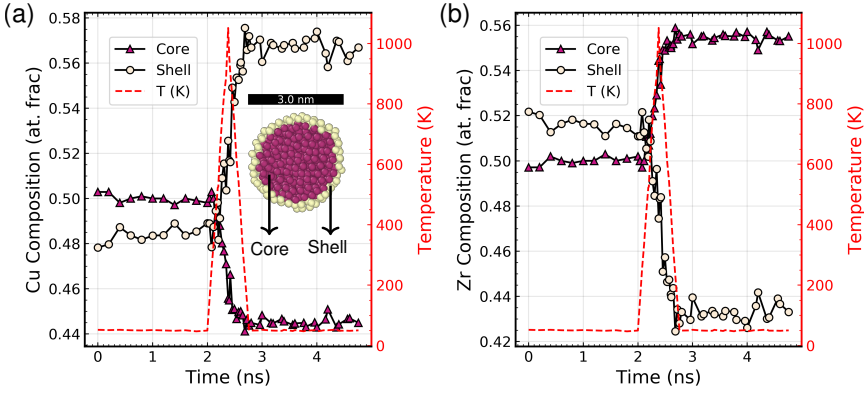
Figure 4.9.: 3 nm $Cu_{50}Zr_{50}$ cluster core-shell composition evolution:
Copper atoms diffusing out of a 13 Å shell (the core-shell structure
is depicted in the inset) of 2Å thickness. The Cu composition
decreases in the core and correspondingly increases in the shell,
as the cluster is heated up to and beyond T_g.

at a rate of 2.5×10^{12} K/s. Although T_g is crossed in the simulation, crystallisation is
avoided (see Section 5.3) due to the short heating time; sufficient diffusion occurs over
the short distances to establish a concentration profile in the cluster. In addition, the
cluster was equilibrated for 2 ns both after the cutting and after the heat treatment. The
heat treatment on the cluster and its effect on the structure of the cluster is visualised in
Figures 4.8 and 4.9 for a cluster derived from the 10^{10} K/s MG, and are discussed below.

It was reported in earlier experiments of small CuZr clusters, of 20-30 atoms in size, that
the Cu atoms segregated to the surface [29]. This chemical segregation, also observed in
granular matter and dubbed the "Brazil-nut" effect [147], influences the local chemical
homogeneity in the length scales comparable to the 3 nm cluster in the simulations. This
surface segregation is promoted by the different surface energies of the pure Cu and Zr
atoms [22, 87]. To verify the radial variation of the chemical segregation in the cluster,
the Cu and Zr compositions in 0.2 nm thick bands at various radii within the simulated
spherical cluster are plotted as a function of the said radii in Figure 4.8a.

The inverse of the square root of the total population $1/\sqrt{N_{band}}$ is also depicted to
estimate the error. At lower radii (≤ 8 Å) the population in the band is low, and the error
is high. In the intermediate radii ranges of 8 Å$\leq r \leq 13$ Å, the Cu and Zr compositions

fluctuate around 50 at. %. From 13-15 Å, Cu and Zr compositions are seen to increase and decrease with increasing band radius. This is indicative of the Cu segregation. Beyond 15 Å, the bands extend outside the volume of the shell, capture only a few of the outer atoms of the cluster, which happen to be predominantly Cu as well. For this reason, the error estimate $1/\sqrt{N_{band}}$ increases for $r \geq 15$ Å. This behaviour seen in Figure 4.8a was also replicated in Figure 4.8b, where the bands were chosen to be equi-populated with ~50 atoms, instead of having the same band thickness. In this case, the error estimate remains constant. Nevertheless, the presence of a chemical segregation is observed.

In Figure 4.9 the evolution of the Cu composition in the 0.2 nm thick shell at a radius of 1.3 nm is shown. Up to a time t = 2 ns, when the cluster is equilibrated at 50 K, the Cu composition remains constant. The heating and cooling spike of the cluster between t = 2 ns and t=~3 ns results in a sharp increase of the Cu-concentration in the outer shell compared to the bulk composition, eventually leveling off at about 56.48 at. %. In the remaining core volume, the Cu concentration decreases to 44.59 at. %. While the overall composition of the 3 nm cluster remains unchanged, two distinct regions are seen in the equilibrated cluster—a core region with a lower Cu concentration, and a shell region with a substantially higher Cu concentration. The inset in Figure 4.9a depicts the core (coloured magenta) and shell (coloured yellow) regions of the cluster. As in other reports, Cu-atoms segregate towards the cluster surface—increasing the Cu concentration by 9 at. % as compared to the initial homogeneous composition. In Figure 4.9b, the Zr-concentration in the core and shell are plotted as a function of time. A drop in the Zr-concentration in the shell is seen, which is concurrent with the Cu-enrichment. The Cu-atoms are enriched in the shell, while the Zr-atoms are enriched in the core. This elemental segregation was also confirmed by subjecting the cluster multiple heat-spikes (see Figure A.4 in Supplementary Material). 100 additional heat-spikes were given to the $Cu_{50}Zr_{50}$ cluster, and Cu-enrichment in the shell was evaluated over the course of the heat-treatments. In contrast to the average Cu-concentration of 57% in the first initial heat-treatment, the Cu concentration oscillated around 59% through the subsequent 100 heat-spikes. Even with additional heat-treatment, the average increase is only 2%, compared to an initial increase of 7%. This compositional variation on the length scale of the cluster size is carried over to the interfacial regions between clusters upon compaction or energetic impact. From previous studies it is known that such chemical heterogeneities in compacted NGs on the nanometre length scale stabilise the amorphous structure [22].

Apart from heating the cluster shortly above the T_g, it was attempted within this doctoral work to find an equilibrium cluster structure using Monte Carlo (MC) techniques on LAMMPS, to perform MC swaps with the Metropolis criterion. However for the 3 nm cluster which is ~800 atoms in size, the MC simulation did not converge. Another alternative is to perform MC using the `vcsgc` package on LAMMPS, which is specifically designed for atomistic precipitation in alloys [148]. However, this package is unfortunately

optimised for multi-million atom simulations and maybe useful to simulate chemical segregation in large nanoparticles.

4.3. Modelling Cluster-assembled Metallic Glasses

4.3.1. Single Cluster Deposition

With the cluster prepared, the next course of study towards understanding CAMGs is the simulation of deposition of single clusters on a surface, as depicted in Figure 4.10a. These simulation conditions were performed to represent closely the experimental conditions in the cluster-ion beam deposition (CIBD) experiments, in terms of cluster size and range of impact energies [30, 31]. In the CIBD experiments, CuZr clusters are generated as charged cluster-ions and then guided as a particle-beam towards the substrate using an electric field. The strength of the said electric field determines the impact energy of the cluster ions onto the substrate. In the present simulation, a classical momentum was given to the cluster to mimic the cluster-acceleration in the experiments, when they pass through the electric field. Furthermore, in the experimental CIBD set-up, the substrate is electrically grounded to prevent any charge build-up on the surface [117]. Therefore, the deposition process can be modelled with classical molecular dynamics without taking electrodynamics into account.

In terms of the thermodynamics, the cluster is modelled as a closed system (micro-canonical ensemble). A simplification, which was made in the MD simulations, is the replacement of the oxidised Si-substrate used in the experiments [30, 31] with an amorphous $Cu_{50}Zr_{50}$ substrate, equilibrated for 2 ns. The cross-section of Figure 4.10a, illustrated in Figure 4.10b, shows a layered thermal model with the following configuration used to represent the substrate: 1. the top layer (modelled as a micro-canonical ensemble) serving as a buffer between the clusters and the substrate, 2. the middle layer being coupled with a heat sink, using a Nosé-Hoover thermostat to hold the substrate temperature at 50 K, and 3. the bottom layer, with atoms held fixed to mimic the rigidity of the substrate. The buffer and thermostatted layers had a minimum thickness of two-atom layers.

It is important to note that all three layers are essential to model the substrate. Without the first layer, the deposited atoms would immediately quench onto the substrate. The second layer accounts for temperature control, the lack of which would have led to a thermally unstable (explosive) substrate caused by its inability to expel sufficient amounts of energy from the system. Furthermore, without the third layer, the substrate would have no mechanical rigidity, and the clusters will simply pass through the substrate at higher energies. The layer model was configured in accordance with previous MD thin film studies [113, 114, 149]. For the case of single cluster deposition, a semi-hemispherical
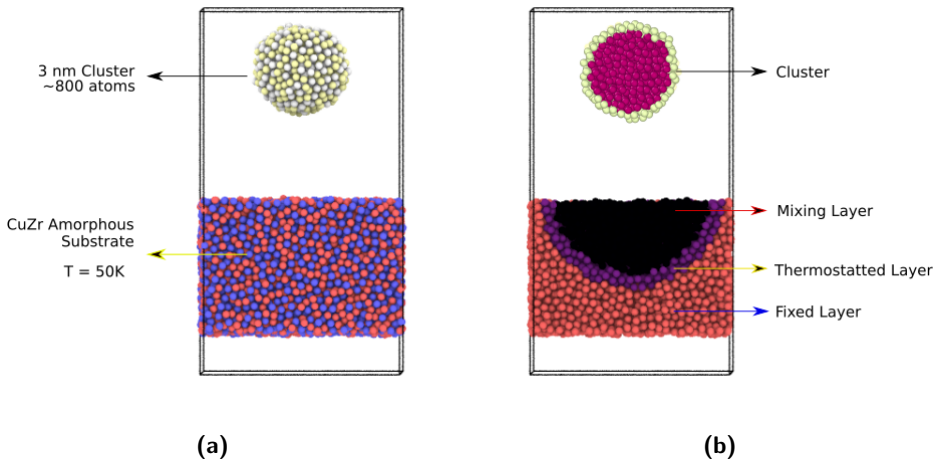
Figure 4.10.: Substrate model for deposition of a 3 nm cluster: (a) The cluster is deposited onto a substrate, with a given energy. (b) The cross-sectional view of the film is as shown, with a mixing/buffer layer and thermostatted layer. The third fixed layer gives rigidity to the substrate.

layout was utilised for the thermostatted layer to account for a spherical shockwave that passes through the substrate. For these single cluster depositions, the substrate length and width were chosen to be 6 nm: two times as wide as the cluster diameter.

The thickness of the first two layers (buffer and thermostatted layers) can affect the heat absorption and also the hardness of the substrate. Consequently, the dissipation of the energy introduced to the film-substrate system by the cluster deposition is influenced by the specific design of the layers. For the present substrate model, the deposition of a single cluster was inspected at large timescales. Figure 4.11 shows the evolution of asphericity of the single cluster upon deposition. The asphericity of the cluster is defined as the ratio of the radii of the cluster in the deposition direction (R_Z in Z-axis) to that the deposition plane (R_{XY} in the XY plane). The undeposited cluster, which is spherical, intially has a $R_Z/R_{XY} = 1$, and as the cluster deforms monotonically with the impact energy, the R_Z/R_{XY} decreases further. After deposition, the R_Z/R_{XY} demonstrates a dip, and eventually the simulation converges, as seen at even 2 ns after the cluster deposition.
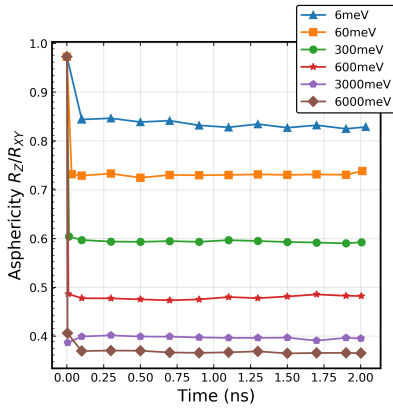
Figure 4.11.: Convergence of single cluster deposition simulation: The asphericity of the cluster for depositions at various per-atom energies serves as a metric to evaluate that 2 ns after deposition, a single deposited cluster deforms no further (See text for more details)

4.3.2. Multiple Cluster Deposition

Following the simulations of deposition of single clusters, the deposition of multiple clusters to form CAMG films was modelled. A large $Cu_{50}Zr_{50}$ substrate of dimensions 25 nm × 25 nm × 3 nm, consisting of about ∼75,000 atoms was chosen. As described in the previous section, the substrate model is tri-layered with flat substrate layers (see Figure 4.12). Both the buffer and thermostatted-layer are set to an initial temperature of 50 K. In the CAMG experiment [30], the clusters are polydisperse in nature, with a log-normal size distribution, while in the present simulations, however, each cluster is chosen to be of the same size. In addition, each cluster is allowed to rotate by three random Euler angles before deposition to ensure a random configuration in the CAMG film samples. The simulation was performed with periodic boundary conditions in the XY plane.

In the CIBD experiments, the electric field, which finally directs the beam of clusters onto the substrate is swept across the substrate surface to ensure uniform particle coverage. To replicate the experimental conditions, however, it was first attempted to sequentially deposit clusters at random locations on the substrate. First, the deposition of a single cluster onto the substrate at 60 meV/atom was studied. As seen in Figure 4.13, the
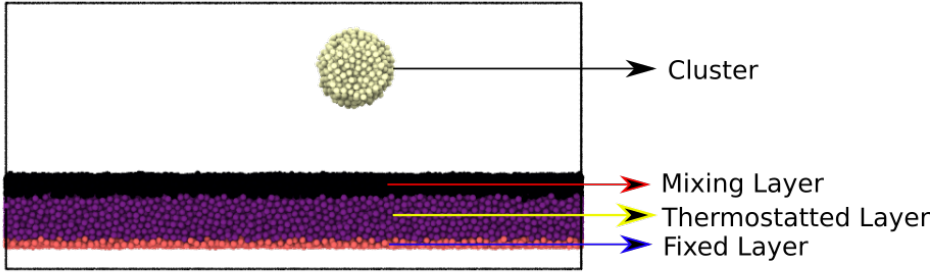

Figure 4.12.: Substrate thermal model for multiple cluster deposition:
Similar to Figure 4.10, this figure shows the substrate model for
the multiple cluster deposition. The substrate is divided into
three layers, in this thermal model.

simulation was found to converge, when inspecting the average PE 2 ns after the deposition.
Hence, 2 ns is determined as the relaxation time between each sequential deposition.

Such a simulation of clusters being sequentially deposited turned out to be computationally
expensive, costing ∼30,000 CPU hours to deposit a layer of 50 clusters. Hence, an
algorithm was developed to shorten simulation times. The schematic of the deposition
algorithm is illustrated in Figure 4.14 and it is described in the following steps:

1. A neighbourhood of a cluster is defined as the region enclosed within two-cluster-
   diameter-lengths.
2. Once a cluster is deposited, its neighbourhood is noted.
3. If a cluster has not been equilibrated for at least 2 ns, no depositions are allowed in
   its neighbourhood.
4. If no deposit-able region exist on the substrate, then the already deposited film is
   equilibrated for 2 ns, and the next cluster is allowed to land.

As seen in Figure 4.14, if the substrate is divided into chunks of a cluster-diameter
length, it results in an 8×8 grid i.e. 64 $ar.u.$. Then, the undepositable area around an
unequilibrated cluster is 9 (3×3) $ar.u.$. When the first cluster is deposited, the probability
of the deposition algorithm finding a depositable-area is high (p=55/64). This probability
value gradually decreases as new clusters randomly land across the substrate plane.
Neverthless, the algorithm reduces the number of equilibration steps, and consequently
the simulation time. Further, this method scales inversely with larger substrates, as
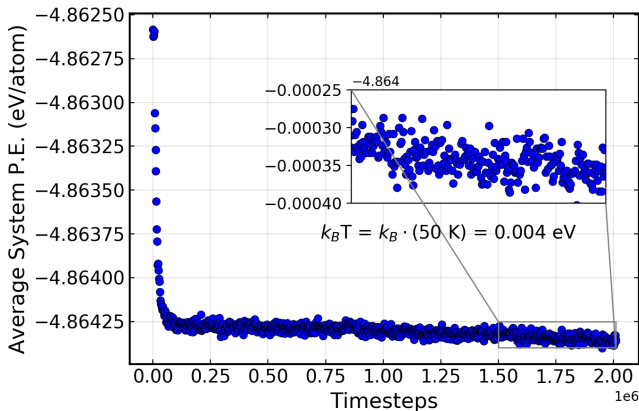
Figure 4.13.: Convergence of deposition on the 25 nm × 25 nm substrate:
The PE of the cluster stabilises with time and converges to its
minimum value, the single cluster after deposition was found to
relax after 2 million timesteps (2 ns) of equilibration.

the probability of a cluster landing in the neighbourhood of an unequilibrated cluster is
greatly reduced.

Such a deposition of the clusters on the substrate at random locations in the XY plane,
is visualised in Figure 4.15. The random deposition of clusters, resulted in the formation
of pillars, thus shadowing certain regions of the film and leading to porous films. The
growth of the porous film bore resemblance to previous statistical studies on ballistic
deposition [150]. Although such pores may occur in the experiments, here a model was
used to maximise inter-cluster interactions and to avoid formation of pores. An absence
of surface effects from the pore formation and an increase of cluster-cluster interfaces
is desirable to study the effects of interfaces in CAMGs. In order to achieve reducing
the porosity, the clusters were deposited in a hexagonal close-packed (HCP) arrangement
onto the substrate.

Figure 4.16a shows the schematic of the algorithm employed to make the HCP depositions.
The HCP patterned film is first considered to be made up of one layer of clusters on the
XZ plane. This layer is divided into four sublayers as depicted in Figure 4.16a: the red
and pink clusters of types 1 and 2 each. Then the following algorithm is implemented:
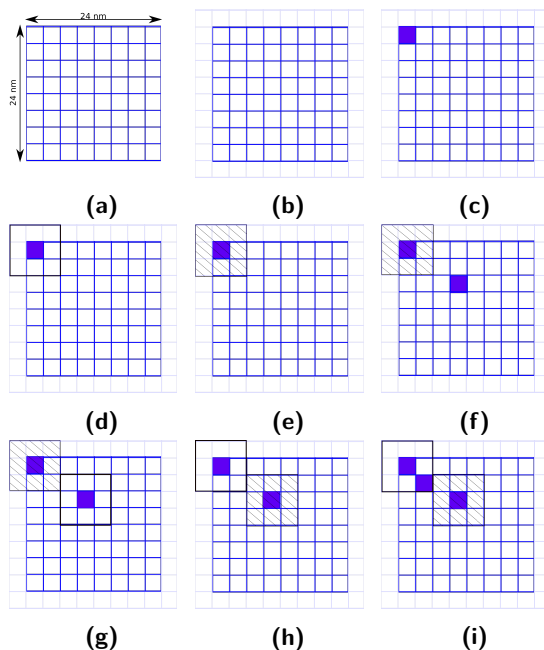
Figure 4.14.: Schematic of the algorithm for random deposition of clusters: (a) Substrate depicted as 64 $ar.u.$ grids with periodic boundary conditions (PBC) (b). An unequilibrated cluster (c) and its neighbourhood (d) block an area (e) of 9 $ar.u.$, resulting in a deposition in a random position (f). The new neighbourhood (g) and blocked area (h) are shown. When the cluster is equilibrated on the substrate, a new cluster (i) can be deposited in its neighbourhood.

1. Deposit Red clusters of type 1. Equilibrate for 2 ns.
2. Deposit Red clusters of type 2. Equilibrate for 2 ns.
3. Repeat steps 1-4 for the Pink clusters

This sequential deposition of clusters by the order of the sublayer they belong to ensures that the newly deposited clusters are not in the neighbourhood of unequilibrated clusters. The algorithm allows for a nearly simultaneous deposition, the only latency between each deposition being the time taken for the cluster to reach the surface of the film. On the
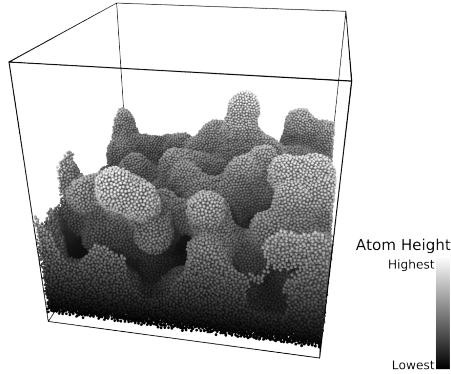
Figure 4.15.: Pores in randomly deposited cluster films: Multiple cluster deposition with the random deposition algorithm results in porous CAMG films.

(a)

(b)
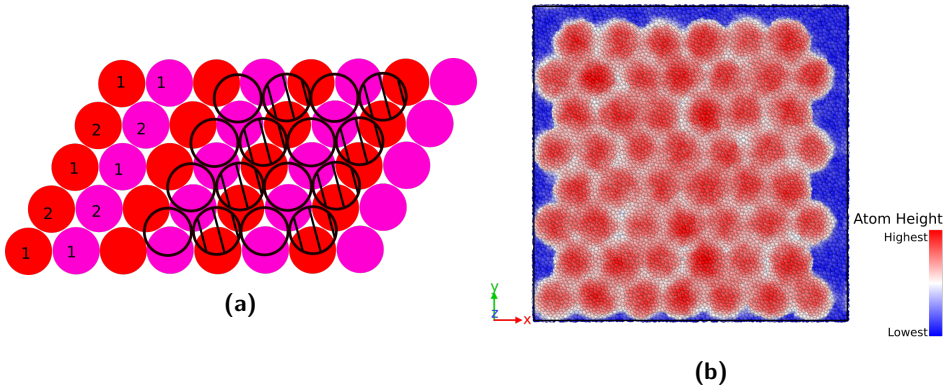
Figure 4.16.: Patterned deposition of multiple clusters: (a) HCP deposition algorithm; the red (1 & 2) and pink (1 & 2) atoms are deposited separately. The clear and striped circles represent the clusters in the next layer. (b) Top view of one layer of deposited film atoms in the HCP pattern, coloured coded by their height in Z-axis

24 nm × 24 nm XY plane of the substrate, 52 clusters can be arranged in an HCP pattern, meaning that the deposition of the four sublayers can be done with four equilibration steps, instead of a 52 times as would be the case in a completely sequential deposition. This speeds up the deposition compared to single deposition algorithm process by a factor of 13 for the given substrate and cluster combination. Like the random deposition algorithm, this algorithm also scales better with the increase in XY dimensions of the film. A top view of a HCP patterned deposition of 3 nm sized clusters at 60 meV/atom energy can be seen in Supplementary Video V1.

4.4. Modelling Nanoglasses

One of the aims of this study is to compare CAMGs to metallic glasses prepared by mechanical compaction, i.e., NGs. The results of simulations of CAMGs and NGs using the same clusters as building blocks allows a comparison of the different processing techniques, compaction for NGs and energetic impact for CAMGs. Furthermore, the structure of simulated NGs prepared by compaction of clusters in the size range of 800 atoms has not been reported in the literature. For the simulation of the cold compaction, the clusters were inserted in a simulation box and compacted at 50 K temperature under 5 GPa pressure to yield a NG of ∼300,000 atoms. In previous works, the compaction of NGs was modelled by inserting the clusters at random positions before compaction [20, 92] as this method closely resembles the actual experiments conducted to obtain NGs. The properties of such NGs are described in further detail, in Chapter 6.

However, when comparing the NGs with CAMGs, the clusters were inserted in a HCP arrangement prior to compaction in order to resemble the arrangement used for the CAMGs. Such a regular cluster arrangement to make NGs has been employed in previous works as well [19, 21, 93, 97]. Once the sample was compacted at 50 K temperature and equilibrated, it was unloaded for 0.2 ns and then equilibrated again for another 2 ns. In the NGs with clusters of sizes 3 nm (described in Chapter 5) and 7 nm (described in Chapter 6) prepared in this way, no pores were present, when examined using a surface mesh with a probe sphere radius of 3 Å [137, 139].

4.5. Summary

The current chapter laid out the details of protocols implemented to simulate the various kinds of metallic glasses discussed in this dissertation. The simulation of CAMGs and NGs were performed using a MD EAM potential. The authenticity of the atomic potential and the modelling methods were tested by simulating RQ MGs. The EAM potential effectively captures the vitrification of the quenched glasses, as evidenced by the PRDFs. It was also possible to reproduce the known theories for the local atomic SRO and PE states for the MGs. Additionally, it was determined that the dependence of glass volume on quench rate is not accurately reproduced using the potential.

Consequently, models used to prepare CAMGs and NGs were developed. First a cluster was simulated cutting out a spherical volume from an RQ MG. With a short heat-treatment above T_g, it was possible to induce Cu-atoms to segregate out to the cluster surface—an effect that better replicates the experiments, and desirable to create stable cluster-cluster interfaces created during deposition (for CAMGs) or compaction (for NGs).

To understand the mechanisms of CAMGs synthesis, the deposition of a single cluster onto a substrate is modelled, and the simulation is determined to have converged upon inspecting the atomic trajectories 2 ns after the deposition. To generate an entire film of clusters, one requires a deposition of multiple clusters onto the substrate. Depositing the clusters in a random fashion resulted in formation of porous films: leading to the reduction of number of cluster-cluster interfaces. This reduction of interfaces is undesirable as it is intended to closely examine the nature of the interfaces in the CAMGs. For this reason, an optimal HCP patterned multi-cluster parallel deposition algorithm was developed to maximise cluster-packing and removal of pores, increase cluster-cluster interfaces, and also leading to a $13\times$ improvement in simulation speed.

Two methods of simulating NGs were discussed. The compaction of clusters was done upon: 1. clusters being randomly inserted in a box—in the manner described by Adjaoud and Albe [20] for NG simulations, and 2. clusters being arranged in an HCP pattern to emulate the pattern formed by the CAMGs deposited in the HCP layout.

The LAMMPS-based simulation codes and workflows can be accessed with information available in Section A.2. Armed with this arsenal of simulation techniques, it is then possible to study the CAMGs and NGs, which motivates the work discussed in the following Chapters 5 and 6.

5. Structure and Packing of Cluster-assembled Metallic Glasses

Selected sections of this chapter were communicated in [140]. The respective paragraphs—along with further additions and modifications—are indicated by a vertical gray bar in the inner page margin[1].

One of the primary objectives of the thesis has been to computationally study the cluster-assembled metallic glass (CAMG)—which are metallic glasses synthesised by an alternative route. The novel cluster-ion beam deposition (CIBD) method holds promise of creating distinct nanostructures in amorphous materials, and controlling the local amorphous order. The simulations of CAMGs are finally possible due to protocols established in Chapter 4. Some primary characteristics of the deposition process were also gathered. In the current chapter, we dive deeper into analysing the simulated CAMGs. First, the deposition of a single cluster on a substrate is studied to understand the behaviour of cluster depositions. Next, the nanostructure and the local amorphous order of the film made from deposition of a plethora of clusters is understood: the simulated CAMGs are characterised by their radial distribution function (RDF)s, short-to-medium range order, their atomic packing, and the energetic states they occupy. By the above metrics, the CAMGs are also contrasted with the rapidly-quenched (RQ) metallic glass (MG) that they are derived from, also the nanoglass (NG). Thereby, one can isolate the effects of cluster deposition and cluster compaction processes[2].

Furthermore, it is explored whether or not the initial state of the cluster has any influence on the final states of the CAMGs (and also NGs). The clusters are derived from RQ MGs of varying quench rates, and CAMGs and NGs are produced from them. Consequently, an attempt is made to understand the resulting structural and energetical changes in the CAMGs and NGs.

---

[1] *Reprinted with permission from [140]. ©2022, Elsevier Ltd.*

[2] It is noted once again that in this thesis, the NGs are made with a monodisperse cluster distribution. They serve as a better counterpart to CAMGs, unlike previous polydisperse-cluster models of NG [20].

5.1. Exploring Deposition Energy Ranges

In order to understand the role of the impact energy on the cluster deposition and to identify the range of impact energy of interest for the preparation of CAMGs, the deposition of a single cluster on a substrate was studied initially. A single $Cu_{50}Zr_{50}$ cluster, 3 nm in diameter— prepared from a 10^{10} K/s RQ MG as described in Section 4.2—was deposited at various energies ranging from 6 meV to 6000 meV per atom.

Figure 5.1 shows the cross-sections of the clusters deposited at various energies in the YZ plane parallel to the deposition axis. The snapshots were made 2 ns after deposition. As seen in Section 4.3, the simulation was determined to have converged by this time. The atoms coloured in yellow and magenta, belong to the shell and core atoms of the cluster prior to deposition, respectively (as in Figure 4.8). No distinction is made in this colour code for the constituent elements. All substrate atoms are coloured in black. Clearly, it is seen that the morphology of the cluster after impact varies with deposition energy.

In the energy range of 6-60 meV/atom, the cluster is in a soft-landing state. In this regime, it is observed that even for the lowest deposition energy of 6 meV/atom the cluster loses the original shape of the free cluster, which was almost perfectly spherical. This change of shape is attributed to a partial wetting due to the cohesive forces at the surface between the cluster and the substrate. No noticeable difference in the final shapes is observed for the cases of 6 meV/atom and 60 meV/atom impact energy. As more drastic changes of the cluster shape are observed at higher impact energies, the deposition energy of 60 meV/atom was chosen to be the upper limit for the soft-landed state.

For all simulated cluster impacts, it is observed in Figure 5.1 that the impact energy clearly influences the final states of the shell atoms in the clusters. The change in state of the deposited clusters was quantified by means of the root mean square deviation of the radial coordinate (with respect to centroid of the cluster) of the shell atoms from the average shell radius and the largest R_C^{max} of the cluster in the deposition axis. The R_C^{max} is calculated as the largest Z-component of the displacement vector subtended by shell atoms in a spherical sector around the deposition axis, to the surface level of the substrate. The method of evaluation R_C^{max} is illustrated in Figure 5.2. The R_C^{max} represents the convexity of the aspherical cluster for the which RC varies as a function of the surface.

Figure 5.1b summarises the $RMSD_{shell}$ and R_C^{max} as a function of deposition energy, with the clusters being equilibrated for 2 ns after deposition. The values of $RMSD_{shell}$ quantify the degree of distortion of the shell atoms from their original positions, which increases monotonically with the impact energy. The shell region stays intact at energies below
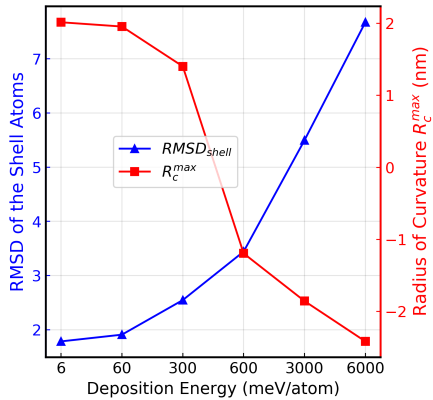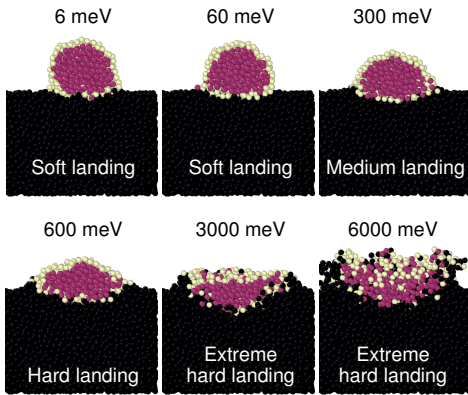
Figure 5.1.: Single 3 nm cluster deposited states: In (a), the cross sections of snapshots of the clusters 2 ns after the simulated deposition at various per-atom energies ranging from 6 meV/atom to 6000 meV/atom are shown, with categories of soft, medium, hard and extreme hard landing indicated. The core and shell atoms are marked in magenta and yellow colours, respectively. This is the same colour scheme used in Figure 4.8. In (b) the as-deposited states of the clusters (curvature and thickness of the embedded clusters) are represented after equilibration for 2 ns after the deposition.

600 meV/atom. However, for impact energies $\geq$ 600 meV/atom, i.e., in the hard-landed state, the distortion of the cluster increases continuously with increasing impact energy. The deposition at 300 meV/atom energy is then defined as the medium-landed state.

The separation between soft, medium and hard landing is assigned arbitrarily. However, these distinctions allow us to understand the broad energy regimes in which the CAMGs retain or lose the signatures of the originally free clusters. In the soft-landed state, the clusters in the CAMGs can be expected to remain mostly spherical. At the higher energies, in the medium-landed state, the cluster is expected to deform further. In the hard-landing state, not only will the cluster be deformed, but the inter-diffusion of the core-shell atoms in the cluster becomes significant.

In line with the changes of $RMSD_{shell}$, the R_C^{max} gradually decreases with increasing energy, indicating that the cluster loses its spherical morphology at higher impact energies.
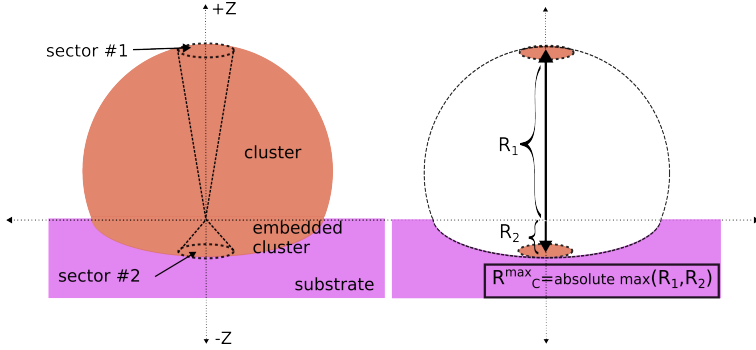
Figure 5.2.: Calculating R_C^{max} of a deposited cluster: The construction used to evaluate the R_C^{max} of single deposited cluster, as depicted in Figure 5.1b.

At energies ≥ 3000 meV/atom, an extreme hard landing is observed: the cluster embeds itself into the substrate during impact, being reflected in a negative R_C^{max}. The cluster adopts a concave shape on the substrate. With increasing impact energy, the cluster deforms more and embeds deeper into the substrate.

In the context of formation of CAMG films, i.e., when multiple clusters are deposited over each other layer-by-layer, intermixing between clusters is expected at the higher impact energies. Based on the results of the single cluster deposition, impact energies between 60-600 meV/atom were chosen to study the formation of CAMG films. In the following section, as part of a first analysis, the changes of the core-shell structures during multiple cluster deposition will be considered.

5.2. Identifying Cores and Interfaces

The deposition of multiple clusters, with clusters derived from 10^{10} K/s $Cu_{50}Zr_{50}$ MG, was simulated at 60 meV/atom, 300 meV/atom, 600 meV/atom impact energies to mimic the soft, medium, and hard-landing in the CAMG film samples, respectively. Additionally, a deposition at an extreme energetic condition was simulated with an impact energy of 6000 meV/atom. The hexagonal close-packed (HCP) arrangement (chosen for reasons mentioned in Section 4.3) for each impact energy was achieved in the following manner: before each new cluster was deposited, the clusters that were already present in its neighborhood were relaxed for at least 2 ns. Every simulated CAMG had three layers of

such cluster depositions, with ∼50 clusters in each layer. The deposition sequence and the processes occurring during impact can be followed in the Supplementary Video V2, which shows the simulation of the deposition of CAMGs in comparison to that of the compaction in the NG processing.

Figure 5.3 shows cross-sections of the films, similar to Figure 5.1a, after equilibrating the sample for 2 ns after the deposition of the last cluster. The yellow and magenta colour coding denotes the shell and core atoms of the clusters prior to deposition, similar to Figure 4.9 and Figure 5.1. No evidence for porosity is observed even for the soft-landing sample (60 meV/atom case) by evaluating a surface mesh with a probe sphere radius of 2.4 Å [137, 139].

At the lowest impact energy of 60 meV/atom, it is observed that, like in Figure 5.1b, the deposited clusters mostly retain their initial sphericity. The cluster sphericity is progressively lost with increasing deposition energy. Next, it should be noted that the first layer of clusters has resided on the substrate for at least 24 ns (using the deposition protocol described) by the time the final layer is deposited. Nevertheless, the interdiffusion of the core and shell atoms is quite low for deposition energies even up to 600 meV/atom. In the energy range of 60-600 meV/atom, the shell atoms, i.e., the former surface atoms of the free cluster prior to deposition, are forming a distinct inter-connected network, which can be interpreted as atomically thin interfacial regions between the cores of the clusters. The former shell atoms (coloured yellow as mentioned above) of the clusters are hence defined to constitute the cluster-cluster interfaces. At the impact energy of 6000 meV/atom the interfacial regions vanish completely.

Additionally, at 6000 meV/atom deposition energy, the film shows significant atomic intermixing between the substrate and the film (see Figure 5.3, visualising the black substrate atoms found in the film, and magenta and yellow atoms from the deposited film embedded in the substrate). For the case of the 6000 meV/atom energy, it is estimated that 8% of the atoms originally in the film are mixed into the substrate, whereas for the case of the 600 meV/atom impact energy this value is about 1.7%.

Similarly, the mixing of the substrate atoms diffusing into the film was also ascertained, by tracking the substrate atoms in the final deposited films. The mixing of the substrate atoms into the film has been estimated to be 6% for 600 meV/atom case, and is 16% for the 6000 meV/atom case. For both the film and substrate atoms, the diffusion into the neighboring medium is higher at higher impaction energies.

Up to now, the locations of the atoms, located initally at the surfaces of the clusters prior to deposition, have been followed (using the magenta and yellow colour scheme for the core and shell atoms, respectively) to determine the interfacial regions in the samples prepared with impact energies in the range below 600 meV/atom. This approach does not provide any information on the energetic state of the atoms in the CAMGs or on the
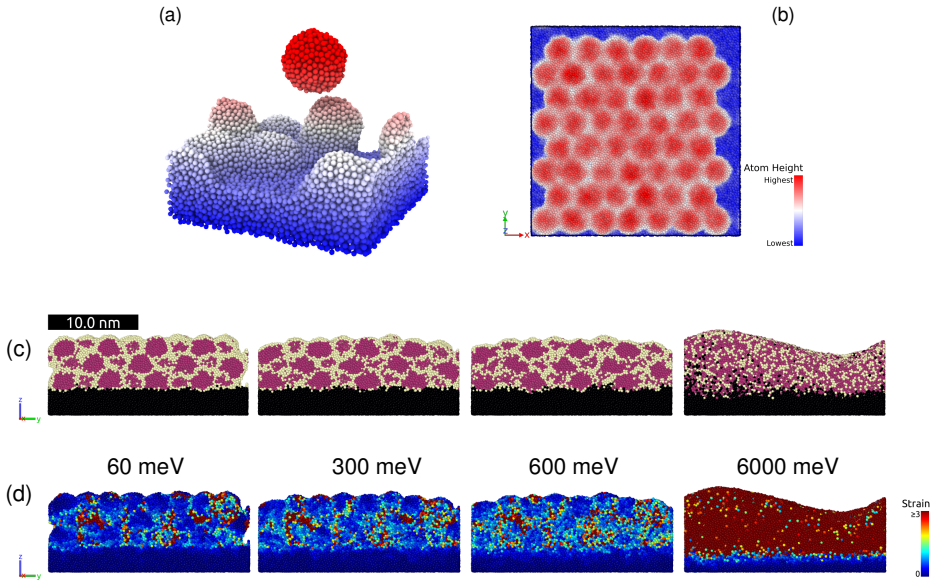
Figure 5.3.: Deposition of CAMG cilms: (a) A depiction of the deposition of a cluster onto the substrate and (b) a top view of the clusters deposited in a HCP arrangement (colour coded by the atom height in the deposition axis) (c) A vertical crossection of the deposited films at 60, 300, 600, and 6000 meV/atom energies, with cluster-core atoms in magenta, and cluster-shell atoms in yellow. The substrate atoms are coloured in black. We observe that the shell atoms form a network of interfaces across the film at least up to 600 meV/atom deposition energy. (d) When colour coded with von Mises shear strain, the interfacial atoms correlate with the higher strained atoms.

local environments in the cores and interfaces. In a first step towards a more detailed analysis, the von Mises shear strain for each of the CAMG atoms was determined [139]. A cut-off radius of 3.8 Å was chosen to compute the strain tensor. In Figure 5.3d, the high strain regions can be clearly correlated to the interfacial network shown in Figure 5.3c for all impact energies below 600 meV/atom. Only for the highest impact energy, no sign for the presence of interfaces can be found, similar to the observation in Figure 5.3c.

The correlation observed for CAMGs is consistent with Gleiter's original definition of interfaces [84] in NGs, in which the interfaces were assumed to be regions of distorted and sheared coordination among adjacent clusters. The strain maps in Figure 5.3d confirm that an interfacial structure is formed and is retained in the range of 60-600 meV/atom impact energies.

Upon inspection of the simulation snapshots in open visualisation tool (OVITO), the cores and interfaces in the CAMG film samples made by soft-to-hard landing deposition are found to reflect a chemical heterogeneity similar to what was originally present in the free clusters prior to deposition (described in Figure 4.9a), with the Cu concentration of 46 at. % in the cores, and 54 at. % in the interfacial regions. The overall composition of the CAMG films are found to be $Cu_{50}Zr_{50}$ (with 1% deviation), same as of the original clusters. The atoms in the CAMG film sample for the extreme hard-landing case of 6000 meV/atom indicate a loss of core and interface structure, and in this manner resembling the MGs obtained by RQ. This loss of core-interface structure, also observed from von Mises local strains is indicative of a high deviation of atoms from their as-deposited positions in the clusters, likely due to local melting and resolidification near the deposition sites. It should be mentioned that the processing of NGs and CAMGs seems to differ in one aspect: at the harshest conditions, i.e., at the extreme hard-landing case for CAMGs and at the highest pressures for NGs, the final structures are different. In NGs, the interfacial regions continue to exist even at the highest pressures, while the interfacial regions disappear in CAMGs at the extreme hard-landing. This most likely is caused by the differences between the compaction and deposition processes. While the cold compaction shears the entire arrangement of clusters together, the sequential deposition of the clusters along with local heating due to the inelastic collision may result in the dissolution of the cluster structure. Therefore, the energetic impact of clusters is considered as a novel process leading to metallic glasses. CAMGs also contain interfacial regions with a modified structure, which differs from that of RQ MGs and NGs prepared by high pressure compaction. However, it is not clear if the structural details of the interfacial regions of CAMGs and NGs are identical, implying that different properties for RQ MGs, NGs and CAMGs are very well possible. Consequently, there is a need to further investigate the NGs and CAMGs both experimentally and using simulation methods.

The CAMG samples are also different from both the MGs and the NG, in the following fashion: the CAMGs only partially fill a simulation box. It is important to clarify that the unfilled volume referred to is not within the film, rather it is between the upper surface of the film and the upper wall of the simulation box. The open surface at the top in the CAMG film samples is expected to give rise to surface artefacts—including defective surface coordinations, larger atomic occupancy and excess surface energy. The surface interaction between the cluster atoms and the substrate will also lead to defective

coordinations at the border. It was decided to first analyse the entire CAMG film sample, and then later represent the data from a slab of fixed dimensions present within the inside of the deposited film samples, in order to avoid the surface artefacts, as shown in Figure 5.4 (Tip for OVITO users: the atoms have to be deleted from the data only after any OVITO-API calls have been performed).
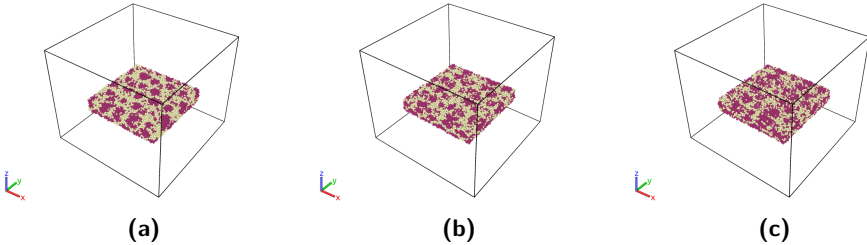

Figure 5.4.: Representative slabs of CAMGs: To avoid surface artefacts, these slabs were cut out of the CAMG (a) 60 meV/atom (b) 300 meV/atom and (c) 600 meV/atom films.

Another possible method of removing surface artefacts is to query the surface atoms by means of a surface mesh, and deleting them from the slab before plotting the analysed data. When deleting surface atoms by using the surface mesh, the deleted atoms are majorly made up of the interface atoms. Moreover, the CAMGs deposited at lower energies have more distinct morphologies at the top surface of the film, meaning that the number of deleted surface atoms in this case will be larger than for a CAMG deposited at higher energies. This would result in the representative samples not consistently having the same number of core and interface atoms in the CAMGs. For the fixed slab method, however, the volume and the consistently similar amounts of core and interfacial atoms, allows for a consistent analysis of the effects of core and interface regions. Hence, the first method of representing data from fixed slabs is preferred in this thesis.

Based on the presented results, a structural model for the CAMGs is proposed, similar to that of NGs. In this model, interfacial regions, which are chemically different from the core regions due to the surface segregation observed in the individual clusters, are formed during the cluster deposition in the range of impact energies between 60–600 meV/atom. The only exception is, as mentioned above, the structure for an impact energy of 6000 meV/atom, for which interfaces are totally absent. Therefore, in the following sections, only simulations of CAMGs deposited at the impact energies 60, 300, and 600 meV/atom, are being considered. Incidentally, this energy range corresponds well with the energy range used in the cluster experiments reported in [30].

The prepared CAMGs in this chapter are compared to corresponding NGs and RQ MGs. Moreover, a heat treatment as described for the single cluster (Section 4.2) can also modify the metastable state and structure of a MG. Therefore, the as-prepared MG sample, i.e., quenched directly from the liquid phase, was subjected to a heat treatment identical to the one used for the single cluster to determine the changes in the structure of the MG sample. In addition to the as-prepared MG, the heat-treated Metallic Glass (MG_ht) serves as a reference structure for the NGs and CAMGs prepared by compaction and energetic impact, respectively. In the following discussion up until Section 5.7, the NGs and CAMGs derived from the cluster made only from the 10^{10} K/s MG are considered.

5.3. Local Structure Tailoring in CAMGs

To obtain a more detailed insight into the structure of CAMGs, in particular the interfacial regions, the normalised partial radial distribution function (PRDF) of the CAMGs, NG, and the MGs were studied (see Figure A.7 in Supplementary Material for more details). Like in Section 4.1, the Cu-Cu (2.45 Å), Cu-Zr (2.8 Å), and Zr-Zr (3.25 Å) first peak positions of the MGs match well with those previously reported values [141, 142]. Even the NG and CAMGs follow the same pair distributions as those of MG. Moreover, no significant change in atomic pair correlations both in the core and the interfacial regions are observed. This prompts the study of the local short-range order (SRO).

The local atomic environment is typically represented using the Voronoi analysis method, and the polyhedra are represented by a $<n_3\ n_4\ n_5\ n_6>$ Schäfli index (See Section 3.2.2). Figures 5.5a-c show the top seven frequent Voronoi polyhedra (VP) (arranged in the numerical order of the indices) for CAMGs, NGs, MG_ht, and the precursor MG quenched at a rate of 10^{10} K/s. In Figure 5.5a, the histograms of the VP for all the atoms constituting the entire six sample sets are shown, whereas Figures 5.5b-c denote the histograms for the core and interface atoms, respectively. The index <0 0 12 0>, which represents the full-icosahedral (FI) coordination, is the highest occurring in the MG, amongst all the six glasses. For the 10^{10} K/s MG, the heat-treatment reduces the FI order as seen in MG_ht. The next highest occurring index is the <0 2 8 2>, which is known to be an icosahedral-like (ICO-like) polyhedron [78, 136]. Its occurrence is highest in MG and MG_ht when compared to the NG and CAMGs. As mentioned in Section 3.2.2, the VP known to be classified into four main categories [78]. The are mentioned here again for the benefit of the reader: 1. icosahedral-like: <0 0 12 0>, <0 0 10 x>, and <0 2 8 x>; 2. crystal-like: <0 4 4 x> and <0 5 2 x>; 3. mixed coordinations: <0 3 6 x>, where 0 ≤ x ≤ 4; and 4. other remaining indices. With this knowledge, it is noticed that in the NG and CAMGs the other prominently occurring polyhedra in Figure 5.5a-c are of the icosahedral-like and mixed coordination types.
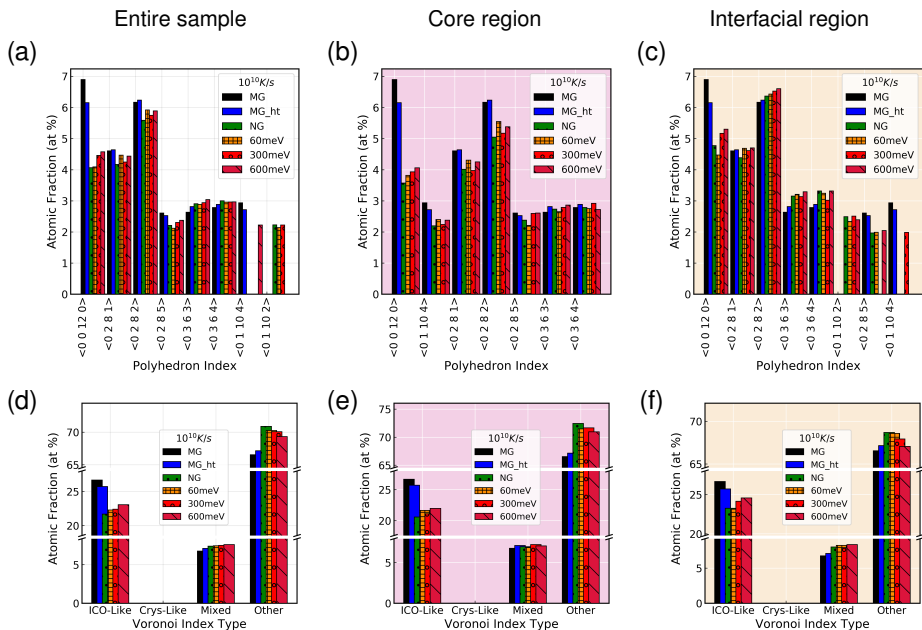
Figure 5.5.: full-icosahedral short-range order recovers in CAMGs with deposition energy: The top 7 Voronoi indices arranged based on numerical order, without considering any special central atom species (Cu/Zr) in the VP. The Voronoi histograms are shown for (a) the entire representative sample, (b) the core atoms, and (c) the interface atoms, respectively. The magenta and yellow backgrounds in the figures are rendered to represent the core and interface cases, respectively. Figure 5.5 (d), (e) and (f) show the indices sorted into known groups of coordinations. Crystalline coordinations are absent in all of the simulated glasses, in particular in the MG_ht, NG, and CAMGs where a heat-treatment is involved in the simulation process. The FI-order and icosahedral-like order (ILO) in CAMGs increase systematically with deposition energy

Furthermore, the Voronoi indices are sorted based on the above rules for the six simulated

glass samples and represented in Figure 5.5d-f, in order to facilitate the analysis of the dominant index classes in comparison of the different metallic glass structures. It is first noticed that crystalline coordinations do not occur in any of the simulated metallic glass samples, especially in the MG_ht and the CAMGs, despite the heat treatment involved in their processing. Especially, the lack of any crystalline coordinations confirms that all the simulated CAMGs are fully amorphous, both in the cores and in the interfaces.

In the CAMGs and NGs a significantly reduced short-range FI order was observed, consistent with previous studies of NGs [90]. This trend is also seen in the analysis of the ILO. The present simulations of the RQ $Cu_{50}Zr_{50}$ MGs have shown that less stable MGs (prepared at higher quench rates) are accompanied by a reduction in FI fractions and also in the ILO (refer to Figure 4.2 in Section 4.1.2), as reported by Yue et al. [78]. The tendency of a decrease of stability in the NGs and CAMGs with decreasing ILO is further discussed in Section 5.5.

The sorted VP histograms for Cu-centred and Zr-centred coordinations are depicted in Figure 5.6 (The unsorted Voronoi indices distribution is indicated in Figure A.8 in Supplementary Material). The ILO is observed to be higher for Cu atoms than for Zr atoms for all the six metallic glass samples that have been studied. The Cu-centred atoms make up the majority in contributing to ILO. Also seen is the increasing ILO in Cu-centred atoms in the CAMGs with deposition energy.

Looking back at Figure 5.5e-f, it is observed that for NGs and CAMGs, both FI order and the ILO indices are respectively at least 1% and 5% higher in the interfaces compared to the cores. It is evident that the interfaces, being richer in Cu compared to the core regions, exhibit higher FI as well as higher ILO. This indicates that the interfaces must be better packed than the core regions[3].

Interestingly, a systematic increase in FI order (See Figure 5.5c) in the CAMGs with increasing impact energy is observed. This trend, also seen in the ILO fractions of the entire sample, is especially prominent for the interfaces (see Figure 5.5f). We recall that the interfaces are defined as the surface atoms of the undeposited clusters, and for this reason it should be noted that the interfaces for all impact energies have the same chemical composition. The increase in the FI-order and ILO in the interfacial atoms can then be interpreted to be the direct result of the CIBD process. In both the core and interface atoms, another striking feature is the systematic increase of ILO in the CAMGs with increasing deposition energy, recovering towards the ILO of MG and MG_ht. The present model demonstrates the possibility of tailoring the local amorphous order with impact energy for metallic glasses synthesised via the CIBD route.

---

[3]The correlation of ILO of cores and interfaces in the CAMGs and NGs, with their stability is discussed in Sections 5.5 and 5.7
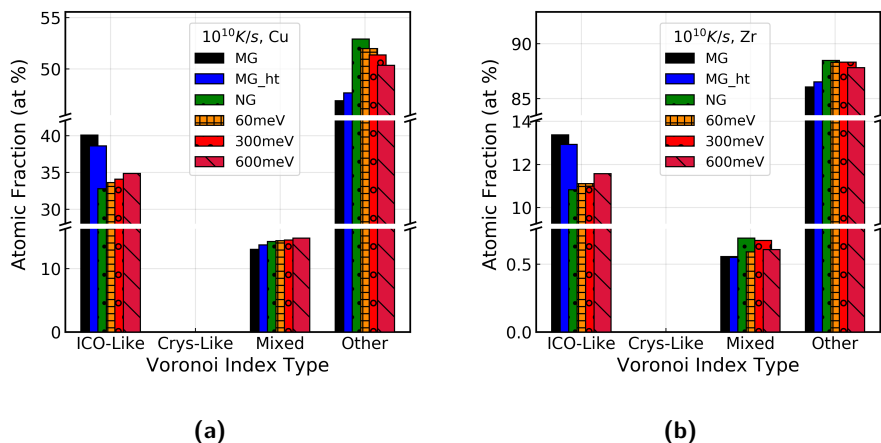
(a)   (b)

Figure 5.6.: Sorted Voronoi polyhedra for Cu- and Zr-centred atoms in MGs, NGs, and CAMGs: The atomic fractions here are defined w.r.t the same species i.e., at. fraction of Cu is the fraction of Cu atoms exhibiting a certain local order.

5.4. Atomic Volume Analysis

The normalised distribution of the atomic coordination volumes, or Voronoi volumes [21, 145] for all the atoms in the six metallic glass samples was studied using the Voronoi analysis. Figure 5.7a shows the volume distribution with two peaks approximately at 13.9 Å^3 for Cu and 21.8 Å^3 for Zr, which indicates the volumes occupied by the Cu and Zr atoms. The Cu atoms are observed to have lower volume occupancies compared to those of Zr atoms. Cheng and Trelewicz [21] reported similar distributions in $Cu_{64}Zr_{36}$ nanoglasses, however, with the volume per atom peaks shifted to the left, likely caused by the fact that $Cu_{64}Zr_{36}$ MGs are denser than the $Cu_{50}Zr_{50}$ MGs [151]. Furthermore, the CAMGs are similar to the NGs and MGs in terms of atomic volume distributions. It is also noticed that the distributions in the core and in the interfaces are not significantly different from each other (see Figure A.9 in Supplementary Material). Using the volume distributions in Figure 5.7a, the exclusion of the surface atoms in the analysis (detailed in Section 5.2) of CAMGs was cross-verified. The surface atoms occupy higher volume per atom than average, and when included in the volume analysis, are known to alter the volume distributions of Cu and Zr atoms with a shoulder to the right of each main peak

[21]. The absence of such shoulders indeed ascertains the absence of surface atoms in the representative Figure 5.7a.
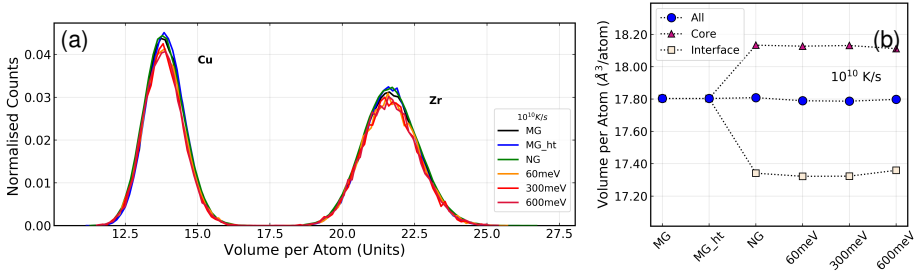

Figure 5.7.: Reduced volumes in CAMG samples: (a) The normalised volume per atom distribution shows similar behaviour for the six metallic glass samples. (b) Average volumes of the atoms show that the core regions are less densely packed than the interfaces.

In Figure 5.7b, which shows the average volume/atom values for all six metallic glass samples, it can be seen that, on average, the atoms in CAMGs and NGs occupy similar volumes. Furthermore, the impact energy does not have an influence on the average volume of the CAMGs. The core regions in the NGs and CAMGs present a higher volume occupancy. By contrast, the opposite behaviour is observed for the interfacial atoms. When all of the atoms are considered together, the increase of volume for core atoms and the decrease of volume for the interface atoms in CAMGs and NGs offset each other to result in similar volume occupancies as MGs prepared by RQ. While the interfaces in NGs have previously been reported to be less dense in the MG [17, 19], this need not hold true for the CAMGs as well. The interfaces are richer in Cu-atoms, which, on an average, occupy lower volumes compared to Zr-atoms. The interfaces in the present CAMGs model have an increased density due to the chemical effects, and this is consistent with previous studies of segregated planar interfaces by Adjaoud and Albe [22].

5.5. Potential Energy Inspection

In Figure 5.8a, the normalised potential energy (PE) distribution of the simulated CAMGs, NG and MGs are summarised. The Cu and Zr atoms exhibit two separate distributions, with the peaks of -3.5 eV for Cu atoms and $\sim$-6.4 eV for Zr atoms. By contrast to the
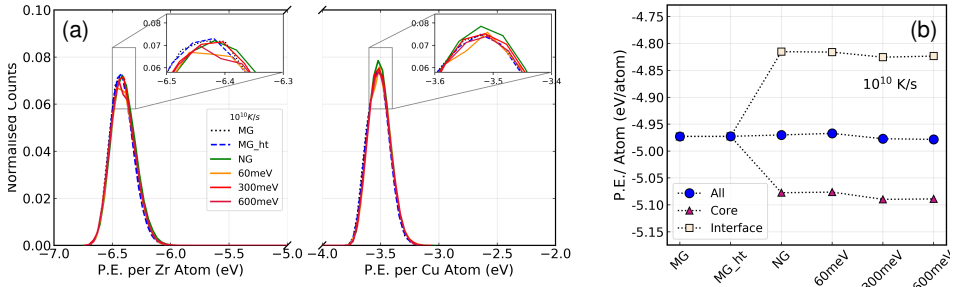
Figure 5.8.: PE/atom states of the CAMGs, NG and the MGs: (a) The normalised PE distributions for the six glasses. (b) The average PE per atom, also in the core and interface regions for all the glasses.

atomic volume distribution behaviour, where the Cu atoms occupied lower volumes, the Cu atoms have a higher PE overall in comparison to Zr atoms. The absence of right shoulders in the PE distribution peaks, like in the volume distributions discussed in Section 5.4, once again confirms the absence of surface atoms in the representative CAMG slabs.

Figure 5.8b summarises the average potential energies for all atoms in the MG, MG_ht, NG, and the CAMGs and the average potential energies of the atoms in the core and interfacial regions in the NG and CAMGs, deposited at the different impact energies. All of these six metallic glasses samples have been made from a 10^{10} K/s Cu$_{50}$Zr$_{50}$ glass. It is observed that the core and interfacial atoms in the CAMGs and NGs can be distinguished by their energetic states. The core atoms occupy lower energy states, about 2% lower than that of the atoms in MGs prepared by RQ, whereas the interfaces possess higher energies 6% higher compared to those of the MGs. While the interfaces are better packed than the cores, as seen in Section 5.4, they occupy a higher energy state than the MGs. From liquid quenched traditional metallic glasses simulated in Section 4.1, it is known that the total PE of the glass increases with increasing Cu concentration maintaining the same quenching rate (See Figure 4.4). Hence, it can be explained that the higher Cu concentration in the interfaces, results in the interface atoms residing at a higher energy state. We conclude that the core regions stabilise the CAMGs and the NGs. Denser packing at the interfaces does not necessarily correspond to a lower energy state in the NGs and CAMGs due to their chemical heterogeneity.

5.6. Medium-range Order in CAMGs

In this section, the medium-range order (MRO) in all six metallic glasses (3 CAMGs, NG, MG and MG_ht) shall be inspected to better understand the connectivity of the FI units in the MG and MG_ht and how the MRO varies in the CAMGs with the deposition energy.
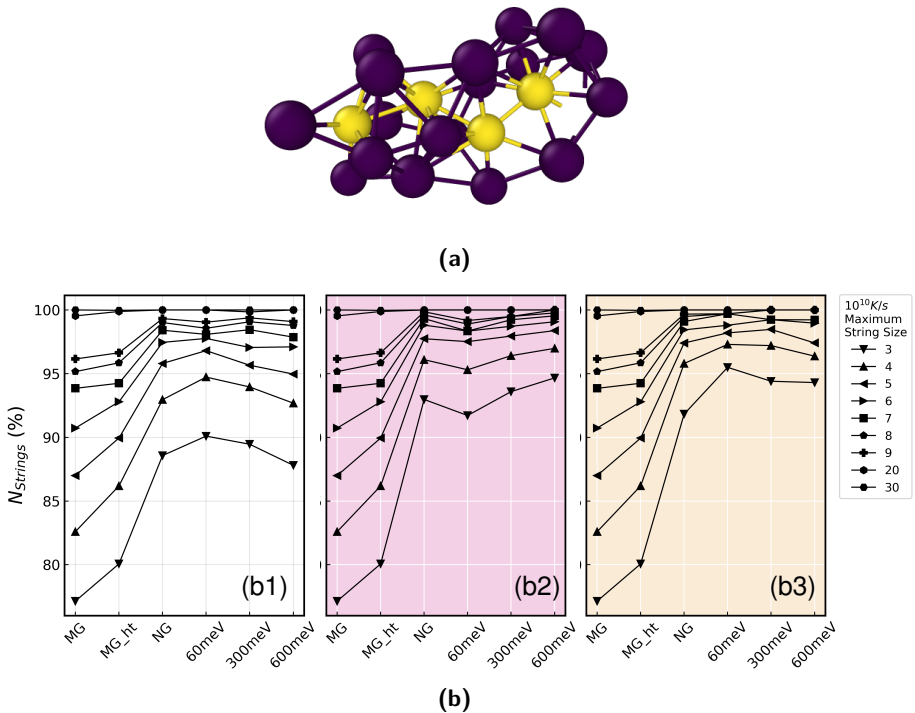

(a)

(b)

Figure 5.9.: FI-strings in MGs, MG_ht, NG and CAMGs: (a) An FI-string (yellow atoms) seen in the 60 meV/atom CAMG (b) Number of atoms (%) in the glass samples having strings of sizes less than a cut-off value. See text for more details.

The relative packing of coordination polyhedra centred around solute atoms is used to define MRO in metallic glasses; it has been shown that the solute atoms exhibit string-like

connectivity when the solute concentration goes beyond 20-30 at.%, [56]. Similarly, the string-like connectivity of FI-atoms, which are the atoms residing in FI coordinations, have been reported to indicate MRO, as icosahedral <0 0 12 0> clusters have a strong tendency to aggregate with each other [58, 67, 151]. Interpenetrating string-like networks of atoms in FI environments have been reported before as indicative of MRO, including the studies by Lee et al. [80] and Ritter et al. [23]. To visualise these strings for the glasses simulated in this work, bonds were constructed using OVITO for FI-atoms with other FI-atoms, present within a cut-off radius of 3.5 Å.

Figure 5.9a shows one of the FI-atom chains found in one of the CAMGs. The yellow coloured atoms are the ones in the FI environment, the blue atoms are the surrounding atoms in the coordination polyhedron. In Figure 5.9b, the number of strings (% of total strings) below a maximum string length are described for all FI-atoms (Figure 5.9b1), FI-atoms in the cores (Figure 5.9b2) and FI-atoms in the interfaces (Figure 5.9b3) for the NGs and CAMGs.

The number of small strings of sizes 3-9 recover in the CAMGs, specifically in the interfaces towards MG and MG_ht values with increasing deposition energies. In the glasses, at least 74% of all linked atoms are in 3-atom or longer string-like networks. This behaviour is seen in both the cores and the interfaces of the CAMGs and NGs as well. The MROs of all the glasses in the context of the larger strings of length 40-100 are similar as characterised by the chosen metrics.
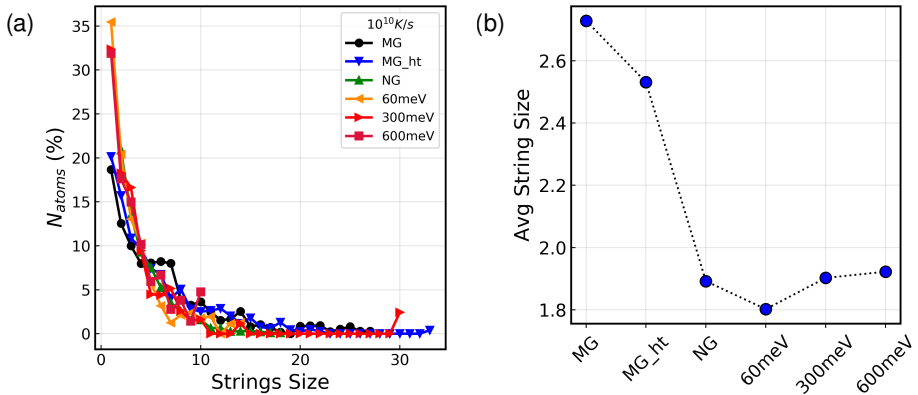

Figure 5.10.: **MRO in 3 nm CAMGs and NGs**: (a) Distribution of the number (%) of atoms existing in FI-strings of varying sizes (b) Average FI string size in the six glasses.

Figure 5.10a shows the fraction of FI-atoms in each of the glasses made from a 10^{10} K/s MG, which are present in a string of a given size. From both Figures 5.9b and 5.10a, it is evident that most FI-atoms exist in small strings. However, the number of atoms in small strings (3-5 FI-atoms in size) is the lowest in the MG and MG_ht. A higher percentage of larger-sized strings is seen in the MG, MG_ht and NG. This can be attributed to the geometry of the samples: larger strings can form in MG, MG_ht, and NG cases due to periodic boundaries conditions in all directions, and the simulation box being completely filled. Such strings of larger sizes cannot be expected to form in the CAMGs, as the sample considered for analysis without surface artefacts is limited by the dimensions of the representative slabs from within the CAMG films. However, amongst the 3 CAMGs, it can still be noted that a 600 meV/atom CAMG has more 3 FI-atom strings than the 60 meV/atom CAMG. This trend is seen for strings of at least 5 FI-atoms in length.

Figure 5.10b shows the average string size for all simulated glasses. The average string size in NG and CAMGs is about 40% lower than for MG and MG_ht. However, with increasing deposition energy, a slight increase in average string size in the CAMGs deposited at 300 and 600 meV/atom compared to the 60 meV/atom CAMG is observed. This indicates that with increasing deposition energies in the CAMGs, the MRO of the strings of FI-atoms can be at least partially recovered.

A comparison of the present results with the available experimental data including the structural and magnetic information on $Fe_{80}Sc_{20}$ CAMGs [30] is not possible as the current simulations are specific to the $Cu_{50}Zr_{50}$ metallic glass, and also due to the non-availability of an embedded atom model (EAM) potential for $Fe_{80}Sc_{20}$ systems. However, some conclusions on the behaviour of cluster-assembled glasses, in particular on the of the medium-range order in CAMGs, can help to better understand the experimental results for $Fe_{80}Sc_{20}$ CAMGs, in particular the comparison to the local motif analysis reported in [30]. As the local order in CAMGs recovers towards the metallic glass values with increasing impact energies, an increase in the size of the string-like MRO networks is expected. This behaviour could explain the strengthening of exchange interactions, and thus the observed increase in the T_C, i.e., the ferromagnetic transition temperature with increasing impact energy.

5.7. Influence of Quench Rates on Final Structure of CAMGs

In this section, we explore the dependence of the final metastable states of the NG and CAMGs on the initial processing conditions of the clusters themselves. This could help to understand the CIBD process and would allow one to traverse the potential-energy landscape (PEL) of metallic glasses. One important processing condition in the

simulation is the quenching rate of the MG from which the clusters are formed. Therefore a comparison of CAMGs and NGs, prepared with different quenching rates, is performed.

The MG, and MG_hts, were prepared at three quench rates of 10^{10} K/s, 10^{12} K/s and 10^{14} K/s. Subsequently, clusters were derived from them for the three quench rates, using which the CAMGs and the NGs were prepared. All the glasses were compared against one another in terms of local icosahedral SRO and potential energy. As mention in Section 4.1.4, the current potential does not correctly reproduce the volume behaviour of RQ MGs with quench rates, and hence the comparison glasses' volume behaviour with quench rates is not attempted.

Figure 5.11 describes the FI order in the glasses. The fraction of FI in RQ MGs is highest at 7% for the 10^{10} K/s MG, and at 5.5% and 3.8% for the 10^{12} K/s and 10^{14} K/s MGs respectively. The MG_ht FI drops at low quench rate of 10^{10} K/s, but increases at 10^{14} K/s, revealing that the heat-treatment causes different effects at different quench rates. Compared to the MG_ht, the NGs and CAMGs appear to consistently demonstrate lesser FI-packed states for the three quench rates. For the CAMGs and NGs, the FI-order in the core and interfacial regions are also represented. As seen in Section 5.5, the interfaces possess higher FI-packing than the cores for the CAMGs and NGs. The order in the entire NGs and CAMGs sample is depicted as 'All' in the Figure 5.11. Amongst the CAMGs and NGs, the NGs have the lowest FI-order. For the three quench rates, a trend of increase in the FI-order with increasing deposition energy is hinted; as the FI-order for the 600 meV/atom CAMG is greater than that for the 60 meV/atom CAMG. However the FI-300 meV/atom CAMG does not follow this trend for the 10^{12} K/s and 10^{14} K/s cases. The ICO-like was considered as an alternative candidate to explore SRO.
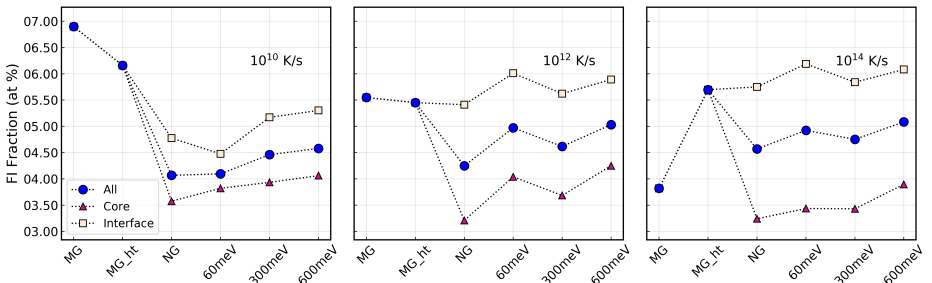

Figure 5.11.: Full-icosahedral ordering versus quench rates: The FI in the CAMGs and MGs, in comparison to their precursor MGs and MG_hts is invariant with the quench rate used.

It has been discussed previously in literature [74] that the distinction between FI and ICO-like coordinations is ambiguous, owing to the defined threshold of a distortion tolerance set while performing the Voronoi tessellation. In the previous sections, it has also been mentioned that the ILO is a well-known indicator of glass stability and of packing [74, 75, 78, 79]. Now, the ILO behaviour in CAMGs is observed with respect to the processing conditions of the RQ MGs, from which the clusters are derived. CAMGs made from fast-quenched 10^{12} K/s-MGs and 10^{14} K/s-MGs were investigated. For these reasons, ILOs of the six glasses are also examined. Figure 5.12 shows the variation of the ILO for three different quenching rates of the MGs from which the clusters were prepared. Firstly, it can be seen that the ILO in the MG decreases with increasing quenching rates. Secondly, the heat-treatment for the MGs results in different behaviours for the different quenching rates. For the MGs prepared with cooling rates 10^{10} K/s (Figure 5.12a) and 10^{12} K/s (Figure 5.12b), the heat-treated glasses MG_ht exhibit lower ILO than the MG. At the highest cooling rate of 10^{14} K/s, the same heat-treatment places the MG_ht at a state with higher ILO value (Figure 5.12c). Given that the clusters undergo the same heat-treatment as MG_ht, the NGs and CAMGs can be compared with the MG_ht.

At all quenching rates, it is noted that the interfaces exhibit higher ICO-like SRO than the cores, due to the chemical effects discussed in Section 5.3. The CAMGs, however, show an increase in the ILO with increasing impact energies, for all the three quench rates used in the present study. Therefore, it is concluded that for a given cooling rate of the as-prepared clusters, the CIBD process determines the final ICO-like states of the CAMGs.
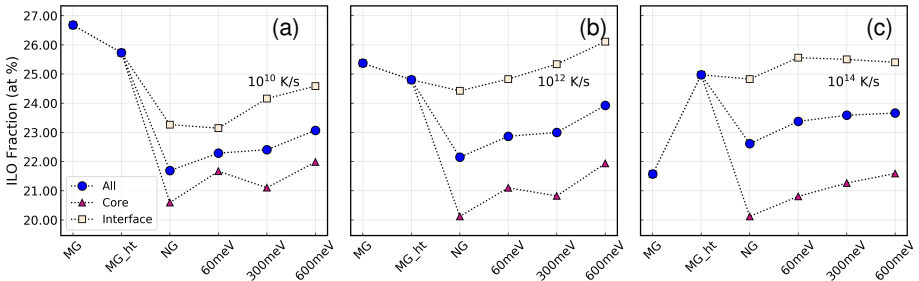

Figure 5.12.: Icosahedral-like ordering versus quench rates in CAMGs: Variation of ILO in the various NGs and CAMGs and MGs, compared to their precursor MGs and MG_hts for cluster derived from (a) 10^{10} K/s, (b) 10^{12} K/s, and (c) 10^{14} K/s $Cu_{50}Zr_{50}$ RQ MGs.

Figure 5.13a shows the average PE per atom for the cores, interfaces and the entire sample for the six glasses, and for the three cooling rates. In Figure 5.13b, the average PE of only the entire sample is represented, and a possible representation of the PEL has also been illustrated and overlayed upon the plots. We observe that while in the low cooling rate cases of 10^{10} K/s and 10^{12} K/s $Cu_{50}Zr_{50}$ glasses, the MG_hts are at a higher energy states, indicating a rejuvenation process [152, 153]. This is consistent with the ILO behaviour of MG and MG_ht. Furthermore, when examined across the quench rates, the potential energies of the glasses are lower at lower quench rates.
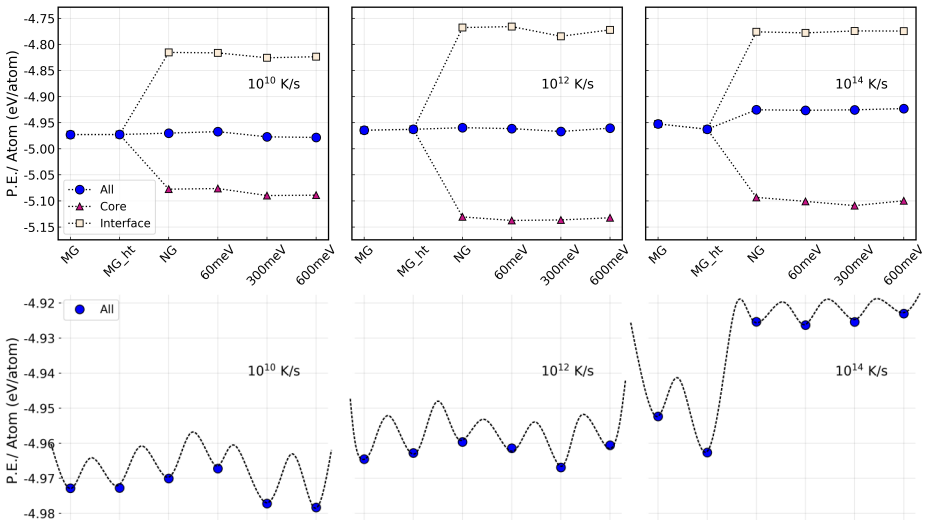

Figure 5.13.: **Average PE of CAMGs versus quench rates**: (a) The normalised PE per atom in the various CAMGs and NGs, in comparison to their precursor MGs and MG_hts for three different quench rate cases. (b) The average PE per atom in the metallic glasses, along with an imagined depiction of the PEL.

The CAMGs and NGs however, for any given cooling rate, do not show any clear trend in the potential energies. Unlike in the MG and the MG_ht, the stability and ILO packing do not correlate with each other in the CAMGs and NGs. For a CAMG prepared

at a given impact energy, the ILO packing increases with quenching rate. The NG is consistently at a higher energy state than the MG_ht at all quench rates. In contrast, the potential energies of the CAMGs decrease with impact energy for the lower quench rate case of 10^{10} K/s, but at higher quench rates of 10^{12} K/s and 10^{14} K/s, the difference in the energy states of the NGs and CAMGs is seen to diminish. This seemingly random behaviour could be an effect of the local atomic strain accumulated during the deposition process.

It may be that the strain energy has a lower effect for glasses quenched at lower rates. It may also be that the strain energy gained due to CAMG processing could be erratic, and dominating the stability gained from the quenching in the NGs and CAMGs, leading to the observed behaviour. In Figure 5.3d, the strain analysis shows that von-Mises strains for the 3 nm clusters studied here are higher in both NGs and CAMGs, compared to previous reports for 7 nm cluster NGs [20]. This leads to the conclusion that the size of the clusters plays an important role in the final structures attained by the CAMGs. Further studies with different cluster sizes, including size distributions, and random deposition locations are needed to gain further understanding on the role of the processing parameters in cluster assembled metallic glasses prepared by compaction (NGs) and by energetic impact (CAMGs).

5.8. Summary

In this chapter, the simulated $Cu_{50}Zr_{50}$ CAMGs were studied and characterised. The present model of CAMGs uses chemically segregated amorphous $Cu_{50}Zr_{50}$ clusters of $\sim$800 atoms, which are 3 nm in diameter, being deposited onto a substrate at different impact energies. These CAMGs are compared with NGs produced by mechanical compaction of the same precursor clusters, and to the conventionally prepared melt-quenched metallic glasses of the same composition.

In the CAMGs, two chemically distinct amorphous phases were observed: cores and interfaces, which constitute an interconnected network of interfaces in which the cores with their distinctly different local structure are embedded. The formation of Cu-rich interfaces is observed at impact energies up to 600 meV/atom. Due to the chemical heterogeneity between cores and interfaces, the core regions occupy lower energy states, thus stabilising the CAMG structures. The interfaces appear to be completely absent at the extreme impact energy of 6000 meV/atom.

The FI and ILO short-range order parameters are lower in the NG and CAMG, in the conventional (10^{10} K/s quench rate) case, for both the cores and interfaces. The interfaces
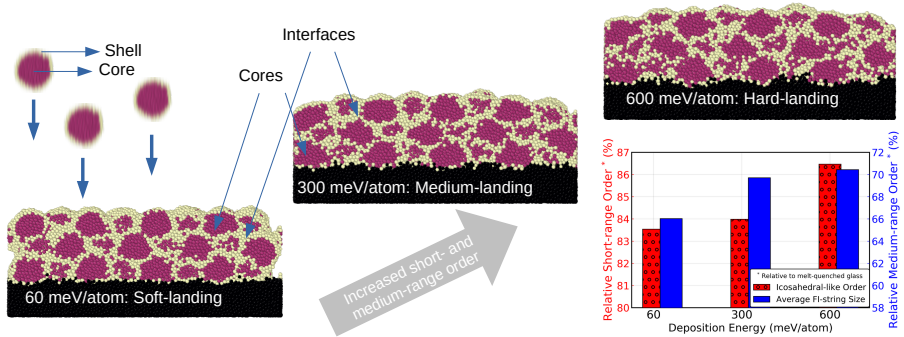
Figure 5.14.: short-range order and medium-range order tailoring in CAMGs: A visual summary of the formation of core-interface structures, and the tailoring of FI-order and FI-string size with deposition energy in CAMGs.

exhibit higher FI and ILO compared to the cores, with a higher density than the cores. A graphical depiction of these findings is represented in Figure 5.14.

The present simulations constitute the first model explaining the mechanisms of local SRO and MRO tailoring in CAMGs by increasing the impact energy. Furthermore, the ILO increases with impact energy, irrespective of the quenching rates used to prepare the 3 nm sized clusters. Consequently, at a fixed overall bulk composition of the metallic glass, control of the local structure is possible by simply modifying the processing conditions. The SRO and MRO in CAMGs recover towards the metallic glass values with increasing impact energies.

6. Cluster-size effects in Cluster-assembled Metallic Glasses

In the last two chapters, a protocol was established to study the cluster-assembled metallic glass (CAMG), and contrast it with rapidly-quenched (RQ) metallic glass (MG) and nanoglass (NG). We observed that the processing of $Cu_{50}Zr_{50}$ CAMGs and NG led to the formation of a core-interface network which influenced the structural characteristics of the materials. Consequently, the nature of the interfaces in terms of length scales are therefore expected to final states of the glassy systems.

For instance, it has recently been shown in various models of the NGs that the diminution of the nanoparticle size or the "grain size" improves the plasticity of the material drastically, characterized by a reduced flow stress [93, 94, 154]. Adopting smaller particle sizes and physical-vapour deposition (PVD) have also lately been shown to correlate with thermal ultra-stability in small-chain polymer glasses experiments [155] and simulated Lennard-Jones (LJ) model-atoms [156]. The current chapter discusses the attempts to explore such size effects in CAMGs and NGs.
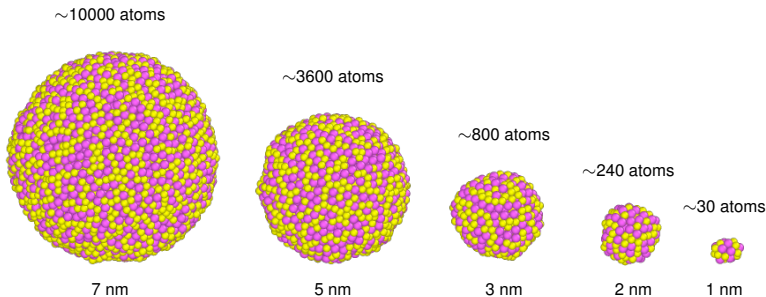

Figure 6.1.: Cluster-sizes and associated length scales: $Cu_{50}Zr_{50}$ CAMG building blocks with diameters in the range of 1-7 nm. The 7 nm nanoparticle has ∼300 times as many atoms as the 1 nm cluster.

6.1. Size-effects in CAMGs

Chapters 4 and 5 describe in detail the CAMGs and NGs made from 3 nm sized clusters. In this section, CAMGs made from monodisperse nanoparticles of two sizes (1 nm and 7 nm in diameter) are studied as a first step towards understanding cluster-size influence.

6.1.1. 7 nm $Cu_{50}Zr_{50}$ Single Nanoparticle Synthesis and Deposition

In previous simulation-based investigations of NGs, nanoparticles of sizes 7-15 nm were chosen [20–22, 92]. Therefore, CAMGs were explored with this nanoparticle[1] size range. A large spherical nanoparticle, 7 nm in diameter, was cut from a $Cu_{50}Zr_{50}$ 10^{10} K/s MG[2]. The resulting nanoparticle contained ∼10,000 atoms, and had a $Cu_{50}Zr_{50}$ composition with 0.3% deviation. After cutting the sphere, the nanoparticle was subject to a short heating above glass-transition temperature (T_g), and cooled to 50 K, similar to the 3 nm cluster (as described in Section 4.2).
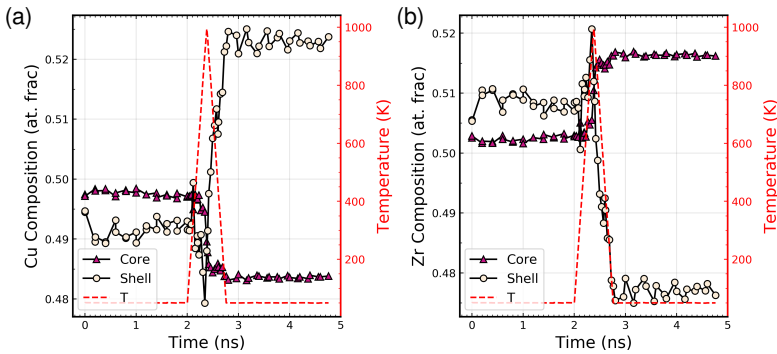

Figure 6.2.: Compositional variation in the 7 nm $Cu_{50}Zr_{50}$ nanoparticle: The evolution of chemical segregation of (a) Cu-atoms and (b) Zr-atoms, in the core and the shell regions of the $Cu_{50}Zr_{50}$ amorphous nanoparticle.

---

[1]It is worth noting that in this chapter, the clusters and nanoparticles, although the same in constitution and composition, refer to two different entities. The clusters refer to small aggregations of atoms—usually in the size range of 10-2000 atoms [28–31, 119], whereas the nanoparticles are the large masses of atoms typically used in the context of NGs [10, 18, 20, 22].

[2]All simulated MGs, NGs and CAMGs discussed in this chapter are made from $Cu_{50}Zr_{50}$ 10^{10} K/s MGs.

A core-shell structure was found to evolve in the 7 nm nanoparticle (See Figure 4.8 in Supplementary Material), with a shell thickness of 3 nm evaluated using a radial composition analysis like in Figure 4.8, Chapter 4. Figure 6.2 describes the variation of Cu and Zr concentrations in the core and shell regions. Like in the 3 nm cluster (Figure 4.9), a sharp change in the compositions in the core and shell is observed with the heat treatment. The high temperature mobilizes the atoms to move to their preferred positions. This configuration is by no means the equilibrium concentration of the nanoparticle, as the atoms need a longer time above the T_g to diffuse across the sphere completely [22]. However, long duration of heat-treatment above T_g is known to produce crystalline nuclei in the RQ MG experiments. Moreover, it was necessary to set the simulation parameters in the 7 nm nanoparticle same as the 3 nm cluster for the sake of consistency.

Nevertheless, the Cu-concentration in the 7 nm nanoparticle is seen to increase in the nanoparticle shell, with a corresponding decrease in the core region. The opposite is observed with the Zr-concentration, which is seen to preferentially segregate to the core. A brief discussion on the driving force behind this segregation is mentioned in Section 4.2 and Reference [22].

After the preparation of the nanoparticle, its deposition on a substrate is studied (similar to Chapter 4). A layered substrate thermal model is once again implemented for reasons mentioned in Chapters 4 and 5. The substrate chosen is 15 nm × 15 nm in the XY-plane, larger than the one used for the single 3 nm cluster deposition. The substrate thermal layers were flat, unlike for the 3 nm single deposition case. In Figure 6.3a, the cross sections of a single 7 nm nanoparticle deposition are depicted, 2 ns after impact[3]. The impact energy of the deposition is varied from 6 meV/atom to 3000 meV/atom. The 7 nm nanoparticle, like the 3 nm cluster (see Figure 4.10) is seen to deform with increasing impact energy. Furthermore, the nanoparticle is also seen to be embedded more into the substrate at higher energies.

At 3000 meV/atom impact energy, some nanoparticle and substrate atoms can be seen to ejected from the substrate, not just from the sides of the impacted nanoparticle, but also along the impact-center, indicating a reflection of impact-shockwaves by the substrate. Such an explosive behaviour would not only be a consequence of the high momentum of deposited nanoparticle, but also a result of the inability of the modelled substrate to dispel sufficient heat from the system (See Section 4.3 for more details).

Although the energy per atom is half the maximum deposition energy of 6000 meV/atom in the 3 nm clusters case (See Sections 4.3 and 5.1), the deposition of the bigger 7 nm size nanoparticle introduces a larger momentum into the system. Since the high impact is not desirable for formation of interfaces, the deposition at 3000 meV/atom case will not

---

[3]The singly deposited nanoparticles at various energies were found to attain a stable configuration after 2 ns of deposition, see Figure A.6 in Supplementary Material for more details.
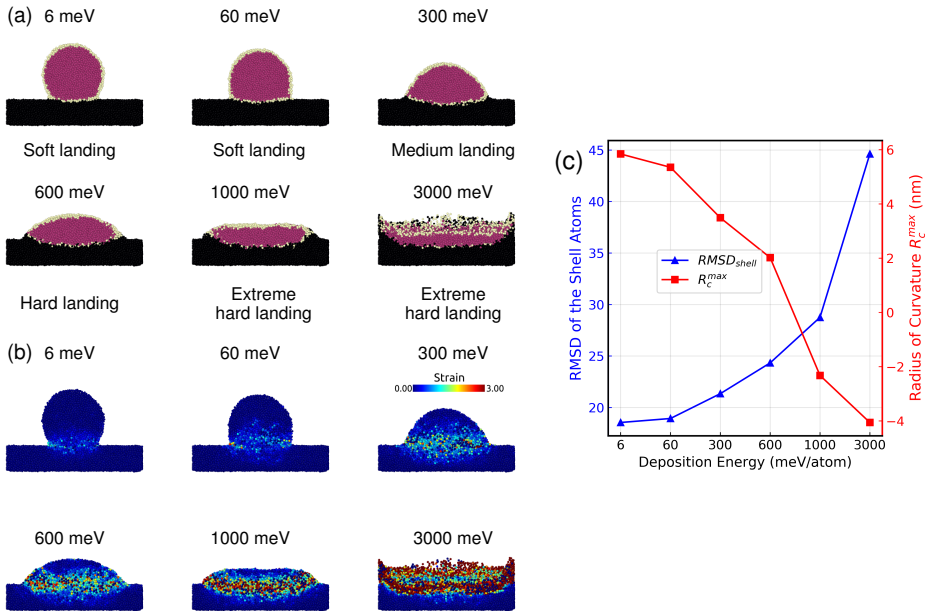
Figure 6.3.: 7 nm Cu$_{50}$Zr$_{50}$ single nanoparticle deposition: The cross sections of the as-deposited states of the nanoparticle being deposited at varying energies (per atom) colour coded by (a) the core and shell regions of undeposited nanoparticle, like in Figure 5.1. (b) The local atomic shear strains of the nanoparticle and substrate, as compared to their pre-deposition states. In (c), the as deposited states are characterized by R_C^{max} and RMSD$_{shell}$ (See text for more details).

be studied in detail. However, to simulate high impact and high momentum depositions, hybrid substrate models using molecular dynamics (MD) and continuum mechanics would serve as better physical models, for instance, by reducing the shockwave reflections upon impact [157, 158].

When the atoms in the simulated cross-sections are colour-coded by their local von Mises strain as in Figure 6.3b, the deformation of the 7 nm nanoparticle is clearly visible. The deformed zones in the nanoparticle-substrate system are much wider than in the 3 nm

cluster case, hinting that the cluster-cluster interfaces in CAMGs would increase in width with the size of the chosen clusters.

In Chapter 4, two quantities R_C^{max} and RMSD_{shell} were defined to quantify the deposited states of a single 3 nm cluster, 2 ns after deposition. Figure 6.3c shows the R_C^{max} and RMSD_{shell} corresponding the depositions of the 7 nm nanoparticle. Unsurprisingly, the RMSD_{shell} is seen to increase drastically with impact energy. At an impact energy of 600 meV/atom, a ~6% increase in RMSD_{shell} relative to the 6 meV/atom soft-landed state. In contrast, for a 3 nm cluster at the same impact energy, the relative increase in RMSD_{shell} from the 6 meV/atom soft-landed state is only ~1.9%. Correspondingly, the convexity of the nanoparticle, characterized by R_C^{max}, is seen to change with deposition energy. In the energy ranges of 0-600 meV/atom, the nanoparticle remains largely convex in nature on the substrate. In comparison, the 3 nm cluster loses its convexity already at 600 meV/atom impact energy (Figure 5.1). At 1000 meV/atom, the 7 nm nanoparticle is more concave, indicating that the nanoparticle begins to embed into the substrate beyond this energy. The CAMG of the 3000 meV/atom case—as mentioned before—was observed to be losing atoms likely due to shockwave reflections. If the snapshots were made later in time, more atoms would have been lost from the deposited nanoparticle at the 3000 meV/atom energy. The R_C^{max} and RMSD_{shell} values in this case are hence merely representative, and will not describe the end state of the deposited nanoparticle. To facilitate a comparison with the 3 nm CAMGs studied in Chapter 5, CAMGs made from 7 nm nanoparticles are simulated with 60, 300 and 600 meV/atom impact energies in the next section.

6.1.2. 7 nm $Cu_{50}Zr_{50}$ Multiple Nanoparticle Deposition

The deposition of the CAMG film was made in an hexagonal close-packed (HCP) pattern (see Section 4 for more details regarding this choice). To fit the deposited CAMG exactly onto the substrate, the substrate dimensions were chosen to be 14 nm × 13 nm in the XY-plane. This helped save simulation costs. In Figure 6.4, the deposited film for the low energy case of 60 meV/atom is shown. Like the 3 nm clusters, all the nanoparticles retain most of their sphericity. In Figure 6.4a, the film atoms are once again colour-coded with the scheme used in Chapters 4 and 5. While the substrate atoms are coloured-black, the atoms in the shell region of the undeposited nanoparticle are coloured yellow, the core atoms are coloured magneta. These core and shell atoms defined from the undeposited nanoparticle are once again used to define the core and interface atoms in the CAMGs films.

A surface mesh construction [137, 139] with a probe sphere radius of 3 Å revealed the formation of pores in the films (Figure 6.4b). Even when the deposition of the
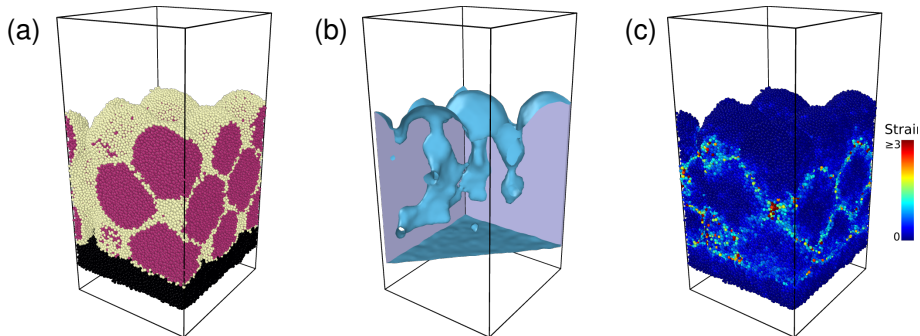
Figure 6.4.: **A perspective view of the 60 meV/atom 7 nm Cu$_{50}$Zr$_{50}$ CAMG**: (a) The deposited film atoms are coloured by a core-shell colour scheme also used in Figures 4.8 and 5.3. (b) A sliced view of a constructed surface mesh in the same perspective view as Figure 6.4a shows the presence of pores in the CAMG film. In (c) the atoms shown in Figure6.4a are represented by their local atomic strains, corroborating the presence of interface regions (similar to Figure 5.3).

nanoparticles were adjusted (deviating from the HCP pattern), the pores were seen to not fully close up. This can be attributed to the large size of the nanoparticles. In atomic clusters of smaller sizes, voids formed in cluster-cluster interfaces can easily be closed up in a HCP deposition.

The local shear strain or von Mises strain of the CAMG atoms and the substrate are depicted by a colour coding scheme in Figure 6.4c. In this manner, the deformed interfaces can be clearly visible, as observed in Figures 5.3 and 6.3.

6.1.3. Effect of Cluster Size on CAMG SRO and Energetic States

After setting up a deposition protocol for the 7 nm nanoparticle, it is now possible to proceed to the evaluation of size effects in the 7 nm CAMGs, which were prepared at three energies of 60, 300 and 600 meV/atom. With the exception of the 60 meV/atom CAMG, the other two simulated samples were observed to not show any pores. To avoid the inclusion of any surface artefacts in the non-porous films (See Section 5.2 for more details), representative slabs were constructed for the CAMGs.
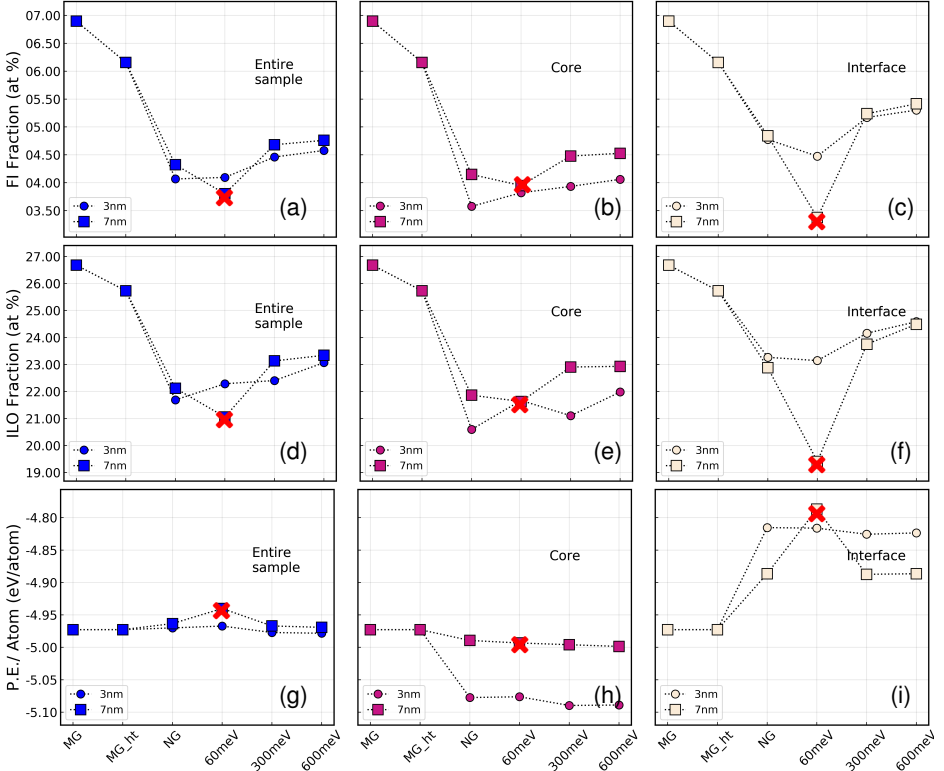
Figure 6.5.: Comparison of SRO and energetic states of 3 nm and 7 nm CAMGs: (a)-(c) Full-icosahedral (FI) packing, (d)-(f) icosahedral-like ordering (ILO), and (g)-(i) average P.E/atom of the CAMGs.

The 7 nm CAMGs are compared to the 3 nm CAMGs based on their energetic states and local short-range order (SRO) in Figure 6.5. The RQ MG and heat-treated Metallic Glass (MG_ht), like in Sections 5.3 and 5.5 are also represented as a reference. For reasons elucidated in Section 5.2, the CAMGs are compared with 7 nm NGs (compacted in an HCP layout), RQ MG, and MG_ht. The porous 7 nm 60 meV/atom CAMG, which is present with surface artefacts is marked in all the sub-figures with a red cross ('✖'). The full-icosahedral (FI) order and icosahedral-like order (ILO) are used to describe the SRO. Figures 6.5(a)-(c) show the FI variation in the entire CAMG representative slab, and also

| Cluster | Composition | | |
diameter	Total sample	Core	Interface
3 nm	$Cu_{50}Zr_{50}$	$Cu_{46}Zr_{54}$	$Cu_{55}Zr_{45}$
7 nm	$Cu_{50}Zr_{50}$	$Cu_{49}Zr_{51}$	$Cu_{52}Zr_{48}$

Table 6.1.: Chemical heterogeneity in the 3 nm and 7 nm CAMGs: The cores and interfaces are in the two CAMGs are found to exhibit distinct chemical concentrations, although the macroscopic chemical composition remains constant at $Cu_{50}Zr_{50}$.

in the core and the interface regions. Likewise, the ILO is depicted in Figures 6.5(d)-(f). It is clearly observed for both the 3 nm and 7 nm CAMGs that the FI order and ILO both increase in the core and interfaces with increasing deposition energy.

In the core regions, a clear difference is seen in the SRO with cluster size. For the case of the CAMG with the larger nanoparticle, the FI order and ILO are both higher than for the 3 nm CAMG of the corresponding deposition energies. This same trend is also observed in the NGs. The average P.E/atom of the CAMGs of different cluster sizes show the opposite behaviour in Figure 6.5(g)-(i). The change in the FI order and ILO in both the 3 nm and 7 nm CAMGs is a clear evidence of tailoring of local structure with the deposition energy. The variation in SRO and P.E/atom between the 3 nm and 7 nm CAMGs can be correlated to the difference in local compositions, as indicated in Table 6.1. In the entire CAMG samples overall, the SRO and P.E/atom are seen to be invariant with cluster size. The observed change in the formation of interfaces and previous reports of scaling of elastic properties with the size of the cluster in nanoglasses [93] motivates the exploration of CAMGs with atomic clusters of 10-30 atoms in size, wherein the scope of interface formation improves drastically.

6.1.4. Small-cluster CAMGs

One of the objectives of this work was to explore the effects of CAMGs made from clusters of 1 nm diameter. Based on previous works on PVD glasses [155, 156], these CAMGs can be expected to show thermodynamic ultrastability. Since the 1 nm clusters contain only ∼30 atoms, the stability of the cluster on the surface after deposition is of concern. Theoretically, after deposition, it is expected that a certain amount of the impact energy dissipated from the cluster is transferred back to it. However, the cluster will be stable on the substrate as long as the energy transferred back to it is lesser than the cohesive energy (E_{coh}) of the material. Even in an extreme case where 100% of the deposition energy is transferred back to the cluster, the depositions in the energy range

of 60-600 meV/atom should result in stable clusters, as the energy is much lower than $\sim$-4.88 eV/atom—the E_{coh} of a $Cu_{50}Zr_{50}$ RQ MG [159]. The following paragraph briefly describes the initial simulations of CAMGs made from small clusters performed with the assistance of Ms. Veronika Stangier, who briefly worked as a student researcher in the group of Prof. Wolfgang Wenzel at the Karlsruhe Institute of Technology (KIT).

In conjunction with the work discussed in this dissertation, attempts to simulate $Cu_{50}Zr_{50}$ CAMGs from clusters of 20-30 atoms were also made to explore local chemical heterogeneity at the size scale of ≤ 1 nm, as envisioned by Kartouzian et al. [29]. In contrary to the expectations elucidated above, the clusters were found to spontaneously melt onto the surface, even with soft landing of 6 meV/atom energy. Alternatively, clusters which were first arranged on the substrate in a 'frozen' state (with their thermal models and net computed forces set to zero)–were also found to dissolve onto the surface once they were unfrozen. This led to conclusion that the dissolution of clusters is likely due to their cohesion with the $Cu_{50}Zr_{50}$ substrate.

As a workaround to these modeling limitations with small clusters in CAMGs, the grain size effects were explored in NGs, as discussed in the following section.

6.2. Size-effects in Nanoglasses

In this section, the influence of grain size or cluster size on the NGs is studied. Firstly, the clusters of diameters 1, 2, 3, 5, and 7 nm were once again prepared as discussed in Chapter 4 and in the above sectin. It was also ensured that the clusters were made with an exact $Cu_{50}Zr_{50}$ composition, with no deviation in composition. The NGs were then made from monodisperse cluster distributions, inserted into a simulation box in a random fashion[4] and compacted at 5 GPa pressure before unloading (See Figure 6.6a).

6.2.1. Variation of Interfaces with Cluster Size

Figures 6.6(b)-(f) show the cross-sectional views of the NGs. Similar to Figure 5.3(d), here the atoms are colour-coded with their local von-Mises strain (η) or atomic strain values evaluated using open visualisation tool (OVITO) [139] to distinguish the interfaces from the core by means of atomic-level deformation. As mentioned in Section 5.2, this is done because the interfacial atoms are expected to deviate more from their original

---

[4]In this section, all NGs are made from a random cluster-insertion model unlike the HCP packing used in previous sections and chapters. Without the constraint of a patterned arrangement, the total number of clusters in the box can be controlled to ensure that the simulated NG samples made from varying cluster sizes have approximately the same number of atoms, thereby ruling out any possible simulation-box size effects.
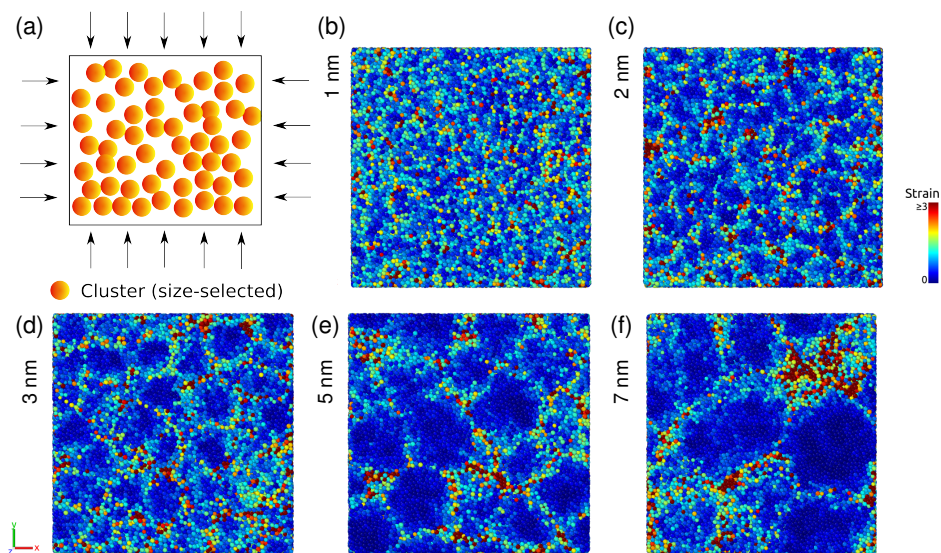
Figure 6.6.: NG interfaces vary with cluster size: (a) The cluster compaction model is illustrated. (b)-(f) A frontal sliced view of the NGs, with the atoms coloured by their von Mises shear strain made from clusters of sizes 1-7 nm shows the homogenization of interface regions with reducing cluster size.

positions near the surface of the uncompressed cluster/nanoparticle, than the core atoms [84]. With the decreasing cluster size, the interfacial width is not only found to drop, but also simultaneously one can visually observe how the interfacial atoms begin to dominate the bulk of the NGs with smaller clusters. This is in agreement with previous NG simulations [93] and also the expectation that smaller clusters have a higher surface to volume ratio, thereby enabling the possibility for more interfaces to occur. In other words, the net number of atoms participating in interface formation increase with decreasing cluster size.

6.2.2. Atomic Readjustment upon Compaction

In the previous subsection, the formation of interfaces in NGs was observed using the local atomic strain or von-Mises strain (η). The change in interfacial characteristics was visually noticeable when the NG building blocks were varied from large nanoparticles (5-7 nm) to small clusters (1-3 nm). The von-Mises strain-information of every atom in the NGs are now used to further explore the cluster-size effects on the atomic displacement which occurs during formation of the cluster-cluster interfaces.
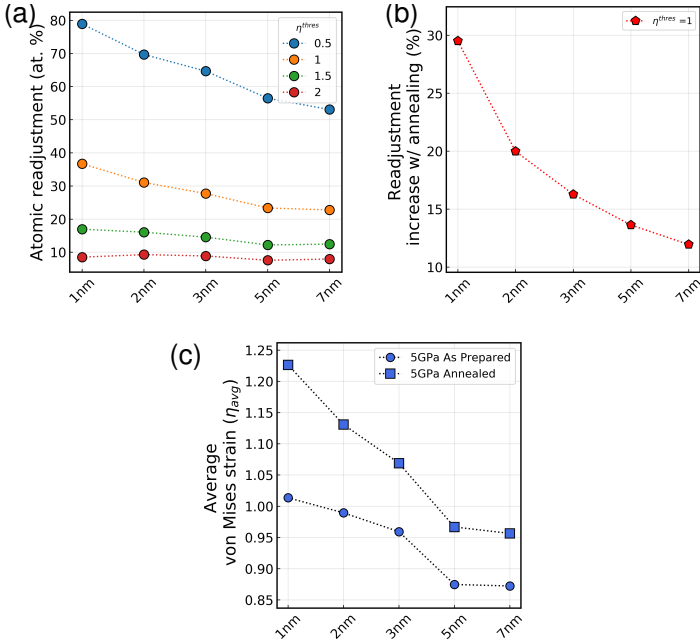
Figure 6.7.: **NG atomic readjustment after compaction**: (a) The fraction of atoms with a local strain higher than a threshold of η^{thres} (indicated in the legend). (b) Atoms with $\eta^{thres} = 1$ are seen to readjust further with annealing, and with decrease in cluster size. (c) The average strain of NG atoms increases with annealing and with lowering cluster size.

In Figure 6.7a, the 'Atomic readjustment' in the compacted NGs—defined as the percentage of atoms having η above a threshold of η^{thres} is illustrated. The atomic

readjustment is named so, as the von Mises strain essentially captures the change of the local environment of around an atom in a system of atoms, with respect to a reference configuration [20, 21, 97, 143]. In this manner, one can quantify the change in the environment of each atom in a cluster before and after compaction into a NG. At low thresholds of $\eta^{thres} \leq 1$, the atomic readjustment in the NGs is seen to increase with decreasing cluster size. It is also noticed that above $\eta^{thres} = 1$, the atomic readjustment does not vary with cluster size.

Both these observations together indicate that the number of highly readjusting interfacial atoms in the NGs do not vary significantly with cluster size. More number of atoms participate in the atomic-level deformation in the smaller cluster NGs, overall. This is also confirmed by Figures 6.7(b)-(c). Additionally, the NG samples were annealed below T_g at 600 K for 2 ns. The heating from 50 K to 600 K was done at a rate of 10^{12} K/s. After equilibration at 600 K for 2 ns, the samples were cooled down back to 50 K at a rate of 10^{12} K/s and equilibrated again for 2 ns. Upon annealing, the increase in atomic readjustment (at a constant threshold of $\eta^{thres} = 1$) is greater with the decrease of NG cluster size. Additionally, the average von Mises strain in the as-prepared NG system is higher with reduction of cluster size, and the increase in this value upon annealing is also higher at smaller cluster sizes.

6.2.3. Short-range Order and Thermal Behaviour of the NGs

The as-prepared and annealed NGs are next characterized by their local SRO and energetic states. In Figure 6.8, the characteristics of the entire NG samples are depicted. The core and interface atoms are not individually investigated. The FI order, ILO, and P.E/atom in the as-prepared samples are noted to vary slightly with the cluster size. However, in proportion to the effect of quench rates or energetic deposition as seen in Figures 5.13 and 6.5, respectively, the SRO and energetic states are fail to show the expected cluster size dependency.

Upon thermal relaxation after annealing, the modelled NG samples are observed to have an increased SRO and a lowered energetic state in comparison to their as-prepared states. This appears to be a consequence of the atomic readjustment that was noted to be promoted by the annealing process in the previous subsection. The annealing possibly assists the simulated NGs to attain their final states, which may not be accessible by the as-prepared samples due the short MD simulation time scales. However, even after the thermal treatment, no discernible variation of the SRO and energetic features with cluster size can be noted. This study on $Cu_{50}Zr_{50}$ NGs is in agreement with previous works on $Cu_{64}Zr_{36}$ NGs [93].
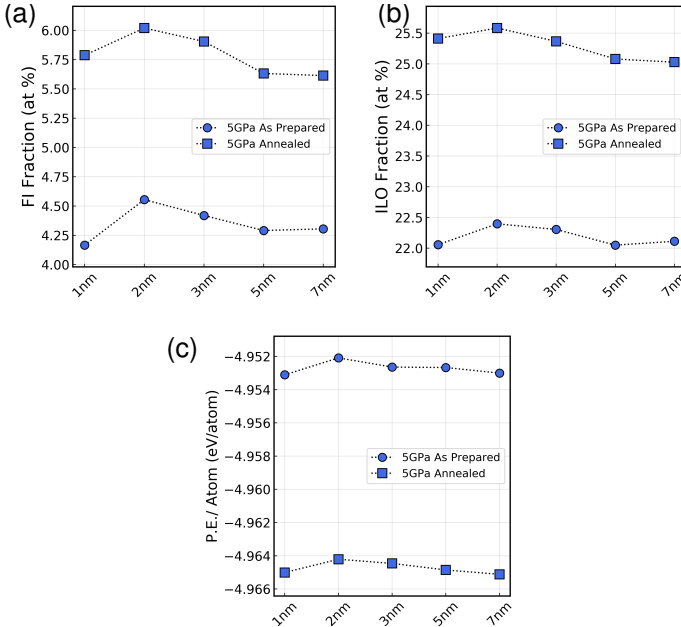
Figure 6.8.: Influence of cluster size on structural and energetic states of NGs: (a) FI-ordering (b) ILO (c) P.E/atom states of the various as-prepared and annealed NGs.

The preceding research activity on cluster-size influence in the NGs, although demonstrating an invariance of local order with cluster-size, reported some interesting mechanical properties in the $Cu_{36}Zr_{64}$, $Cu_{50}Zr_{50}$ and $Cu_{64}Zr_{36}$ Voronoi-tesselated NGs [94, 154] and cluster-compacted NGs [93]. Additionally, the mechanical and thermal properties of RQ MGs have been linked in earlier works [160–162]. This motivates the need to explore the thermal properties of the NGs, in which the reduced grain/cluster-size has notably demonstrated a reduction of flow stress and increased plasticity.

The simulated NGs of various cluster sizes were subjected to a heat-treatment at zero pressure from a low temperature to well above the T_g (800 K for simulated $Cu_{50}Zr_{50}$ RQ MGs), and compared with a reference system of RQ MGs. The average atomic enthalpy[5] as a function of temperature is represented for both the NGs and the reference $Cu_{50}Zr_{50}$

---

[5]The enthalpy H = U + p·V, where U, p, and V are the internal energy, pressure and volume of the system, respectively. In the heating simulations, as p=0, the enthalpy can be expressed as H = U.
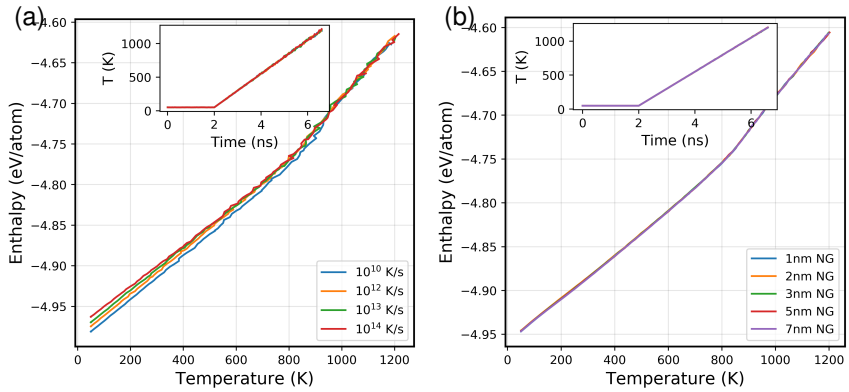
Figure 6.9.: Thermal behaviour of MGs and NGs: The average enthalpy per atom with increasing temperature in (a) the simulated reference samples of 8000-atom sized $Cu_{50}Zr_{50}$ RQ MGs of varying quench rates and (b) the NGs of varying cluster sizes. In the insets of the respective figures, the system temperature with time is indicated.

RQ MGs[6] in Figure 6.9. The NG samples, in their as-prepared states at 50 K are first equilibrated for 2 ns and then heated to 1200 K at a rate of 0.25 K/ps. For the reference RQ MGs prepared at various quench rates, the initial average enthalpies at 50 K are found to be ordered according to quench rates associated with their formation: the lower the quench rate, the lower the enthalpy. This trend continues in the entire temperature regime below T_g, after which the enthalpies of the glasses of various quench rates are equal. These observations are in agreement with known knowledge from literature [5, 37]. In contrast, the thermal behaviour of the NGs is found to be independent of cluster-size. The curves depicting average enthalpy versus temperature for various cluster-sizes overlap with each other.

6.3. Discussion and Summary

The ability to design a network of distinct amorphous cluster-core and cluster-cluster interface phases into the CAMGs and NGs begets the emergence of cluster-size/grain size

---

[6]Further studies to establish the protocol for heating and cooling of RQ MGs are discussed in Section A.3 of the Supplementary Material chapter.

effects in these novel amorphous materials. In the current chapter, simulated $Cu_{50}Zr_{50}$ CAMGs and NGs prepared from monodisperse clusters of varying sizes were studied.

First, the CAMGs made from a 3 nm cluster in Chapter 5 was compared to those prepared from a 7 nm nanoparticle at corresponding per-atom deposition energies. The SRO of the 7 nm CAMGs were also observed to be tailorable with deposition energy in the samples. However, the SRO and the average potential energy (PE)/atom of CAMGs (for a given deposition energy) were found to be invariant with the cluster-size. Upon further inspection, it was revealed that within the core and interfacial regions, the SRO and the average energetic states in the CAMGs varied considerably with cluster size. These effects were attributed to the difference in the local chemical heterogeneity introduced into the simulated CAMGs from the precursor clusters. An attempt to prepare CAMGs from clusters of 1 nm diameter ($\sim$30 atoms) proved to be non-viable, owing to spontaneous melting of deposited clusters onto the substrate even at per-atom deposition energies below the cohesive energy of $Cu_{50}Zr_{50}$. Replacing the $Cu_{50}Zr_{50}$ substrate with a Si substrate may reduce cluster-substrate cohesion, promoting retention of the structure of the smaller clusters after deposition.

The influence of grain size studies in smaller clusters (diameter $\leq$ 2 nm) were explored in the $Cu_{50}Zr_{50}$ NGs made using a monodisperse clusters inserted randomly before compaction. This approach offers the advantage of exploring size effects without considering additional substrate interactions unlike in the CAMGs. With the reduction of the cluster size in the NGs, the interfacial width was seen to correspondingly reduce, while the cluster atoms participating in readjustment upon compaction and annealing increase drastically. Despite the readjustment of the interfacial atoms, and the opportunity for interfaces to relax better, no significant change is seen in the NGs with the cluster size. Additionally, the smaller 1-2 nm clusters present a challenge of defining interfaces in the NGs, in terms of distinguishing the shell atoms from the core. In the future, using the von Mises strain or the quasi-nearest atom (QNA) approach [163] may serve as better parameters to identify glass-glass interfaces by making no *a priori* inferences about the clusters' core and shell regions. Further studies on the evolution of density and free volume with the composition and size of the precursor clusters are in progress.

7. Conclusions

7.1. Summary

In this dissertation the novel $Cu_{50}Zr_{50}$ cluster-assembled metallic glass (CAMG), prepared by the energetic deposition of amorphous nanoclusters, has been studied by means of molecular dynamics (MD) simulations. The cluster assembly is expected to give rise to new amorphous structures different from the conventional rapidly-quenched (RQ) metallic glass (MG) of the same composition. The CAMG structure is also expected to be different from the nanoglass (NG) produced by mechanical compaction of amorphous clusters. Understanding the formation mechanisms and final structures of the so-obtained CAMG opens up possibilities to design and control amorphous structures. The key results obtained in this doctoral work are summarized below.

1. **First virtual insights into CAMGs**

   a) **Development of a simulation protocol for cluster deposition**
   First, a single 3 nm cluster is derived from the bulk of a RQ MG and followed with a heat-treatment to induce a structure that is expected from experimental inert-gas condensation (IGC) preparation. This cluster was deposited at various impact energies ranging from 6-6000 meV/atom onto a $Cu_{50}Zr_{50}$ substrate. Its shape and deviation from its undeposited state were noted to change with impact energy. At low energies (6-60 meV/atom) the cluster adopted a nearly spherical morphology, while at medium impact energy of 300 meV/atom the cluster is disorted further although still adopting a convex drop-like shape. At deposition energies higher than 600 meV/atom the cluster begins to turn concave-like, embedding itself more into the substrate. The cluster core-shell structure disintegrates in the extreme landing (6000 meV/atom energy) case.

   b) **Simulating $Cu_{50}Zr_{50}$ CAMGs**
   The protocol developed for cluster deposition was extended to simulate CAMGs. It was chosen to deposit 3 nm size $Cu_{50}Zr_{50}$ clusters in a hexagonal close-packed (HCP) pattern to remove surface artefacts, maximize cluster-cluster interface formation, and improve simulation efficiency. Upon assembling the CAMGs from

the 3 nm sized clusters, it was found that the chemically segregated core and shell structure of the undeposited clusters gave rise to two chemically distinct Zr-rich cores and Cu-rich interfaces phases; with the core regions being embedded within an interconnected network of the cluster-cluster interfaces. The interfaces were found to be stable in MD timescales for impact energies up to 600 meV/atom, however they disappear at extreme landing energy of 6000 meV/atom energy.

c) **Short-to-medium range order tailoring in $Cu_{50}Zr_{50}$ CAMGs**

The full-icosahedral (FI) and icosahedral-like order (ILO) evaluated by Voronoi tessellation were used to describe the short-range order (SRO) of the glasses. Strings of FI-atoms are used to indicate medium-range order (MRO). The SRO of the NG and CAMG are found to differ from the RQ MGs, irrespective of the quench rate associated with the bulk-derived clusters. In the conventional (10^{10} K/s quench rate) case, SRO is lower in the NG and CAMG as compared to RQ MGs, for both the cores and interfaces. However, irrespective of the quench rate used, both the SRO and MRO in CAMGs recover towards the metallic glass values with increasing impact energies. As a result, adjusting the processing conditions in CAMGs makes it possible to control the local structure of metallic glasses.

2. **Cluster-size effects in CAMGs and NGs**

An influence of cluster size on the interface and cores regions was expected, motivating an investigation of further changes within the CAMG structure.

a) **Cluster deposition: 3 nm cluster vs 7 nm $Cu_{50}Zr_{50}$ nanoparticle**

Large 7 nm sized $Cu_{50}Zr_{50}$ nanoparticles were derived from the bulk, in an identical procedure as for the 3 nm clusters. The 7 nm nanoparticles also showed a core-shell structure, with a shell of 0.3 nm thickness. The Cu-enrichment in the nanoparticle shell was 52 %, which is 4% lesser than in the 3 nm cluster. Upon testing the single nanoparticle deposition, the 7 nm nanoparticle was found to retain its morphology better at any given impact energy as compared to the 3 nm cluster. Like in the 3 nm cluster case, the shell atoms of the 7 nm nanoparticles were also found to deviate from their original positions, characterized by the local atomic strain. The amount of deviation was higher at any given energy for the 7 nm nanoparticle. At the deposition site, the atoms were found to increasingly shear (with respect to their un-deposited states) with deposition energy. At a given energy, the larger 7 nm nanoparticle was found to cause larger volume of atomic-level deformation at the site of deposition, hinting at formation of larger interfaces during the cluster-ion beam deposition (CIBD) process.

b) **Local order in 7 nm $Cu_{50}Zr_{50}$ CAMGs**

Like the 3 nm CAMGs, the CAMGs from 7 nm nanoparticles were also deposited

in a HCP pattern. As expected from the single cluster deposition, the interfacial width was larger, and at 60 meV/atom energy, the nanoparticles could not deform enough, leaving large pores in the sample. However, at higher energies, the pores closed up and the SRO of the 7 nm CAMGs increased with deposition energy. At a fixed impact energy, the SRO and the average energetic states of CAMGs were found to be invariant with the cluster-size. The difference in the local chemical heterogeneity introduced from the precursor clusters into the simulated CAMGs, brought about a significant variation in the SRO and the average P.E./atom within the core and interfacial regions with cluster size.

c) **Building NGs with blocks ranging from atomic clusters to large nanoparticles**
Monodisperse clusters of diameters ranging between 1-7 nm were arranged randomly before compaction to prepare $Cu_{50}Zr_{50}$ NGs. Lowering the cluster size was observed to lower the interfacial width as in the CAMGs. The number of cluster atoms participating in readjustment at the interfaces upon compaction and annealing was also found to increase with decreasing cluster sizes. The change in cluster size appears to not have a significant influence on the SRO, average energetic states, and the thermal behaviour in the simulated NGs. Regardless, the pronounced increase in readjustment of the interfacial atoms with reduced cluster size offers scope for interesting local structural changes which may have not been detected in the present simulations. A deeper investigation is required to better understand these novel glasses.

The establishment of an MD simulation protocol for CAMGs and the study of their local characteristics now lends support to the idea of controllable local order and microstructures in metallic glasses. There is an immense need for future work on this class of novel materials to better understand them and harness their properties.

7.2. Outlook

The primary contributions of this work are the initial *in silico* investigations on the cluster-assembly of metallic glasses, as discussed above. Although some preliminary questions have been answered, the quest to fully understand CAMGs and the consequences of their tailorability of their local order remains to be explored.

1. **Thermal stability of CAMGs made from vapour-condensed clusters**
   In a previous study, Danilov et al. [98] reported the thermal ultrastability of NGs from IGC-derived nanoparticles, as compared to NGs from bulk-derived nanoparticles, also also conventional RQ MGs. This remains to be explored in CAMGs. The IGC-like vapour condensed cluster growth method described in Chapter 4 can be combined with gas-phase condensation methods [89, 96] to prepare spherical $Cu_{50}Zr_{50}$ clusters. It was also determined in the current work, that the cluster assembly of amorphous nanoclusters leads to the increase of local SRO with impact energy. The stability gained from the use of IGC-derived nanoparticles as building blocks, compounded with the increase in SRO with the deposition energy can result in a synergetic effect to form thermally ultrastable CAMGs.

2. **Isolating the role of cluster-deposition processing in CAMGs**
   In the present thesis, a heat-treatment was given to the clusters to allow the cluster-atoms to diffuse, enabling a chemical segregation. The phenomena observed in CAMGs, discussed in Chapters 4, 5 and 6 are a result of the deposition process and also the chemical segregation. A comparison of CAMGs made from unsegregated clusters can help isolate the role of the deposition processing. Moreover, the difference in local packing and density in comparison to the segregated interfaces and unsegregated interfaces can lead to interesting changes in properties of CAMGs.

3. **Novel mechanical properties of CAMGs**
   The tailorable local structure of the CAMGs may result in exciting properties. Previously, reducing the cluster size of NGs, has been shown to reduce flow stress [93, 94] of the material. This change in property was driven by the reduction of interface width and simultaneous increase of interface volume—the nature of the interface plays an important influence on the mechanical properties of bottom-up glasses. Consequently, comparing the mechanical properties of CAMGs made from unsegregated and vapour condensed clusters via nanoindentation studies, specifically observing the stress-strain relations, and strain localization and propagation in the two kinds of CAMG interfaces would be interesting.

4. **CAMG simulations at mesoscopic timescales**
   A challenge encountered in this dissertation was the formation of large pores in the

CAMGs when the clusters were deposited randomly (discussed in Chapter 4). It is very possible that the clusters at long experimental times scales, may reach their preferred states which result in the pores closing up. The short simulation times achieved by MD thereby hinder the exact replication of CAMG experiments. A recent technique called the autonomous basin climbing (ABC) has been developed to traverse the potential-energy landscape (PEL) to general atomic trajectories in the timescale of seconds [164, 165]. This basin-hopping method finds immense value in CAMG simulations to access mesoscopic timescales and better model the experiments.

5. **Investigating crystalline cluster-assembled materials (CAMs)**
Recently, polycrystalline materials of small nm-sized grains have been shown to exhibit minimal-interface configurations, exhibiting higher strengths and thermal stability [166, 167] in contrast to the expected inverse Hall-Petch (IHP) behaviour. The simulation protocols developed within the framework of this thesis are already being applied to simulate CAMs from nm-sized crystalline clusters in the group of Prof. Penghui Cao, University of California-Irvine, to test the IHP relationship with cluster-assembly.

6. **Controlling chemical heterogeneity in CAMGs**
As mentioned in the Scientific Background chapter, one of the first works on CAMGs reported a new amorphous class of materials built from chemically distinct clusters 10-16 atoms in size, in an attempt to engineer a locally heterogenous structure in MGs [28, 29]. Such exotic CAMGs have not been investigated beyond synchrotron surface x-ray diffraction (XRD) measurements. In Chapter 6, the possibility of simulating locally heterogenous clusters is briefly discussed. In the present thesis, the simulation of CuZr clusters of varying compositions with $\sim$30 atoms each were not stable upon deposition despite the impact energies being much lower than the cohesive energy of the glassy solid. Presently, the dissolution of the small clusters is attributed to the cohesive forces from the $Cu_{50}Zr_{50}$ substrate used, and hence using a Si substrate may offer more success. The CAMGs of a given macroscopic composition may then be simulated at soft-landing energies with varying local heterogeneity. The resulting systems could be investigated by their local SRO and MRO, but also by the phonon density of states, which is sensitive to the local atomic structure.

Bibliography

[1] W. Klement, R. H. Willens, P. Duwez, *Nature* **1960**, *187*, 869–870 (pages 1, 7).

[2] A. L. Greer, *Science (80-.)*. **1995**, *267*, 1947–1953 (pages 1, 10).

[3] C. Suryanarayana, *Prog. Mater. Sci.* **2001**, *46*, 1–184 (pages 1, 10).

[4] M. M. Trexler, N. N. Thadhani, *Prog. Mater. Sci.* **2010**, *55*, 759–839 (page 1).

[5] L. Berthier, M. D. Ediger, *Phys. Today* **2016**, *69*, 40–46 (pages 1, 7, 8, 11, 45, 46, 48, 50, 100).

[6] W. L. Johnson, *JOM* **2002**, *54*, 40–43 (page 1).

[7] N. T. N. Nu, T. V. Luong, *Int. J. Sci. Environ. Technol.* **2016**, *5*, 2209–2216 (page 1).

[8] A. W. Weeber, H. Bakker, *Phys. B Phys. Condens. Matter* **1988**, *153*, 93–135 (pages 1, 10).

[9] P. Duwez, R. H. Willens, W. Klement, *J. Appl. Phys.* **1960**, *31*, 1136–1137 (pages 1, 7).

[10] J. Jing, A. Krämer, R. Birringer, H. Gleiter, U. Gonser, *J. Non. Cryst. Solids* **1989**, *113*, 167–170 (pages 1, 16, 17, 88).

[11] H. Gleiter, T. Schimmel, H. Hahn, *Nano Today* **2014**, *9*, 17–68 (page 1).

[12] Y. Ivanisenko, C. Kübel, S. H. Nandam, C. Wang, X. Mu, O. Adjaoud, K. Albe, H. Hahn, *Adv. Eng. Mater.* **2018**, *20*, 1800404 (pages 1, 19).

[13] J. X. Fang, U. Vainio, W. Puff, R. Würschum, X. L. Wang, D. Wang, M. Ghafari, F. Jiang, J. Sun, H. Hahn, H. Gleiter, *Nano Lett.* **2012**, *12*, 458–463 (pages 1, 17, 18).

[14] M. Ghafari, H. Hahn, H. Gleiter, Y. Sakurai, M. Itou, S. Kamali, *Appl. Phys. Lett.* **2012**, *101*, DOI `10.1063/1.4769816` (pages 1, 17, 24).

[15] J. Weissmüller, R. Birringer, H. Gleiter, *Key Eng. Mater.* **1992**, *77-78*, 161–170 (pages 1, 17).

[16] H. Gleiter, *Small* **2016**, *12*, 2225–2233 (page 1).

[17] R. Witte, T. Feng, J. X. Fang, A. Fischer, M. Ghafari, R. Kruk, R. A. Brand, D. Wang, H. Hahn, H. Gleiter, *Appl. Phys. Lett.* **2013**, *103*, 073106 (pages 1, 17, 18, 24, 77).

[18] S. H. Nandam, Y. Ivanisenko, R. Schwaiger, Z. Śniadecki, X. Mu, D. Wang, R. Chellali, T. Boll, A. Kilmametov, T. Bergfeldt, H. Gleiter, H. Hahn, *Acta Mater.* **2017**, *136*, 181–189 (pages 1, 3, 18, 88).

[19] D. Şopu, K. Albe, Y. Ritter, H. Gleiter, *Appl. Phys. Lett.* **2009**, *94*, DOI `10.1063/1.3130209` (pages 1, 19–21, 62, 77).

[20] O. Adjaoud, K. Albe, *Acta Mater.* **2018**, *145*, 322–330 (pages 1, 3, 19–21, 52, 62, 63, 65, 85, 88, 98).

[21] B. Cheng, J. R. Trelewicz, *Phys. Rev. Mater.* **2019**, *3*, 1–9 (pages 1, 19, 21, 62, 76, 77, 88, 98, 127).

[22] O. Adjaoud, K. Albe, *Acta Mater.* **2016**, *113*, 284–292 (pages 1, 19, 20, 52–54, 77, 88, 89).

[23] Y. Ritter, D. Sopu, H. Gleiter, K. Albe, *Acta Mater.* **2011**, *59*, 6588–6593 (pages 1, 3, 19, 20, 52, 80).

[24] C. Wang, X. Guo, Y. Ivanisenko, S. Goel, H. Nirschl, H. Gleiter, H. Hahn, *Scr. Mater.* **2017**, *139*, 9–12 (pages 1, 3, 17).

[25] C. Wang, T. Feng, D. Wang, X. Mu, M. Ghafari, R. Witte, A. Kobler, C. Kübel, Y. Ivanisenko, H. Gleiter, H. Hahn, *Mater. Res. Lett.* **2018**, *6*, 178–183 (page 1).

[26] S. H. Nandam, O. Adjaoud, R. Schwaiger, Y. Ivanisenko, M. R. Chellali, D. Wang, K. Albe, H. Hahn, *Acta Mater.* **2020**, *193*, 252–260 (page 1).

[27] S. H. Nandam, R. Schwaiger, A. Kobler, C. Kübel, C. Wang, Y. Ivanisenko, H. Hahn, *J. Mater. Res.* **2021**, *36*, 2903–2914 (page 1).

[28] A. Kartouzian, *Nanoscale Res. Lett.* **2013**, *8*, 2–5 (pages 2, 22, 24, 88, 107).

[29] A. Kartouzian, J. Antonowicz, T. Lünskens, A. Lagogianni, P. Heister, G. Evangelakis, R. Felici, *Mater. Express* **2014**, *4*, 228–234 (pages 2, 22, 24, 53, 88, 95, 107).

[30] C. Benel, A. Fischer, A. Zimina, R. Steininger, R. Kruk, H. Hahn, A. Léon, *Mater. Horizons* **2019**, *6*, 727–732 (pages 2, 3, 24–26, 51, 55, 57, 72, 81, 88).

[31] C. Benel, T. Reisinger, R. Kruk, H. Hahn, *Adv. Mater.* **2019**, *31*, 1806634 (pages 2, 22, 23, 51, 55, 88).

[32] P. G. Debenedetti, F. H. Stillinger, *Nature* **2001**, *410*, 259–267 (pages 7, 11).

[33] Robert H. Doremus, *Glass Science*, Wiley, **1994**, p. 352 (page 7).

[34] G. Jaeger, *Arch. Hist. Exact Sci.* **1998**, *53*, 51–81 (page 8).

[35] M. H. Cohen, D. Turnbull, *J. Chem. Phys.* **1959**, *31*, 1164–1169 (pages 8, 9).

[36] W. Kauzmann, *Chem. Rev.* **1948**, *43*, 219–256 (pages 8, 11).

[37] M. D. Ediger, C. A. Angell, S. R. Nagel, *J. Phys. Chem.* **1996**, *100*, 13200–13212 (pages 9, 50, 100).

[38] H. Nishimori, G. Ortiz, *Elements of Phase Transitions and Critical Phenomena*, Oxford University Press, **2010** (page 9).

[39] T. G. Fox, P. J. Flory, *J. Appl. Phys.* **1950**, *21*, 581–591 (page 9).

[40] P. Ramachandrarao, B. Cantor, R. W. Cahn, *J. Mater. Sci.* **1977**, *12*, 2488–2502 (page 9).

[41] A. J. Batschinski, *Zeitschrift für Phys. Chemie* **1913**, *84U*, 643–706 (page 9).

[42] T. G. Fox, P. J. Flory, *J. Phys. Chem.* **1951**, *55*, 221–234 (page 9).

[43] D. Turnbull, M. H. Cohen, *J. Chem. Phys.* **1961**, *34*, 120–125 (page 10).

[44] R. B. Schwarz, W. L. Johnson, *Phys. Rev. Lett.* **1983**, *51*, 415–418 (page 10).

[45] D. Turnbull, *Contemp. Phys.* **1969**, *10*, 473–488 (page 10).

[46] W. H. Wang, C. Dong, C. H. Shek, *Mater. Sci. Eng. R Reports* **2004**, *44*, 45–89 (pages 10, 11).

[47] C.-y. Wu, K.-j. Lin, Y.-t. Cheng, C.-k. Huang, C.-N. PAN, W.-C. LI, L.-K. CHIANG, C.-N. YEH, S.-C. FONG, *China Steel Tech. Rep.* **2014**, 28–42 (page 10).

[48] W. L. Johnson, *MRS Bull.* **1999**, *24*, 42–56 (page 10).

[49] A. L. Greer, E. Ma, *MRS Bull.* **2007**, *32*, 611–619 (pages 10, 12).

[50] A. Inoue, *Acta Mater.* **2000**, *48*, 279–306 (page 10).

[51] A. R. Berens, I. M. Hodge, *Macromolecules* **1982**, *15*, 756–761 (page 11).

[52] C. A. Angell, K. L. Ngai, G. B. McKenna, P. F. McMillan, S. W. Martin, *J. Appl. Phys.* **2000**, *88*, 3113–3157 (page 11).

[53] F. H. Stillinger, *Science (80-.).* **1995**, *267*, 1935–1939 (page 11).

[54] E. Ma, *Nat. Mater.* **2015**, *14*, 547–552 (pages 12, 15).

[55] P. G. Wolynes, *Proc. Natl. Acad. Sci. U. S. A.* **2009**, *106*, 1353–1358 (page 12).

[56] H. W. Sheng, W. K. Luo, F. M. Alamgir, J. M. Bai, E. Ma, *Nature* **2006**, *439*, 419–425 (pages 12, 14, 15, 27, 43, 80).

[57] T. Fukunaga, K. Itohm, T. Otomo, K. Mori, M. Sugiyama, H. Kato, M. Hasegawa, A. Hirata, Y. Hirotsu, A. C. Hannon, *Intermetallics* **2006**, 893–897 (pages 12, 14, 15).

[58] J. D. Bernal, *Nature* **1959**, *183*, 141–147 (pages 13, 14, 80).

[59] J. L. Finney, *Proc. R. Soc. London. A. Math. Phys. Sci.* **1970**, *319*, 479–493 (page 13).

[60] G. Voronoi, *J. für die reine und Angew. Math. (Crelles Journal)* **1908**, *1908*, 198–287 (page 13).

[61] H. S. M. Coxeter, *Regular Polytopes*, 3rd, Dover Publications, **1973** (pages 13, 36).

[62] G. Lejeune Dirichlet, *J. für die reine und Angew. Math. (Crelles Journal)* **1850**, *1850*, 209–227 (page 13).

[63] B. Delaunay, *Bull. l'Académie des Sci. l'URSS. Cl. des Sci. mathématiques na* **1934**, *1934*, 793–800 (page 13).

[64] C. Kittel, *Introduction to Solid State Physics*, 8th Editio, **2004**, p. 704 (pages 13, 36).

[65] P. H. Gaskell, *Nature* **1978**, *276*, 484–485 (page 13).

[66] M. Chen, *NPG Asia Mater.* **2011**, *3*, 82–90 (page 13).

[67] D. B. Miracle, *Nat. Mater.* **2004**, *3*, 697–702 (pages 13, 14, 80).

[68] D. B. Miracle, *Acta Mater.* **2013**, *61*, 3157–3171 (page 14).

[69] J. D. Honeycutt, H. C. Andersen, *J. Phys. Chem.* **1987**, *91*, 4950–4963 (page 14).

[70] F. C. Frank, *Proc. R. Soc. London. Ser. A. Math. Phys. Sci.* **1952**, *215*, 43–46 (page 14).

[71] A. S. Clarke, H. Jónsson, *Phys. Rev. E* **1993**, *47*, 3975–3984 (page 14).

[72] F. C. Frank, J. S. Kasper, *Acta Crystallogr.* **1958**, *11*, 184–190 (pages 14, 43).

[73] J. P. Doye, D. J. Wales, *J. Phys. B At. Mol. Opt. Phys.* **1996**, *29*, 4859–4894 (page 14).

[74] J. Ding, S. Patinet, M. L. Falk, Y. Cheng, E. Ma, *Proc. Natl. Acad. Sci. U. S. A.* **2014**, *111*, 14052–14056 (pages 14, 43, 44, 83).

[75] J. Ding, Y. Q. Cheng, E. Ma, *Acta Mater.* **2014**, *69*, 343–354 (pages 14, 83).

[76] H. L. Peng, M. Z. Li, W. H. Wang, C. Z. Wang, K. M. Ho, *Appl. Phys. Lett.* **2010**, *96*, 2008–2011 (pages 14, 45, 46, 52).

[77] M. Li, C. Z. Wang, S. G. Hao, M. J. Kramer, K. M. Ho, *Phys. Rev. B - Condens. Matter Mater. Phys.* **2009**, *80*, 1–7 (pages 14, 44, 45).

[78] X. X. Yue, C. T. Liu, S. Y. Pan, A. Inoue, P. K. Liaw, C. Fan, Effect of cooling rate on structures and mechanical behavior of Cu50Zr50 metallic glass: A molecular-dynamics study, **2018** (pages 14, 37, 43–46, 48, 73, 75, 83).

[79] Y. Q. Cheng, H. W. Sheng, E. Ma, *Phys. Rev. B - Condens. Matter Mater. Phys.* **2008**, *78*, 1–7 (pages 14, 27, 51, 83).

[80] M. Lee, C. M. Lee, K. R. Lee, E. Ma, J. C. Lee, *Acta Mater.* **2011**, *59*, 159–170 (pages 15, 80).

[81] Y. Ritter, K. Albe, *J. Appl. Phys.* **2012**, *111*, 103527 (page 15).

[82] Y. Ritter, PhD thesis, Technical University of Darmstadt, **2012** (pages 15, 45).

[83] J. L. Finney, *Nature* **1977**, *266*, 309–314 (page 15).

[84] H. Gleiter, *J. Appl. Crystallogr.* **1991**, *24*, 79–90 (pages 15, 16, 71, 96).

[85] H. Gleiter, *Nanostructured Mater.* **1995**, *6*, 3–14 (page 16).

[86] M. Ghafari, S. Kohara, H. Hahn, H. Gleiter, T. Feng, R. Witte, S. Kamali, *Appl. Phys. Lett.* **2012**, *100*, 2–6 (page 17).

[87] C. Wang, D. Wang, X. Mu, S. Goel, T. Feng, Y. Ivanisenko, H. Hahn, H. Gleiter, *Mater. Lett.* **2016**, *181*, 248–252 (pages 17, 53).

[88] S. H. Nandam, PhD thesis, Technical University of Darmstadt, **2018** (page 18).

[89] P. Krasnochtchekov, K. Albe, R. S. Averback, *Zeitschrift Fur Met.* **2003**, *94*, 1098–1105 (pages 19, 20, 51, 106).

[90] O. Adjaoud, K. Albe, *Acta Mater.* **2019**, *168*, 393–400 (pages 19, 21, 75).

[91] O. Adjaoud, K. Albe, *Front. Mater.* **2020**, *7*, 1–10 (page 19).

[92] C. Kalcher, O. Adjaoud, J. Rohrer, A. Stukowski, K. Albe, *Scr. Mater.* **2017**, *141*, 115–119 (pages 19, 62, 88).

[93] B. Cheng, J. R. Trelewicz, *J. Mater. Res.* **2019**, *34*, 2325–2336 (pages 19, 21, 62, 87, 94, 96, 98, 99, 106).

[94] S. Adibi, P. S. Branicio, Y. W. Zhang, S. P. Joshi, *J. Appl. Phys.* **2014**, *116*, DOI `10.1063/1.4891450` (pages 19, 21, 44, 87, 99, 106).

[95] Z. D. Sha, P. S. Branicio, H. P. Lee, T. E. Tay, *Int. J. Plast.* **2017**, *90*, 231–241 (pages 19, 21).

[96] K. Zheng, P. Branicio, *Phys. Rev. Mater.* **2020**, *4*, 1–7 (pages 19, 20, 106).

[97] K. Zheng, S. Yuan, H. Hahn, P. S. Branicio, *Sci. Rep.* **2021**, *11*, 1–11 (pages 19, 21, 62, 98).

[98] D. Danilov, H. Hahn, H. Gleiter, W. Wenzel, *ACS Nano* **2016**, *10*, 3241–3247 (pages 20, 29, 51, 106).

[99] W. Kob, H. C. Andersen, *Phys. Rev. E* **1995**, *52*, 4134–4153 (pages 20, 29).

[100] M. I. Mendelev, M. J. Kramer, R. T. Ott, D. J. Sordelet, D. Yagodin, P. Popel, *Philos. Mag.* **2009**, *89*, 967–987 (pages 21, 29, 51).

[101] M. I. Mendelev, Y. Sun, F. Zhang, C. Z. Wang, K. M. Ho, *J. Chem. Phys.* **2019**, *151*, DOI `10.1063/1.5131500` (pages 21, 29, 30, 43, 50).

[102] F. Shimizu, S. Ogata, J. Li, *Mater. Trans.* **2007**, *48*, 2923–2927 (pages 21, 38).

[103] J. L. Ma, H. Y. Song, J. Y. Wang, J. L. Dai, Y. L. Li, *J. Appl. Phys.* **2020**, *128*, DOI `10.1063/5.0020999` (page 21).

[104] T. Takagi, *Vacuum* **1986**, *36*, 27–31 (page 21).

[105] T. Takagi, *Pure Appl. Chem.* **1988**, *60*, 781–794 (page 21).

[106] R. Beuhler, L. Friedman, *Chem. Rev.* **1986**, *86*, 521–537 (page 21).

[107] W. Brown, M. Jarrold, R. McEachern, M. Sosnowski, G. Takaoka, H. Usui, I. Yamada, *Nucl. Instruments Methods Phys. Res. Sect. B Beam Interact. with Mater. Atoms* **1991**, *59-60*, 182–189 (page 22).

[108] A. Perez, P. Melinon, V. Dupuis, P. Jensen, B. Prevel, J. Tuaillon, L. Bardotti, C. Martet, M. Treilleux, M. Broyer, M. Pellarin, J. L. Vaille, B. Palpant, J. Lerme, *J. Phys. D. Appl. Phys.* **1997**, *30*, 709–721 (page 22).

[109] S. A. Claridge, A. W. Castleman, S. N. Khanna, C. B. Murray, A. Sen, P. S. Weiss, *ACS Nano* **2009**, *3*, 244–255 (page 22).

[110] K.-H. Müller, *J. Appl. Phys.* **1987**, *61*, 2516 (page 22).

[111] C. L. Cleveland, U. Landman, **1992**, *257*, 355–362 (page 22).

[112] K. Albe, W. Möller, *Comput. Mater. Sci.* **1998**, *10*, 111–115 (page 22).

[113] H. Haberland, Z. Insepov, M. Moseler, *Zeitschrift für Phys. D Atoms Mol. Clust.* **1993**, *26*, 229–231 (pages 22, 55).

[114] H. Haberland, Z. Insepov, M. Moseler, *Phys. Rev. B* **1995**, *51*, 11061–11067 (pages 22, 55).

[115] S. F. Hwang, Y. H. Li, Z. H. Hong, *Comput. Mater. Sci.* **2012**, *56*, 85–94 (page 22).

[116] H. Gong, W. Lu, L. Wang, G. Li, S. Zhang, *Comput. Mater. Sci.* **2012**, *65*, 230–234 (page 22).

[117] A. Fischer, R. Kruk, H. Hahn, *Rev. Sci. Instrum.* **2015**, *86*, DOI `10.1063/1.4908166` (pages 22, 23, 55).

[118] A. S. Fischer, PhD thesis, Technical University of Darmstadt, **2015** (pages 22, 23).

[119] N. Gack, G. Iankevich, C. Benel, R. Kruk, D. Wang, H. Hahn, T. Reisinger, *Nanomaterials* **2020**, *10*, 1–27 (pages 23, 88).

[120] C. A. Schuh, T. C. Hufnagel, U. Ramamurty, *Acta Mater.* **2007**, *55*, 4067–4109 (page 27).

[121] K. Burke, *J. Chem. Phys.* **2012**, *136*, DOI `10.1063/1.4704546` (page 27).

[122] S. Plimpton, *J. Comput. Phys.* **1995**, *117*, 1–19 (pages 27, 43).

[123] A. P. Thompson, H. M. Aktulga, R. Berger, D. S. Bolintineanu, W. M. Brown, P. S. Crozier, P. J. in 't Veld, A. Kohlmeyer, S. G. Moore, T. D. Nguyen, R. Shan, M. J. Stevens, J. Tranchida, C. Trott, S. J. Plimpton, *Comput. Phys. Commun.* **2022**, *271*, 108171 (pages 27, 31, 43).

[124] M. Born, R. Oppenheimer, *Ann. Phys.* **1927**, *389*, 457–484 (page 27).

[125] J. G. Lee, *Computational Materials Science*, CRC Press, Second edition. | Boca Raton : CRC Press, Taylor & Francis, **2016** (pages 28, 30, 32).

[126] M. S. Daw, S. M. Foiles, M. I. Baskes, *Mater. Sci. Reports* **1993**, *9*, 251–310 (pages 29, 43).

[127] M. S. Daw, M. I. Baskes, *Phys. Rev. Lett.* **1983**, *50*, 1285–1288 (page 29).

[128] D. Frenkel, B. Smit, J. Tobochnik, S. R. McKay, W. Christian, Understanding Molecular Simulation, **1997** (pages 30, 32, 33).

[129] L. Verlet, *Phys. Rev.* **1967**, *159*, 98–103 (page 31).

[130] W. C. Swope, H. C. Andersen, P. H. Berens, K. R. Wilson, *J. Chem. Phys.* **1982**, *76*, 637–649 (page 31).

[131] C. Shannon, *Proc. IRE* **1949**, *37*, 10–21 (page 33).

[132] W. G. Hoover, *Phys. Rev. A* **1985**, *31*, 1695–1697 (page 33).

[133] M. Parrinello, A. Rahman, *Phys. Rev. Lett.* **1980**, *45*, 1196–1199 (page 34).

[134] W. Brostow, J. P. Dussault, B. L. Fox, *J. Comput. Phys.* **1978**, *29*, 81–92 (page 36).

[135] W. Brostow, M. Chybicki, R. Laskowski, J. Rybicki, *Phys. Rev. B - Condens. Matter Mater. Phys.* **1998**, *57*, 13448–13458 (page 36).

[136] V. A. Borodin, *Philos. Mag. A Phys. Condens. Matter Struct. Defects Mech. Prop.* **1999**, *79*, 1887–1907 (pages 36, 37, 73).

[137] A. Stukowski, *Model. Simul. Mater. Sci. Eng.* **2010**, *18*, DOI `10.1088/0965-0393/18/1/015012` (pages 36, 62, 69, 91).

[138] J. L. Finney, *Proc. R. Soc. London. A. Math. Phys. Sci.* **1970**, *319*, 495–507 (page 36).

[139] A. Stukowski, *JOM* **2014**, *66*, 399–407 (pages 38, 62, 69, 70, 91, 95, 126).

[140] S. P. Chilakalapudi, S. Katnagallu, A. Sarkar, P. Cao, W. Wenzel, H. Hahn, *Acta Mater.* **2022**, 118152 (pages 41, 65).

[141] G. Duan, D. Xu, Q. Zhang, G. Zhang, T. Cagin, W. L. Johnson, W. A. Goddard, *Phys. Rev. B - Condens. Matter Mater. Phys.* **2005**, *71*, 1–9 (pages 43, 73).

[142] T. Nasu, S. Takahashi, I. Ajiki, T. Usuki, Y. Onodera, M. Sakurai, Z. Wei, A. Inoue, B. He, W. Zhong, Z. Xie, S. Wei, *J. Alloys Compd.* **2007**, *434-435*, 44–47 (pages 43, 73).

[143] Y. Q. Cheng, A. J. Cao, E. Ma, *Acta Mater.* **2009**, *57*, 3253–3267 (pages 44, 98).

[144] K. A. Avchaciov, Y. Ritter, F. Djurabekova, K. Nordlund, K. Albe, *Appl. Phys. Lett.* **2013**, *102*, 0–4 (page 44).

[145] B. F. Lu, L. T. Kong, K. J. Laws, W. Q. Xu, Z. Jiang, Y. Y. Huang, M. Ferry, J. F. Li, Y. H. Zhou, EXAFS and molecular dynamics simulation studies of Cu-Zr metallic glass: Short-to-medium range order and glass forming ability, **2018** (pages 44, 76).

[146] P. Krasnochtchekov, K. Albe, Y. Ashkenazy, R. S. Averback, *J. Chem. Phys.* **2005**, *123*, DOI 10.1063/1.2074247 (page 51).

[147] A. Rosato, K. J. Strandburg, F. Prinz, R. H. Swendsen, *Phys. Rev. Lett.* **1987**, *58*, 1038–1040 (page 53).

[148] B. Sadigh, P. Erhart, A. Stukowski, A. Caro, E. Martinez, L. Zepeda-Ruiz, *Phys. Rev. B - Condens. Matter Mater. Phys.* **2012**, *85*, 1–11 (page 54).

[149] S. Rahmati, A. Zúñiga, B. Jodoin, R. G. Veiga, *Comput. Mater. Sci.* **2020**, *171*, 109219 (page 55).

[150] P. Meakin, P. Ramanlal, L. M. Sander, R. C. Ball, *Phys. Rev. A* **1986**, *34*, 5091–5103 (page 59).

[151] Y. Li, Q. Guo, J. A. Kalb, C. V. Thompson, *Science (80-.).* **2008**, *322*, 1816–1819 (pages 76, 80).

[152] M. Wakeda, J. Saida, J. Li, S. Ogata, *Sci. Rep.* **2015**, *5*, 1–8 (page 84).

[153] J. Saida, R. Yamada, M. Wakeda, S. Ogata, *Sci. Technol. Adv. Mater.* **2017**, *18*, 152–162 (page 84).

[154] S. Adibi, Z.-D. Sha, P. S. Branicio, S. P. Joshi, Z.-S. Liu, Y.-W. Zhang, *Appl. Phys. Lett.* **2013**, *103*, 211905 (pages 87, 99).

[155] A. N. Raegen, J. Yin, Q. Zhou, J. A. Forrest, *Nat. Mater.* **2020**, *19*, 1110–1113 (pages 87, 94).

[156] S. Singh, M. D. Ediger, J. J. De Pablo, *Nat. Mater.* **2013**, *12*, 139–144 (pages 87, 94).

[157] Z. Insepov, M. Sosnowski, I. Yamada, *Nucl. Instruments Methods Phys. Res. Sect. B Beam Interact. with Mater. Atoms* **1997**, *127-128*, 269–272 (page 90).

[158] L. P. Allen, Z. Insepov, D. B. Fenner, C. Santeufemio, W. Brooks, K. S. Jones, I. Yamada, *J. Appl. Phys.* **2002**, *92*, 3671–3678 (page 90).

[159] S. Jekal, *Res. Dev. Mater. Sci.* **2019**, *12*, DOI `10.31031/rdms.2019.12.000785` (page 95).

[160] C. Su, Y. Chen, P. Yu, M. Song, W. Chen, S. F. Guo, *J. Alloys Compd.* **2016**, *663*, 867–871 (page 99).

[161] L. Battezzati, D. Baldissin, A. Habib, P. Rizzi, *J. Phys. Conf. Ser.* **2009**, *144*, DOI `10.1088/1742-6596/144/1/012088` (page 99).

[162] B. Bian, X. Cui, J. Li, *AIP Adv.* **2021**, *11*, 015202 (page 99).

[163] S. Feng, L. Li, Y. Liu, L. Wang, R. Liu, *J. Non. Cryst. Solids* **2020**, *546*, 120265 (page 101).

[164] P. Cao, M. Li, R. J. Heugle, H. S. Park, X. Lin, *Phys. Rev. E - Stat. Nonlinear Soft Matter Phys.* **2012**, *86*, 1–8 (page 107).

[165] Y. Fan, P. Cao, *Handb. Mater. Model.* **2018**, 1–27 (page 107).

[166] X. Y. Li, Z. H. Jin, X. Zhou, K. Lu, *Science (80-.).* **2020**, *370*, 831–836 (page 107).

[167] H. Hu, T. Fu, C. Li, S. Weng, Y. Zhao, X. Chen, X. Peng, *Phys. Rev. B* **2022**, *105*, 1–8 (page 107).

A. Supplementary Material

A.1. Simulation Development
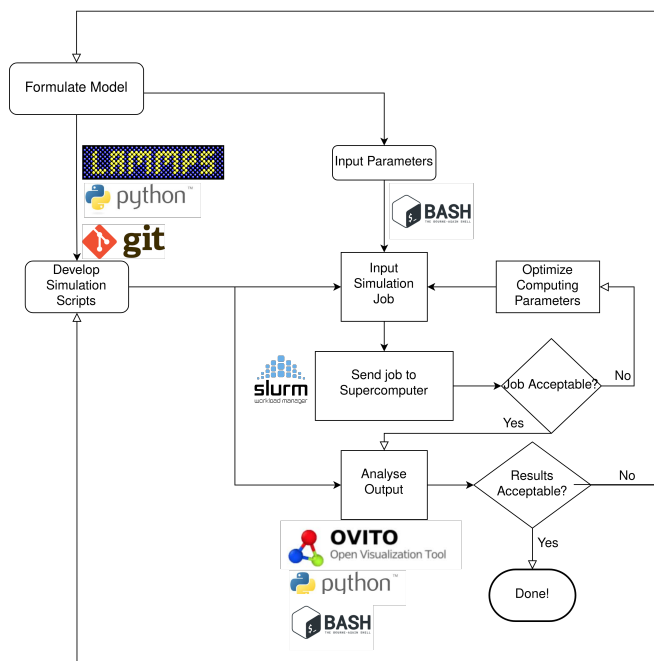
Figure A.1.: Simulation development process: The molecular dynamics (MD) high-performance computing (HPC) workflows were developed in a iterative fashion as illustrated.

A.2. Simulation Repository
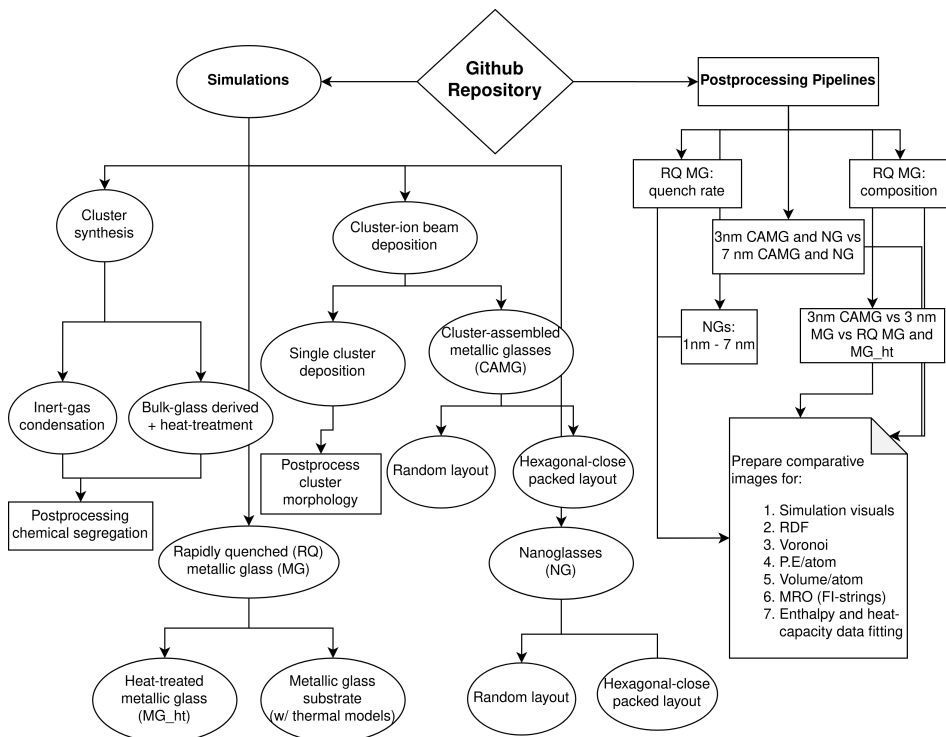
Figure A.2.: Simulation repository flowchart: The various large-scale atomic/molecular massively parallel simulator (LAMMPS) based semi-automated MD simulation workflows, and python data processing scripts developed for this thesis are depicted.

The simulation repositories can be accessed via the following Github links:

- Simulations + post-processing:
  https://github.com/syamalpraneeth/camg-simulations
- Comparative data-processing pipelines:
  https://github.com/syamalpraneeth/camg-analysis

A.3. Quenching of RQ MGs

(a)

(b)

(c)
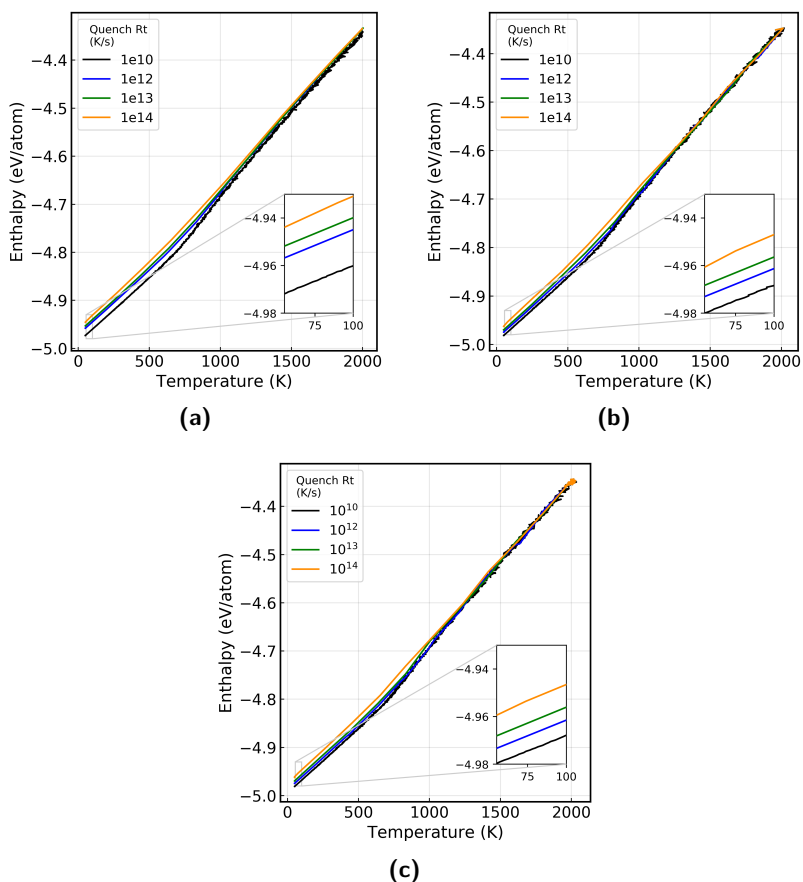
Figure A.3.: Enthalpy vs quench rate for Cu$_{50}$Zr$_{50}$ RQ MGs: Enthalpy evolution is recording while changing quenching simulation processes. (a) Simulated as performed as discussed in Section 4.1, (b) simulation starting with ~8000 atoms at 2000 K, and (c) ~8000 atoms melted from 50 K before quenching.
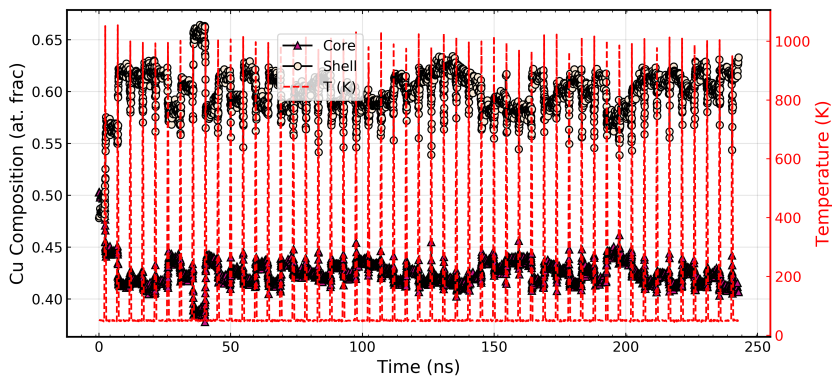
(a)
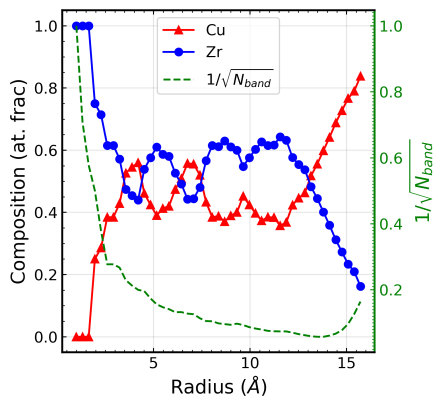
(b)

Figure A.4.: Additional heat-treatment to the 3 nm Cu$_{50}$Zr$_{50}$ Cluster: (a) Fluctuations in core Cu at. % during additional heat-treatment. (b) Final cluster radial composition profile. Inert-gas condensation (IGC) clusters simulations can help establish equilibrium profile.

A.5. Atomic Strain in Single-cluster Depositions

(a) Core-shell colour coding   (b) Local shear strain
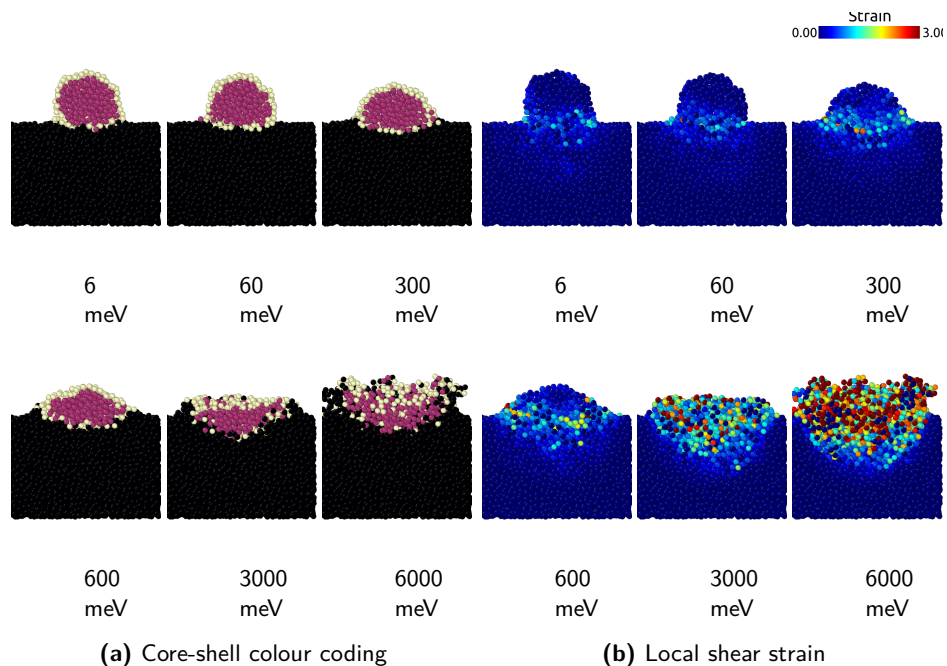
Figure A.5.: Local strain in Single 3 nm cluster depositions: Single cluster depositions at various impact energies are depicted 2 ns after deposition. (a) The deposited clusters and colour-coded by the core-shell structure determined in Figure 4.8. (b) The same cluster atoms in (a) are coloured by their local von-Mises shear strain. The intensity of distortion, and the volume of distortion are seen to increase with deposition energy.
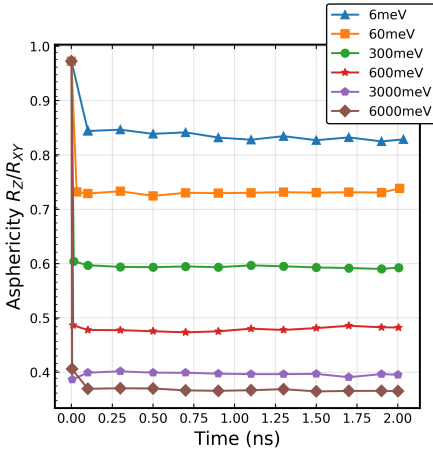
(a) 3 nm cluster
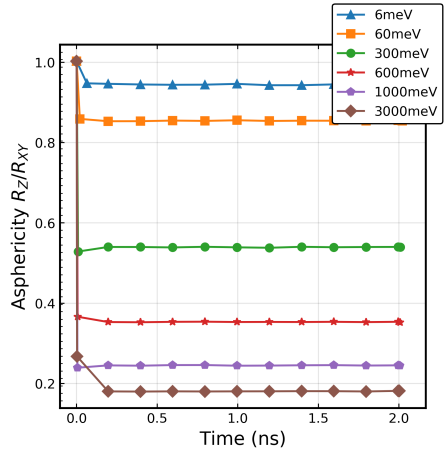
(b) 7 nm nanoparticle

Figure A.6.: Cluster asphericity time-evolution vs cluster-size: Singly deposited clusters are studied for two different particle sizes by the cluster asphericity (see Section 4.3 for more details). The as-deposited states of (a) the 3 nm clusters (same as Figure 4.11) and (b) the 7 nm nanoparticle, 2 ns after deposition.

A.6. Radial Distribution Functions for Simulated 3 nm CAMGs
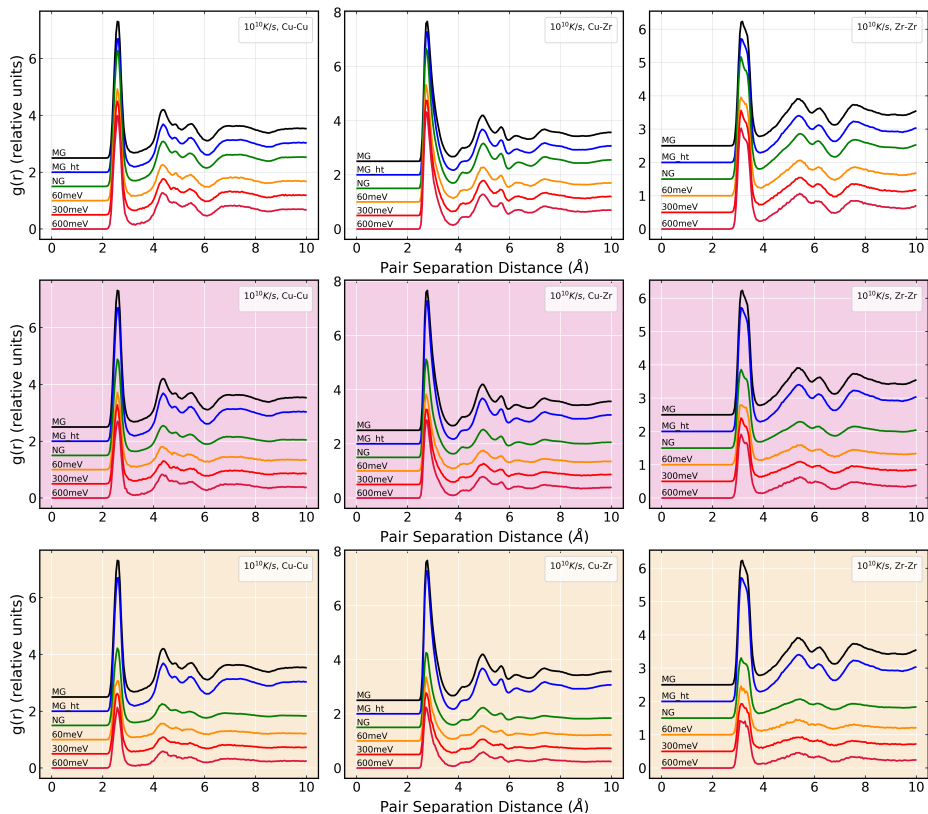
Figure A.7.: Pair-correlations in 3 nm CAMGs, NGs and MGs: Partial RDFs for the CAMGs show similar distribution in the core and interfacial regions as compared to other glasses, indicating that the average local-order in these glasses is similar. The graph backgrounds have been coloured magenta and yellow respectively to stick with the general colour scheme used for core and interfaces in this dissertation (See Figures 4.9 and 5.3).

For the simulated rapidly-quenched (RQ) metallic glass (MG) and nanoglass (NG), the

sample volume is the same as the simulation box. As seen in Chapter 5, this is not the case for cluster-assembled metallic glass (CAMG). The volume of the CAMG is evaluated by means of a surface mesh [139]. The plots have been normalized according the respective volumes of the samples considered. In the metallic glasses and NG case, the radial distribution function (RDF) converge to 1, as would any homogeneous system. However, when evaluating RDFs for the cores and interfaces separately in the NG and CAMGs, it does not converge to 1. The CAMG film is not a homogeneous system that spans the entire simulation box.

A.7. Voronoi Index Histograms for Cu-/Zr-centered in 3 nm CAMGs

(a)   **(b)**
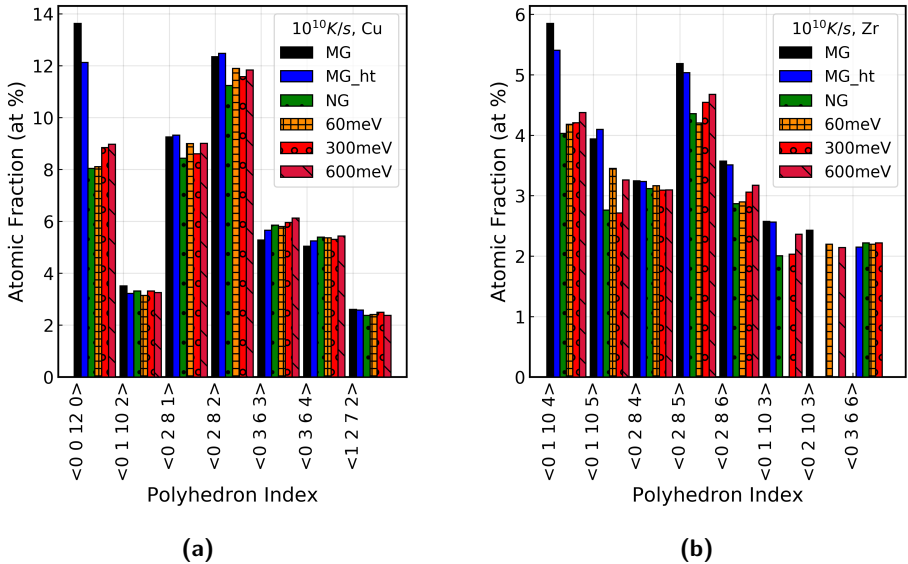
Figure A.8.: Voronoi polyhedra of 3 nm CAMGs for Cu- and Zr-centered atoms: The Voronoi histograms are represented separately by species. (a) The Cu-centered atoms exhibit higher full-icosahedral (FI)-order ($<$0 0 12 0$>$) than (b) the Zr-centered atoms. The icosahedral-like order (ILO) (not pictured) follows the same trend.

A.8. 3 nm CAMG Atomic Volume Distribution in Cores and Interfaces
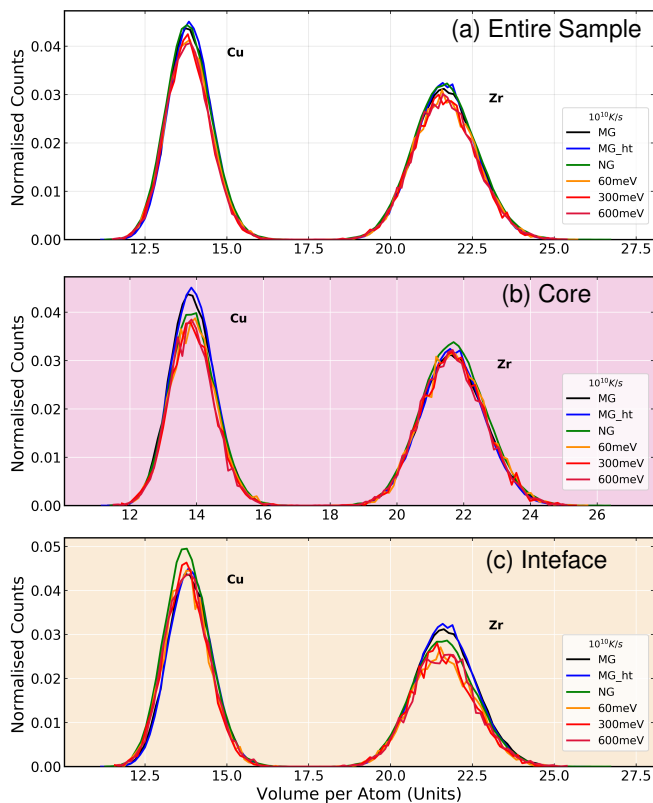
Figure A.9.: Atomic volume distribution in the 3 nm CAMG cores and interfaces: The effects of chemical segregation in CAMGs and NGs are easily observable as Cu peak height decreases in core and increases in interfaces. The shape of the distributions of CAMGs are similar to other glasses. Also similar to reports on NGs [21]. The distributions are similar also for core and interfaces.

Figure A.10.: P.E/atom distribution in the 3 nm CAMG: Atomic potential energy distributions of CAMGs are similar in shape for core and interfaces, also compared to NGs, RQ MG, and MG_ht.

B. Curriculum Vitae

Name:	Syamal Praneeth Chilakalapudi
Place of Birth:	Hyderabad, India
Nationality:	Indian

Education:

Jul 2017 - present	Doctoral Studies in Materials Science and Engineering Technische Universität Darmstadt
Aug 2011 - May 2016	5-year Integrated Masters of Science in Physics School of Physics, University of Hyderabad (UOH), India

Work Experience:

Jul 2017 - Apr 2022	Scientist (Work group Prof. Horst Hahn) Karlsruhe Institute of Technology, Germany
Jan 2020 - Feb 2020	Visiting Researcher (Research group Prof. Penghui Cao) University of California, Irvine
Jul 2016 - Jun 2017	Project Assistant (Research group Prof. Seshubai Vummethala) School of Physics, University of Hyderabad
Nov 2016 - Jun 2017	Project Assistant (Research group Prof. S. Srinath) School of Physics, University of Hyderabad

Internships:

May 2015 - Jun 2015	National University of Singapore
May 2014 - Jun 2014	Dept. of Physics, IIT-Madras, India
May 2013 - Jun 2013	Dept. of Physics, Univ. of Wisconsin-Madison

Scholarships/awards:

2016	UGC-CSIR lectureship eligibility in India
2016	Best Poster Award, Frontiers in Physics Conference, UOH
2015	SIPIS Summer Fellowship NUS
2014	Summer Research Fellowship IIT Madras
2013	Khorana-S.N. Bose Summer Scholarship

PUBLICATIONS

Journal Articles

*Publications relevant to this thesis.

- *Cluster size effects in cluster-based glasses
  S. P. Chilakalapudi, A. Sarkar, and H. Hahn, (in preparation).

- *Energetically deposited cluster assembly of metallic glasses
  S. P. Chilakalapudi, S. Katnagallu, A. Sarkar, P. Cao, W. Wenzel, and H. Hahn, *Acta Materialia* (2022), 118152, `https://doi.org/10.1016/j.actamat.2022.118152`.

- Geometrical frustration in a new $S = \frac{1}{2}$ distorted checkerboard lattice $PbCuTeO_5$
  S. P. Chilakalapudi, A. Shahee, A. V. Mahajan, S. Srinath, and B. Koteswararao, *AIP Conf. Proc.* **1832**, 130032 (2017) `https://doi.org/10.1063/1.4980752`.

- Synthesis and magnetic properties of a quantum magnet $PbCuTeO_5$
  B Koteswararao, S. P. Chilakalapudi, A. Shahee, P. V. Srinivasarao, S. Srinath, A. V. Mahajan, arXiv preprint, `https://doi.org/10.48550/arXiv.1705.10560`

Conference contributions

*Presenting author

Oral Presentations

- Local structure tailoring in $Cu_{50}Zr_{50}$ cluster-assembled metallic glasses
  S. P. Chilakalapudi*, S. Katnagallu, P. Cao, W. Wenzel, and H. Hahn, DPG Spring Meeting, Mar 2021.

- Geometrical frustration in a new $S = \frac{1}{2}$ distorted checkerboard lattice PbCuTeO$_5$
  S. P. Chilakalapudi*, A. Shahee, A. V. Mahajan, S. Srinath, and B. Koteswararao,
  International Conference on Magnetic Materials (ICMAGMA), Hyderabad, Feb
  2017.

Poster presentations

- Cluster-assembly of metallic glasses as a means to local structure tailoring in amorphous
  materials
  S. P. Chilakalapudi*, S. Katnagallu, A. Sarkar, P. Cao, W. Wenzel, and H. Hahn,
  CECAM Workshop on Virtual Materials Design, Jul 2021.

- Controlling the structure and properties of cluster-assembled amorphous materials
  C. Benel*, S. P. Chilakalapudi*, A. Leon, T. Reisinger, L. Henrichs, R. Kruk, K.
  Fink, W. Wenzel, H. Hahn, POF, Karlsruhe, Sep 2018.

- Synthesis and characterization of a new $S = \frac{1}{2}$ distorted checkerboard lattice PbCuTeO$_5$
  S. P. Chilakalapudi*, S. Srinath, and B. Koteswararao, Frontiers in Physics symposium,
  Hyderabad, Dec 2016.

- Synthesis and characterization of a new $S = \frac{1}{2}$ distorted checkerboard lattice PbCuTeO$_5$
  S. P. Chilakalapudi*, A. Shahee, A. V. Mahajan, S. Srinath, and B. Koteswararao,
  61st DAE Solid state physics symposium, Bhubaneshwar, Dec 2016.

WORKSHOPS

2022	NVIDIA/LRZ *AI for Science* Bootcamp
2022	EuroHPC Vega *N-Ways To GPU Programming* Bootcamp
2021	NVDIA Workshop on *Fundamentals of Deep Learning*
2019	*X-Ment softskills and cross-mentorship program*, KIT Germany
2018	*Winter School in Chemistry: Machine Learning*, U. Helsiki, Finland
2012	5th *Science Conclave* held at the IIIT-Allahabad, India
2011	*Science Camp Vijyoshi* held at IISc, Bangalore, India

C. Acknowledgments